The Pennsylvania State University

The Graduate School

College of Engineering

SCALING, CHARACTERIZATION, AND APPLICATION OF GRAM-RANGE EXPLOSIVE CHARGES TO BLAST TESTING OF MATERIALS

A Dissertation in

Mechanical Engineering

by

Michael J. Hargather

Submitted in Partial Fulfillment
of the Requirements
for the Degree of

Doctor of Philosophy

May 2008

The dissertation of Michael J. Hargather was reviewed and approved* by the following:

Gary S. Settles
Distinguished Professor of Mechanical Engineering
Dissertation Adviser
Chair of Committee

James B. Anderson
Evan Pugh Professor of Chemistry

Panagiotis Michaleris
Associate Professor of Mechanical Engineering

Robert J. Santoro
George L. Guillet Professor of Mechanical Engineering

Gita Talmage
Professor of Mechanical Engineering

Karen Thole
Professor of Mechanical Engineering
Head of the Department of Mechanical and Nuclear Engineering

* Signatures are on file in the Graduate School

ABSTRACT

Laboratory-scale experiments with gram-range explosive charges were performed. Optical shadowgraphy and high-speed digital imaging were used to measure the explosive-driven shock wave position versus time from varying explosive charges. From this, shock Mach number versus distance from the explosion center can be found. These data then yield explosive overpressure and duration, thus explosive impulse. Explosive impulse is a key parameter in explosive characterization and in determining potential damage to structures. High-speed digital cameras and three-dimensional digital image correlation software were then used to measure aluminum panel deflections due to measured explosive impulse impingement.

Explosive characterization was performed on two explosives, pentaerythritol tetranitrate (PETN) and triacetone triperoxide (TATP). The characterization included optical measurements of shock wave position versus time and piezo-pressure measurements of explosive overpressure duration versus distance. Experimental results were supported computationally by simulations performed using the commercial computational fluid dynamics code AUTODYN. Results show the importance of the shock Mach number versus radius profile, since all other pertinent information can be derived from it. These data show that the characterization procedure developed here is effective for both a traditional explosive, PETN, and for an exotic, non-ideal explosive, TATP.

Gram-scale-explosive blast tests were performed on aluminum panels using the above characterized explosives. Typically, material blast testing is conducted at full-scale, but these tests are expensive, dangerous, and difficult to instrument effectively in the field. The present laboratory experiments performed with gram-scale explosive charges show that laboratory-scale testing can be repeatable and effective for documenting material responses to an explosive impulse.

A "shock-hole" fixture was developed to allow panel boundaries to be effectively clamped, yet provide optical access to the deforming panel surface, which was measured by high-speed digital imaging and image correlation. Results of parametric experiments show that panel deformation is a function of explosive impulse, independent of explosive charge type. Dynamic and permanent plastic deformation of the aluminum panels is also dependent on fixture design, with the permanent plastic deformation being highly influenced by boundary conditions.

The gram-scale explosive testing procedures developed here show the benefits of laboratory-scale explosive testing: high repeatability and advanced instrumentation, along with relatively low resource costs and minimal danger to researchers. Explosive scaling procedures developed previously allow gram-scale blast information to be extrapolated to full-scale test parameters. Small-scale material testing can be more difficult to scale appropriately, yet it can still be used to validate computational models and to experimentally determine physical properties of materials. The techniques developed here form a basis for future laboratory-scale explosive materials testing. The scientific understanding of gram-range explosions and blast scaling has also benefited.

TABLE OF CONTENTS

LIST OF TABLES

LIST OF FIGURES

ACKNOWLEDGEMENTS

I would like to thank Dr. Gary S. Settles for being my adviser and mentor for the last four years. He has helped me to become a proficient and confident experimentalist and prepared me for a successful career in academia. Throughout my time in the Penn State Gas Dynamics Laboratory, he has given me countless opportunities to develop myself academically and professionally through conference presentations, proposal writing, and involvement with research sponsors. It has been an honor to work with him and to learn from him.

Special thanks are also due to all members of the Penn State Gas Dynamics Lab and graduate school friends. JD Miller and Lori Dodson-Dreibelbis have provided daily support, encouragement, and advice throughout my time in the lab. The students that have worked in the lab have been my best friends throughout the last four years and make daily life exciting. I could not imagine life without the adventures we have had on a daily basis. Thanks are due to everyone who has ever helped with an experiment or raised a glass with me, but especially to: T. Morris, B. Craven, W. Smith, M. Staymates, J. Volpe, T. Liebner, M. Madalis, R. Bigger, M. Biss, M. Lawson, S. Frymire, C. Cormier, T. Prabhakar, and M. Thiel.

My parents, John and Kate, and my brother, Matt, have also been a source of infinite support. Throughout my life they have helped and guided me in innumerable ways. Their love, care, and enthusiasm for everything that I have done has given me the strength to become the person I am today. They have nurtured my love of science and engineering since I was young and have always supported my quest for knowledge. My extended family has also provided love and guidance throughout my life. I love my entire family and am proud to dedicate my work to them and especially to my grandfather, David Haley.

Chapter 1

INTRODUCTION

1.1 Research Motivation

Trinitrotoluene (TNT) has always been the standard for explosives and explosive damage, but with the development of new explosives and energetic materials, this standard has become cumbersome and somewhat obsolete. Traditionally, explosives are characterized by a "TNT equivalence" value based on the energy released in an explosion [1], but this value is now insufficient. Different explosives have different energy release rates associated with their detonation, and these rate variations produce different explosion characteristics. Shock wave propagation speed is the salient result of an explosion, and it changes from one explosive to another depending on detonation properties and rates.

As a shock propagates through quiescent air, property variations behind the shock result in pressure and temperature variations, which are primary causes of damage. Understanding these property distributions is of critical importance to explosives research and development. These variations, however, cannot be determined from a simple TNT equivalence value, they can only be determined from more detailed experiments.

In order to accurately study shock propagation from different explosives, a controlled environment is required. Using standard explosive scaling laws [2], tests can be conducted at the laboratory-scale, then extrapolated to full-scale. In the laboratory

setting, optical techniques such as shadowgraphy can be easily implemented to fully document shock propagation. The use of a high-speed digital camera then allows the shadowgraph images to be processed to determine shock location as a function of time and thus shock Mach number-versus-distance. From this, all property variation information can be derived. Explosives characterized by means of this new definition can then be used to accurately study material responses to explosive blasts.

Explosive deformation of materials occurs in many civil and military applications, but little fundamental scientific knowledge exists to fully describe a material's response. Typically, full-scale specimens are subjected to large blasts, such as the original atomic bomb tests conducted at full-scale with real tanks, etc. These full-scale tests are expensive, hard to accurately instrument, and conducted with explosives defined only by a TNT equivalence value. Scale-model tests, with well-defined explosives, would develop more fundamental scientific knowledge and improve the ability to accurately model explosive events.

Laboratory tests with characterized explosives can also document material responses to a wide range of explosive blast parameters. Experiments can be conducted and repeated at various conditions to fully understand a material response. High-speed cameras and digital image correlation software can be used to accurately measure material deformation and strain under each loading condition. With this time-resolved information, new material models can be developed and computationally validated, improving the scientific understanding of material responses at the high-strain rates associated with explosive blasts.

Laboratory-scale explosive research can therefore contribute to the scientific knowledge of shock wave propagation and high-speed material deformation. Commercially available technology, combined with traditional optical visualization techniques, allows new information to be learned about high-speed explosive events. Laboratory-scale results can be used to validate computational models and traditional scaling techniques can extend this research to full-scale expectations.

1.2 Literature Review

1.2.1 Explosive Scaling

Explosive scaling is used to relate physical dimensions between different explosive charges of the same material. The first scaling law, developed by Hopkinson [3], relates the radius, R of a spherical charge to its mass, W, and energy release, E:

$$\frac{R_1}{R_2} = \left(\frac{W_1}{W_2}\right)^{\frac{1}{3}} = \left(\frac{E_1}{E_2}\right)^{\frac{1}{3}} \tag{1.1}$$

The Hopkinson scaling law requires not only that the two charges are of the same material and packing density, but also that they are exploded in the same atmosphere. A constant atmosphere is required because the scaling law is based on two charges producing the same peak pressure behind the shock front at their respective scaled distances [4].

The Sachs scaling law was developed to relate explosions of different masses in different atmospheres [5]. Sachs stated that the peak pressure, temperature, and density behind an explosively-driven shock would scale relative to the ambient conditions. For

two explosive charges of the same material, exploded in atmospheres with pressures P_{o1} and P_{o2}, the Sachs scaling for distance is given by:

$$\frac{R_1}{R_2} = \left(\frac{W_1}{W_2}\right)^{\frac{1}{3}} \left(\frac{P_{o2}}{P_{o1}}\right)^{\frac{1}{3}} = \left(\frac{E_1}{E_2}\right)^{\frac{1}{3}} \left(\frac{P_{o2}}{P_{o1}}\right)^{\frac{1}{3}} \tag{1.2}$$

Time, t, scales with the ambient speed of sound, which for air atmospheres reduces to the square root of the ratio of temperatures T_1 and T_2:

$$\frac{t_1}{t_2} = \left(\frac{W_1}{W_2}\right)^{\frac{1}{3}} \left(\frac{P_{o2}}{P_{o1}}\right)^{\frac{1}{3}} \left(\frac{T_1}{T_2}\right)^{\frac{1}{2}} = \left(\frac{E_1}{E_2}\right)^{\frac{1}{3}} \left(\frac{P_{o2}}{P_{o1}}\right)^{\frac{1}{3}} \left(\frac{T_1}{T_2}\right)^{\frac{1}{2}} \tag{1.3}$$

The Sachs scaling law has been verified for TNT charges from 25 to $10^5 kg$ by Dewey [6] and has since been extended by other researchers to include various explosives over the range of 10^{-6} to $10^6 kg$ [4, 7].

With explosive scaling, charges of different masses, exploded under different conditions, can be related to a standard explosive charge, exploded in a standard atmosphere. The scaling approach used by Kleine et al. [7] was also used in the present study, where all experiments were scaled to normal temperature and pressure (NTP). The scaling is given in Equations 1.4 and 1.5 and the scale factors are presented in Equations 1.6 and 1.7. The radius from the charge center is r and W_{std} is the charge mass of the standard charge, which is $1g$ for the present research. Variables with subscripts s are scaled values.

$$R_s = \frac{r}{S} \tag{1.4}$$

$$t_s = \frac{c\,t}{S} \tag{1.5}$$

$$S = \left(\frac{W}{W_{std}}\right)^{\frac{1}{3}} \left(\frac{101325\,Pa}{P}\right)^{\frac{1}{3}} \tag{1.6}$$

$$c = \left(\frac{T}{288.16\,K}\right)^{\frac{1}{2}} \tag{1.7}$$

Once scaled to a standard charge, scaled shock radius as a function of scaled time should be uniform for charges of a given explosive at any mass. Shock-wave-motion data can then be fit to Equation 1.8 by determining coefficients A, B, C, and D, where a_o is the ambient sound speed. This equation, presented by Dewey, represents a qualitative fit to experimental data and satisfies physical limits on time [8]. At $t_s = 0$, the explosive shock wave radius has a finite value, corresponding approximately to the radius of the solid explosive charge. The shock appears to originate from this location because the shock propagation through a solid explosive, centrally initiated, is faster than the propagation through air by over an order of magnitude [8]. As $t_s \to \infty$ the derivative of R_s, as given in Equation 1.9, tends to a constant. This represents shock wave decay to a sound wave, traveling at the ambient sound speed. For data over a large range of radii, it has been suggested that the coefficient B should be set to 1.0 to enforce this limit [9].

$$R_s = A + B\,a_o\,t_s + C\,\ln(1 + a_o\,t_s) + D\,\sqrt{\ln(1 + a_o\,t_s)} \tag{1.8}$$

$$\frac{dR_s}{dt_s} = B\,a_o + \frac{C\,a_o}{1 + a_o\,t_s} + \frac{D\,a_o}{2\,(1 + a_o\,t_s)\,\sqrt{\ln(1 + a_o\,t_s)}} \tag{1.9}$$

Once the shock location as a function of time is known for a given explosive, all other important information can be derived. Equations 1.8 and 1.9 can be manipulated to determine the shock Mach number versus radius from the charge center. With the

shock Mach number and the Rankine-Hugoniot relationship the variations of pressure, density, and temperature behind the shock can be determined [10]. The variation of pressure behind the shock wave is the most important property for the present research.

An "ideal blast wave" profile can be defined at a point in space by examining the pressure-time history as a shock wave passes [11]. An ideal pressure-time history is schematically shown in Figure 1.1. The pressure immediately increases from atmospheric pressure, P_{atm}, to a maximum pressure, P_{max}, as the shock wave passes. The pressure then decays exponentially, crossing the atmospheric pressure at a specific time, t_d, after the initial shock arrival. This time is the defined as the positive pressure duration. The pressure continues to decay to a minimum value, then rises back to the original atmospheric pressure, concluding the event. The maximum pressure rise above atmospheric it typically referred to as the shock overpressure [2].

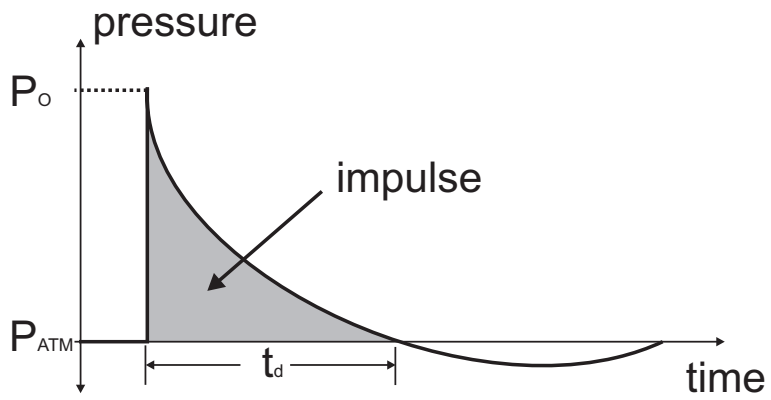

Figure 1.1. Pressure-time history of an ideal explosively-driven shock wave

The ideal shock wave profile can be divided into two primary parts, the positive pressure phase and the negative pressure phase. The integral of pressure with respect to time over each of these regions defines the positive impulse and negative impulse [11]. The positive impulse, shown as the shaded region in Figure 1.1, is typically larger than the negative impulse by several orders of magnitude and therefore is generally the only impulse considered in explosive modeling [2]. The negative impulse, however, may become important at large scaled distances from an explosion when the peak positive pressure is of the same order of magnitude as the peak negative pressure. For this condition, the long duration of the negative phase causes the impulse magnitudes to be similar and therefore of equal modeling importance [12].

With the scaling techniques discussed here, explosive blasts and the resulting property distributions can be scaled to account for changes in the mass of an explosive charge [2]. The scaling is valid over several orders of magnitude and for different explosive materials, but it is not valid for comparing different explosive materials. To compare two explosive materials, an explosive characterization is required.

1.2.2 Explosive Characterization

Explosive characterization is the process of quantifying explosive blast parameters relative to a standard. Typically, TNT is used as the standard explosive because it is readily available and produced with high chemical purity [1]. The wide use of TNT in both civil and military applications has caused it to become the best-documented explosive. Although it is a non-ideal explosive, the ability to scale TNT explosions and the wealth of TNT blast data has confirmed it as the standard explosive.

The properties of TNT blasts are well documented, and the previously defined scaling laws have been confirmed over several orders of magnitude, making it an ideal standard [6]. TNT, however, is not an ideal explosive for all scaling purposes. As a secondary explosive, which must be subjected to a strong shock wave to initiate detonation [13], TNT does not explode reproducibly in masses less than $5kg$ [4]. Another documented problem with TNT is an "after-burning" of the explosion products, which affects flow properties behind the shock front [4]. This problem of after-burning also occurs for aluminized explosives and results in difficulties in characterizing them according to a TNT equivalence [14]. Such issues make TNT a less than an "ideal" explosive compound.

From the wealth of TNT data, a wide range of TNT equivalence tests has evolved for measuring the characteristics of explosives. One simple method for determining TNT equivalence is to directly relate the total energy released by an explosion to that released by a TNT charge. This method assumes all energy is transfered to the shock propagation and can be approximated by the original blast theory developed by Taylor [15]. Although it is not a detailed equivalence estimate, it can be useful for first-order numerical simulations [16].

The most common TNT equivalent tests are the air-blast and plate-dent tests [14]. The air blast test compares pressure profiles from piezoelectric gages placed at discrete distances from an unknown explosive. The TNT equivalence thus determined varies not only as a function of radius, but also based on whether the maximum overpressure value or total impulse value is chosen to scale to TNT [14, 17, 18]. With a discrete number of pressure transducers, however, the collected data are limited and often does not resolve

the full variation of TNT equivalence [19]. The plate dent test measures the deflection of a given metal plate, but there is no standard for explosive charge mass, stand-off distance, or plate material to be used, creating wide variation in reported data [14]. The plate dent results also become tied to the material response to the blast, another complicated topic addressed by this dissertation.

Overall, the wide range of TNT equivalence tests all have limitations in data resolution and typically are tied to arbitrary testing parameters. In order to simplify these tests and consolidate information to give a single characterization value, other methods must be used.

Research pioneered by Kleine et al. used schlieren visualization and a high-speed digital camera to record shock propagation as a function of time from laboratory scale explosive charges [7]. The shock radius data were fit to Equation 1.8, and the shock Mach number was defined as a function of radius from the charge. From these data, TNT equivalence can be derived as a function of radius. The TNT equivalence of silver azide was defined by Kleine et al. as the mass of TNT required to deliver the same peak overpressure the same distance as a given mass of silver azide [7]. The overpressure can be found from the Rankine-Hugoniot relationship and the local shock Mach number. Equation 1.10 shows this classical relationship between the overpressure, P_o, and the shock Mach number, M, for a shock moving through air with specific heat ratio $\gamma = 1.4$ [1].

$$\frac{P_o}{P_{atm}} = \frac{2\gamma(M^2 - 1)}{\gamma + 1} = \frac{7(M^2 - 1)}{6} \tag{1.10}$$

The results show that the TNT equivalence value is a nonlinear function of radius from the charge center [7]. Dewey applied the concepts developed by Kleine et al. to data from propane-oxygen explosions to further show the radial dependence of TNT equivalence values [20]. These investigations highlighted the advantages of using optical techniques and laboratory-scale experiments to more fully document TNT equivalence variations of different explosives. These techniques provide the basis for the current research and a starting point for future experiments.

The present research also extends the explosive characterization by examining the variation of overpressure duration. The overpressure duration is a key parameter in determining the damage from an explosion, and therefore is needed in addition to TNT equivalence [21]. Kinney and Graham hypothesized, based on a physical argument, that the overpressure duration could be estimated, knowing the shock propagation characteristics [1]. No experimental validation for this hypothesis was found, therefore the present research also investigates this claim.

Measured profiles documenting the variation of shock Mach number and overpressure duration with respect to radius completely characterize an explosive. Once characterized, these explosives can be used in the blast testing of materials. The known properties of the explosive then provide accurate knowledge of the input boundary conditions for the materials tests, something rarely known in typical full-scale field tests.

1.2.3 Explosive Material Deformation

Explosive blast research is important for understanding the damage caused by an explosion and also for the development of blast-resistant materials. Typically, blast

tests are conducted on full-scale models or structures to determine the actual material response [22]. Even the smallest of these full-scale tests can require $10 - 100kg$ explosive charges at distances of up to $100m$, which forces these tests outdoors into relatively uncontrolled settings [23]. At this scale, instrumentation becomes difficult and expensive, often yielding only point-wise piezoelectric pressure profiles at limited locations and a qualitative evaluation of material deformation. Optical methods to reveal shock waves in the field, such as background distortion and sunlight shadowgraphy, are often crude and weather dependent [24]. There is little evidence of any quantitative shock radius versus time data, as described earlier, from field testing. Overall, the instrumentation difficulties and prohibitive cost of large-scale blast testing result in limited experiments and even more limited data. Although not able to completely eliminate full-scale testing, laboratory-scale experiments provide unique data collection opportunities and new insights into the physical phenomena.

Laboratory-scale blast experiments provide a more controlled environment with better instrumentation potential. In the laboratory setting it is easier to implement optical visualization techniques such as schlieren and shadowgraphy [24], but few researchers use these techniques to their fullest. The majority of the published laboratory-scale research focuses on determining a maximum post-test plate deflection and a qualitative shape of the final plate [25]. Nurick et al. have performed the majority of recent work and established standard terms for the qualitative definition of plate failures into one of three modes [26]. The work by Nurick et al., however, is limited due to their lack of full knowledge of the explosive energy input, and can be improved with full-field deformation measurements.

The measurement of explosive impulse can be made directly from a well characterized explosive, as discussed above, or it can be determined from a ballistic pendulum [27]. Through an energy balance, the ballistic pendulum method determines an approximate explosive impulse from the change in height of a free-swinging mass. The mass is the test plate and fixture, which are suspended on wires attached to the ceiling of the test facility. The ballistic pendulum measurement does not, however, directly measure the primary shock energy applied to the plate, but rather a total energy impulse delivered over the entire event. This measurement does not directly account for variations in shock propagation or discriminate between positive and negative blast impulses.

Initial experimental research on the explosive deformation of circular plates was done by Bodner and Symonds [28]. The major contributions of this work were the use of the ballistic pendulum to measure explosive impulse and the use of thin cylindrical explosive charges. These charges were placed in contact with a foam material which was in contact with the metal plate being deformed. This foam material was used to decrease the maximum pressure amplitude and to increase the pressure duration in order to prevent the metal panels from failing in shear [28]. These techniques were built upon and used in the later work done by Nurick et al. [29].

The use of an explosive charge in direct contact with a "witness" material changes the physics of the explosive blast test, however. The shock wave generated by the explosion is no longer coupled to the material plate through the air, but rather through a solid material with more complicated shock propagation properties that remain undefined in the publications. With a lack of visualization or direct measurement of the shock wave impacting the test panel, it is difficult to understand the nature of the explosive load and

impossible to specify the input boundary condition. As shown by Held [21], cylindrical charges produce complicated shock wave patterns in the near-field, which is where the tests conducted by Langdon et al. typically occur [30].

Other experiments use a short tube section through which the explosive blast is propagated, further complicating the final shape of the shock wave before it impacts the test panel [31]. Through all of these tests the possibility of non-uniform shock loading or shock focusing exists, complicating the interpretation of results as a pure function of blast impulse. The large body of work published by Nurick and his coauthors, however, does show that explosive deformations scale according to blast impulse as measured by the ballistic pendulum [31].

To improve these results and extend the applications to the broader analysis of material response to an air blast, research should be conducted with spherical explosive charges suspended in air. These tests would couple the energy release from the explosion to the plate via the air in a well-characterized manner. This coupling also represents the most frequent mode by which actual explosive damage occurs. The present research investigates this coupling of the explosive energy from the explosive to the plate through the air.

Other experimental research uses shock tubes to produce blast impulses [9]. These tests are also non-ideal for simulating a typical explosion. One approach is to clamp the test panel inside a shock tube and subject it to the shock wave produced from the bursting of a diaphragm separating high and low pressure chambers. The pressure history for these tests however does not match that expected from an air blast [32]. The pressure rises abruptly as in a typical shock impact, but fails to decay as shown in Figure

1.1, instead remaining high and oscillating as the shock reflects within the tube. Further irregularities exist with the eventual impact of the contact surface between the driver and driven gases. These tests, however, proved useful for matching numerical models of materials but no attempts to scale results according to shock loading were made [33].

A better approach using a shock tube as the "explosive source" is to discharge the shock tube into air and place the material panel at a finite distance from the end of the tube [34]. This technique allows the shock to propagate spherically through air, coupling the energy properly and producing an appropriate shock pressure profile as measured experimentally [34]. The measured pressure, however, stops after the shock wave passes and it is unclear whether the emergence of the contact surface from the shock tube affects the test panel at later times in the experiment [34]. Results prior to the contact surface arrival should scale according to explosive impulse, but data after contact surface impact represent fundamentally different loading conditions.

Some investigations have explored the deformation of materials as a result of high velocity projectile impact [35]. The work by Wen and Jones [36] showed aluminum and steel plate deformation due to projectiles and attempted to develop criteria to define projectile impact resistance. Other work used projectile impact to approximate blast loading [37,38]. The conclusions found through this work, however, show that the results are not always applicable to extrapolation to actual blast loading based on the projectile momentum [37]. Overall, the problems of projectile impact and general blast loading represent two different regimes of damage modes and should be treated as two separate physical phenomena.

The instrumentation used for the measurement of material deformations also varies widely among the various research groups. The simplest methods produce point measurements of plate deflection as a function of time throughout the event [33]. Other methods use strain gages to measure strain rates at specified locations on the surface of the material [34]. Nurick et al. used an optical technique to measure when the plate surface disrupts laser planes parallel to the plate surface, but this method does not specifically measure what point on the surface breaks the plane [39]. Optical techniques similar to particle image velocimetry have been used to measure granular flow around a ballistic impact [40], but have not been applied directly to solid material testing.

Other new optical techniques have been developed that are capable of determining full-field three-dimensional witness plate shape as a function of time [41]. These techniques of measuring full-field, time-resolved, spatial motion can produce an unprecedented amount of information from a single test, but have not been applied to explosive material tests prior to the present research.

Computational modeling has been used extensively for predicting material deformation due to explosive blasts and impulsive loads. Most modeling has focused on either mid-point witness plate deflection as a function of time or permanent deformation of thin solid plates. A broad review of methods and approximations used by various researchers is given by Nurick and Martin [42]. More recent research has examined the response of composite-laminate plates [34, 43] and various panel reinforcement methods [30, 44]. The computational models of plate deformation, however, frequently are limited by a lack of sufficient high-quality experimental data, as discussed above, or due to a lack of information regarding material properties at high-strain rates.

Material properties at high-strain rates are required to accurately model material responses to explosive blasts [45]. Typically these material properties are not known a priori and are significantly different from the static properties generally defined for materials. These high-speed properties are even unknown for some common materials and only become more complex for more complex materials [46]. Although these properties can be determined from experiments with split Hopkinson pressure bars [45] or from plate vibration modes [47], new optical techniques show potential for developing higher-resolution data. The present research applies modern optical technology and methods to develop experimental and measurement techniques which could be used to determine these material properties and thus improve material models.

1.3 Objectives of the Present Research

The present research is focused on expanding the basic scientific knowledge of explosive characterization and material deformation using modern optical methods. As discussed above, previous research has often been conducted using large-scale, under-instrumented experiments, often failing to capture basic scientific understanding of the problems. The present experimental research will use scaling and modern optical instrumentation techniques to improve the quality and quantity of scientific data and information gained from traditional explosive tests.

By conducting experiments at the laboratory-scale, the present research will be able to more fully document the explosion process of different explosive materials. With the characterization procedure outlined and pioneered by Kleine et al. as a foundation [7], the present work will develop new explosive characterization definitions for both

a traditional military secondary explosive and a new, non-ideal primary explosive of homeland security interest. New techniques will be developed for the production and initiation of these explosive charges in order to conduct this research safely and at the laboratory scale. Shadowgraph visualization, high-speed digital photography, and piezo-pressure measurements will be used to collect data. These data will characterize the explosive and be used to test an unproven theoretical hypothesis proposed by Kinney and Graham [1]. The explosive characterization results and traditional scaling laws will be validated and verified using a computational model and archival full-scale experimental data.

With characterized explosives, the variations of overpressure, overpressure duration, and impulse will be determined as functions of distance from the charge center. Knowledge of the impulse to a high degree of accuracy will allow material blast research to be conducted with well-known input boundary conditions, something that is rarely possible in typical field tests. The present work thus intends to develop and demonstrate high-accuracy, laboratory-scale material blast research techniques.

The present research will investigate the requirements for laboratory-scale blast research and produce initial results and the pertinent scaling analysis. To document the deformation and motion of the material panels, new digital image correlation techniques will be used [41]. These techniques require two high-speed digital cameras and commercial software to measure three-dimensional shape and motion of test panels. Until the present study, this optical measurement technique has not been applied to material blast response research and is expected to produce a new depth of knowledge that typical current point measurements are incapable of producing.

The present study will apply traditional scaling approaches to define material deformation as a function of explosive impulse. This research, however, will be the first to document material deformation from two different characterized explosives. The use of two different explosive materials allows the explosive impulse to be varied and matched between experiments. This will be used to determine if explosive impulse is the only important parameter or whether other variables exist that are necessary to describe the comparative energy release from two different explosives.

Through the present research, new scientific knowledge will be developed describing and defining how a material deforms due to an explosion. The use of different characterized explosive materials makes the present research unique and more thorough than previous work. Ultimately, an improved scientific understanding of the controlling parameters in explosive blast research will be developed.

Chapter 2

EXPERIMENTAL METHODS

2.1 High-Speed Digital Imaging

High-speed Photron APX-RS digital cameras are used throughout this research for both shadowgraph and traditional imaging purposes. This camera is capable of recording 8-bit gray-scale images at incremental frame rates from 60 to 250,000 frames per second (fps). As the frame rate increases, the image size decreases from 1024x1024 to 128x16 pixel resolution. The camera stores images in a 16 gigabyte internal memory, which determines the length of time the camera is capable of recording. At most frame rates, approximately $3s$ of real-time images can be recorded. The camera has an electronic shutter that can be adjusted independently from the frame rate, up to a minimum shutter-open time of $1\mu s$. The camera has Nikon and c-mount lens attachments, of which only the Nikon mount is used in the present research. This camera interfaces with a laptop and "Photron FASTCAM Viewer" software via a fiber-optic connection. Through this connection, digital images can be saved in various formats for post-processing

The shadowgraph visualization, as discussed in Section 2.2.2, is typically recorded at either 36,000, 100,000, or $250,000 fps$ with shutter speeds of $1\mu s$. These frame rates are used because the rectangular fields of view allow the spatial and temporal resolutions to be maximized. The decrease in field of view with increasing frame rates results in the need to use a range of frame rates in several experiments to "piece together" the shock

motion over large distances. High frame rates are used to resolve shock motion near the explosive charge, and low frame rates are used to record the shock motion at large radius from the charge. The maximum shutter speed of $1\mu s$ is used to reduce smearing of the shock front across multiple pixels. Neutral-density filters are also typically used to further reduce the light entering the camera to prevent over-exposure of images. The number and strength of the neutral-density filters varies depending on the lens used. Typically a $30 - 80mm$ Nikon zoom lens is used with full-open aperture and maximum zoom. Aperture reduction does not work to adjust the image exposure in the present optical system, thus the neutral-density filters. For this optical system, aperture reduction just vignettes the image.

The measurement of material deformation, as described in Section 2.3.2, requires two of these high-speed digital cameras. The two cameras are synchronized so that they record their images at the same time. The process of synchronizing the cameras requires designating a "master" and a "slave" camera. The master camera sends a "trigger positive" signal through a "general output" BNC channel which is received by the slave camera through the "general input" channel as a "trigger positive" signal. Both cameras are set to the same frame rate and shutter settings, typically $36,000fps$ with $4\mu s$ exposure. Identical $50mm$ Nikon lenses with the f-stop set at 2.8 are used here, although these selections are relatively arbitrary. Higher f-stops could be used, which would increase the depth of focus of the cameras, but this requires more lighting than is currently available.

2.2 Gram-Scale Explosive Characterization

The first objective of this research is to define the energy release from two explosive materials formed into gram-size charges. The energy release will be characterized as described by Kleine et al. [7], by determining the shock wave radius as a function of time from the explosive charge. The definition of Kleine et al. will then be extended to include a description of the variation of explosive overpressure with radius. This section describes the experimental methods used to carry out these laboratory characterizations.

2.2.1 Description of explosive materials

Two different explosives, PETN and TATP, are used in the present study. Pentaerythritol tetranitrate (PETN), is a traditional military explosive commonly used in blasting caps [48]. PETN is used here because it is a well-documented explosive, it has been used extensively in large-scale blast testing, and its explosive characteristics are well known in terms of a TNT equivalence [48]. Triacetone triperoxide (TATP), is a "new" explosive material frequently used by terrorists [49]. TATP is included in this study in order to document the explosive behavior and estimate the explosive yield of this novel and non-ideal material. These two explosives are treated the same in the experimental setup, except that they are made and initiated in different fashions. Figure 2.1 shows a typical TATP ($left$) and PETN ($right$) charge.

PETN is synthesized in the laboratory following the simple procedure outlined by Urbanski [50]. The procedure, as given in Appendix A, produces PETN as a fine white powder precipitate which is then molded into explosive charges. The PETN thus

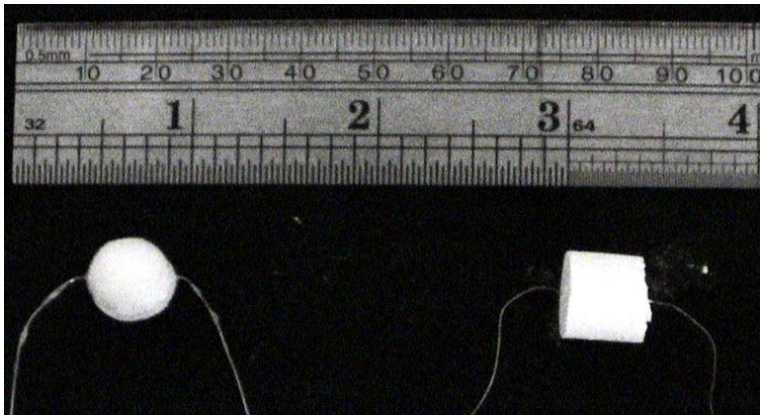

Figure 2.1. $1g$ TATP ($left$) and PETN ($right$) explosive charges

synthesized is at least 95% pure as determined by an x-ray diffraction analysis [51], as also discussed in Appendix A. The precipitated PETN is first ground using a mortar and pestle to produce a fine powder with an average particle size of about $15\mu m$ as estimated using an optical microscope. The PETN is ground to allow a greater packing density and because this was experimentally determined to produce more reliable charge detonations. Variation in the process of forming charges was found to greatly affect the reliability and reproducibility of explosions. The techniques outlined here were developed through trial-and-error methods until the resulting explosions were repeatable within a reasonable experimental error.

Ground PETN was mixed with 10% ground nitrocellulose on a per mass basis. Nitrocellulose, the primary component of smokeless powder [13], is used as a binder to hold the charge together. A 10% mixture was found to be the minimum binder percentage required to solidify charges enough to allow handling. Acetone is added dropwise to the PETN and nitrocellulose mixture until the proper consistency is obtained. The

acetone dissolves the nitrocellulose, allowing it to be combined with the PETN into a homogeneous mixture. Mimimal acetone is desired because it eventually evaporates out of the mixture as the charges solidify. It was found that large amounts of acetone solvent result in air-gaps within charges, decreasing the charge density and reliability of explosion. Typically about $1.5mL$ of acetone is added to a mixture of $9g$ PETN and $1g$ nitrocellulose, resulting in a homogeneous, flaky paste. The paste is then pressed by hand into cylindrical molds. As a secondary explosive, PETN is safe to handle and poses no danger as it is pressed into the charge molds.

Cylindrical charges were used in this research because of their ease of production. The resulting asymmetry is discussed in detail in Section 3.1.1. The cylindrical molds produced charges with length-to-diameter ratios of about 1 in an attempt to reduce asymmetries. $1g$ and $2g$ nominal charge masses were used in the present research. The $1g$ mold was made from a $9.5mm$ thick aluminum plate with a $10.7mm$ diameter hole. Two thin aluminum plates with $1.8mm$ diameter holes were used as the end brackets for the mold as shown in Figure 2.2. The end plates had several drilled holes to accommodate the initiation wire. As discussed below, the charges are initiated with a copper wire centered along the axis of the cylinder.

The molding process begins by securing the bottom plate to the mold and threading the initiating wire through the mold and the bottom plate. The initiating wire is a $0.15mm$ diameter single strand of copper wire, cut to about $0.1m$ in length for handling and attachment to the initiating leads. The PETN paste is placed into the mold and initially packed by hand until full. The paste is then pressed into the mold using a cylindrical rod and using "average human strength". Care must be taken with the

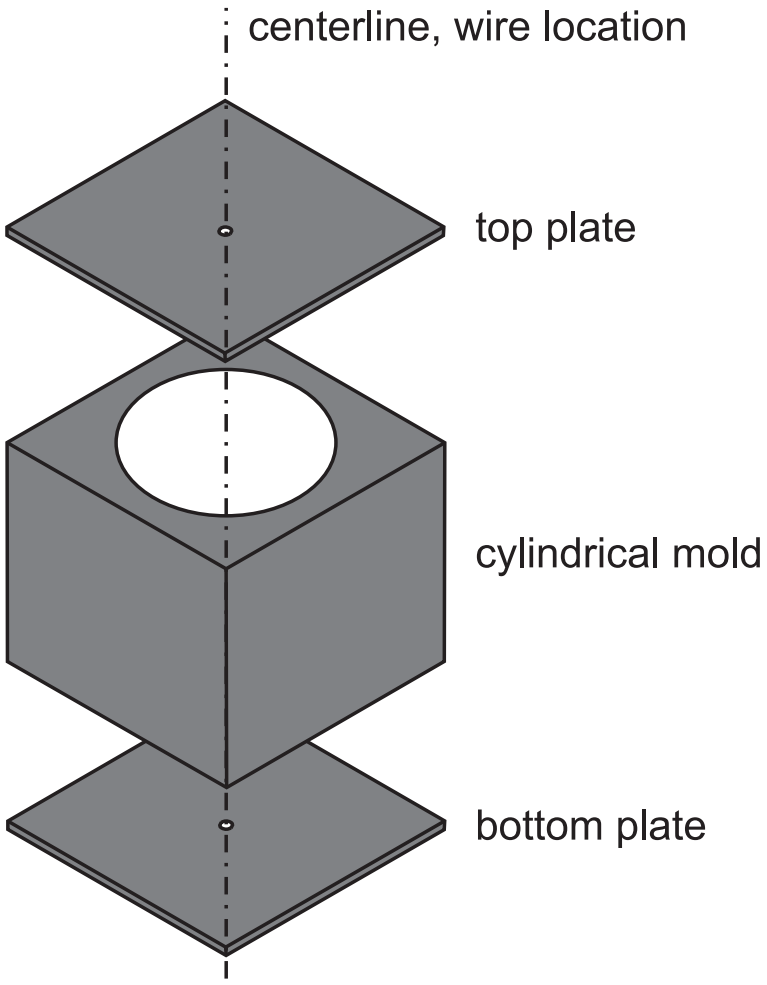

Figure 2.2. Schematic of PETN charge mold

initiating wire to ensure that it does not become crimped or severed and that it remains along the axis of the charge. The initiating wire must be on the axis of the charge to maximize symmetry, although experiments have shown that small deviations do not appear to affect the explosion beyond the normal experimental error. The top plate can then be placed over the mold, with the initiating wire threaded through the drilled hole, and clamped securely. The charges were typically left to dry in the mold for at least 12 hours before being pressed out using a cylindrical rod. Once removed from the mold, the charges were placed into an air-tight container with a silica packet for at least 12 hours before being used. The silica packet aids in drying the charge and appears to improve the ability to handle charges without excessive breakage.

PETN is a secondary explosive; it requires a shock impulse to initiate detonation within the material [13]. This shock is provided in the present experiments by an exploding bridge-wire initiator [48]. Bridge-wires are the primary method for initiation of civil and military blasting caps [52]. A bridge-wire is a thin metal wire through which a large current at high voltage is passed in a short time interval. The large current through the wire converts the metal to plasma, which expands rapidly, driving a shock wave [53]. The shock wave from the explosion of the wire initiates the detonation within the secondary explosive, in this case PETN, which then explodes with a much greater yield than the bridge-wire alone. In the present research two $30\mu F$ capacitors, wired in series, provided $15\mu F$ of capacitance which was charged to $4000V$. A thyratron switch allows this stored electrical energy to be released and conducted by 10-gage wire leads to the bridge-wire. The PETN charges are thus exploded from a control board approximately $7m$ from the charge and inside a safety shelter.

The bridge-wire diameter of $0.15mm$ used here was established by experiments to minimize the diameter, yet maintain strength in the wire for the production and handling of the charges. The initiating voltage is the same as that used in commercial and military bridge-wire initiation devices. The capacitance required represents the minimum amount of energy required to reliably explode the bridge-wire here, as determined through trial-and-error experimentation. Commercial devices typically have a smaller capacitance value, but also explode thinner bridge-wires of other materials [48]. For the thickness of copper wire used here, $15\mu F$ was experimentally determined to be the lowest capacitance for reliable initiation.

TATP is an extremely sensitive explosive made from acetone, hydrogen peroxide, and a catalyst [49]. Studies have shown that TATP explosions are not typical enthalpy-driven reactions, but rather entropy-driven explosions [54]. TATP decomposes rapidly to form primarily acetone and oxygen [55], producing four gas molecules for every molecule of solid TATP, resulting in a significant volume increase which drives the explosion [56]. This process is different from a conventional detonation-explosion reaction where the material reacts exothermically to drive a shock wave [57].

For the present research, TATP is synthesized by the Transportation Security Lab of the US Department of Homeland Security. Pure TATP is produced and mixed with 9.5% polyvinyl alcohol, by mass, as a desensitizer to facilitate handling and to effectively reduce the vapor pressure and volatility of the TATP [58]. The TATP is formed into hemispherical charges using a nitrocellulose binder. Two hemispheres are cemented together with nitrocellulose to produce spherical charges. Centered between the two hemispheres, along a diameter of the sphere, is the $0.15mm$ tinned-copper initiation

wire. The final charges are approximately 5% nitrocellulose, 9.5% polyvinyl alcohol, and 85.5% TATP on a per mass basis [59]. Nominal charge masses from $0.5g$ to $5g$ in $0.5g$ increments are used here, each made using hemispherical molds to obtain spherical charges.

As a primary explosive, TATP can be initiated with the addition of a small amount of heat or impact [13] and therefore does not require the complex initiation technique of an exploding bridge-wire. Here, the TATP is initiated by a hot-wire initiation technique [48]. A standard $12V$ automobile battery with 12 gage wire leads is connected to the initiating wire through the center of the charge. A simple switch is used to complete the circuit and explode the charge from a remote shelter.

2.2.2 Optical Imaging of Shock Waves

Shock waves can be imaged using various methods depending on the experiment scale and equipment available [24]. For the present research, the two methods used were the focused and retro-reflective shadowgraph methods. Shadowgraph techniques provide visualization of the second derivative of refractive index [24]. The shadowgraph method is preferred over schlieren for the present research because of its ease of setup and clear representation of shock waves. When using this technique to visualize shock waves, the shock appears as a dark band followed immediately by a light band. The light is bent from the leading edge to the trailing edge of the shock, i.e. toward the high-density region. The shock location in an image is therefore at the forward edge of the dark band opposite the bright band. Other details can be seen with these visualization techniques,

such as turbulence and combustion gases from the explosion, although these are not the focus of the present study.

The focusing shadowgraph technique is performed using a parallel light beam [24], and is the primary shock wave visualization technique for the present work. The layout for the z-type focusing shadowgraph system used here is given in Figure 2.3. The light source is a $200W$ xenon concentrated arc lamp manufactured by Newport-Oriel. The light source is placed at the focal point of the $0.76m$ $f/5$ mirror. Parallel light between the mirrors illuminates the test section, which is typically half-way between the mirrors which are approximately $10m$ apart. The second mirror focuses the light to a "point" and into the high-speed digital camera described in Section 2.1. The placement of the neutral-density filters is not critical for this optical technique, although they are always placed before the camera such that all light passes through them.

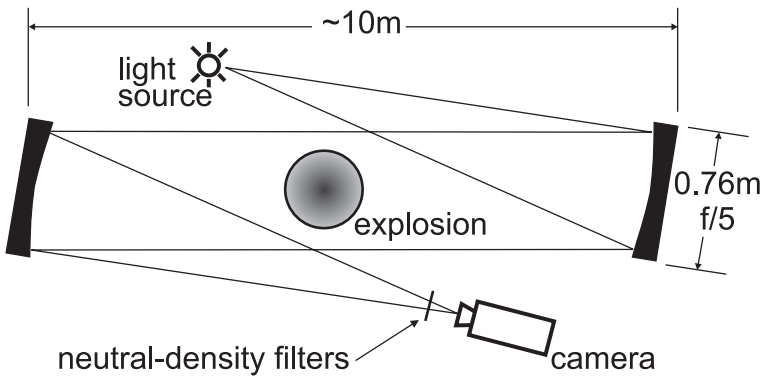

Figure 2.3. Schematic of the z-type focusing shadowgraph system

The focusing shadowgraph technique is used here for all measurement purposes because it sharply resolves the shock wave in the plane of focus, which is adjusted to be the plane of the charge centerline. In principle, the shadowgraph effect disappears at sharp focus; but shock waves are strong enough, and of enough lateral extent, to still be visible. The parallel light and single imaging plane results in a one-to-one relationship between distance measured within an image and actual distance in the measurement plane. No geometry correction is required for this technique, only a calibration image to relate pixel size to physical length is needed, as discussed in Section 2.2.3

The retro-reflective shadowgraph technique was originally developed by Edgerton for outdoor shadowgraph visualization [60]. The technique was improved upon by Settles et al. [61] to align the light source and camera axis in order to eliminate the double-shadow effect observed in the original work by Edgerton. The system developed by Settles et al. is used here for qualitative shadowgraph visualization and is shown in Figure 2.4. The light source is a $1000W$ xenon concentrated arc lamp which is focused onto a small mirror mounted in the center of the camera lens. The mirror is a cylindrical rod, cut at a 45° angle with the angled surface mirrored, which allows the light source to be off-axis from the camera. When the light is focused on the mirrored surface, it becomes effectively on-axis with the camera and expands to illuminate the retro-reflective screen. The $2.5m$ square screen reflects the light back to the camera, entering the lens around the rod mirror. With a small rod mirror in the center of the lens and the camera focused at long focal lengths or infinity, the occluded portion of the lens does not significantly distort or affect the final image.

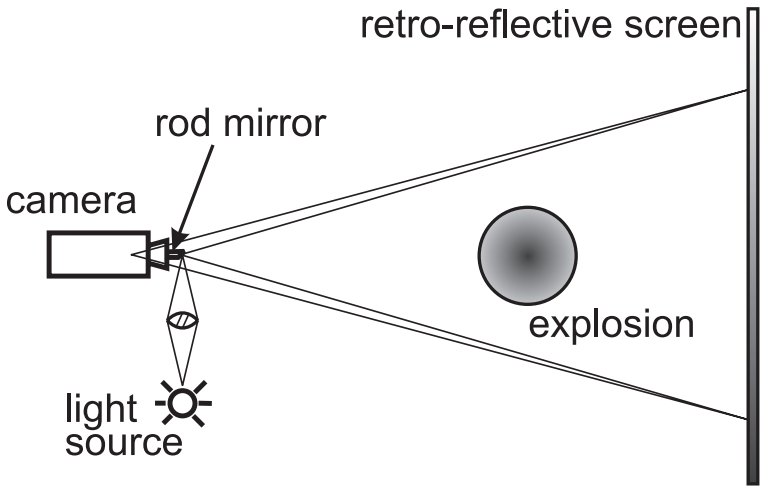

Figure 2.4. Schematic of the retro-reflective shadowgraph system

The retro-reflective shadowgraph technique is used here only as a qualitative tool for the symmetry measurements described in Section 3.1.1. The retro-reflective technique could be used to make quantitative measurements, but the images are not as sharp as those from the focused shadowgraph and a geometrical correction is required. Sharp images are desired for the digital image processing measurements, thus the focusing shadowgraph that produces better images is therefore used for measurements.

The geometric correction arises for the retro-reflective shadowgraph technique because this technique visualizes the shadow of the shock wave, projected onto the screen. The shadow forms only where the light source rays are perpendicular to the shock propagation direction. This location does not remain in a single plane for the case of a

spherical shock centered within the field of view. A simple geometric correction, however, can be applied if the distances from the camera to the screen and to the shock center are known [9].

2.2.3 Digital Image Processing for Shock Position

A MATLAB program was written to determine shock wave position as a function of radius from the center of an explosion. The program uses the gray-scale shadowgraph images from the Photron camera along with user input to determine shock wave position and thence velocity information. The main program and a typical user input file are given in Appendix B. Figure 2.5 shows a typical sequence of images that has been processed with the code. The top image shows the designation of the center of the explosion and the physical scale as discussed below. The rest of the images have the shock position, as determined by the program, highlighted in white on the bottom half of the images. This particular field of view, with the explosive charge off-center, is used to maximize camera resolution capabilities. The shock propagation is assumed to be spherical, as discussed in Section 3.1.1, thus only half of the shock propagation plane is imaged.

The first step in processing a sequence of images is to relate the measurement scale in the images to a physical size in the experiment, i.e. calibration. While the shadowgraph system is being used, a calibration image must be recorded for each camera zoom setting. The calibration image is a single frame, recorded with an object of known length positioned precisely in the plane of focus. The calibration object used here is a rigid sheet of metal, with a known width of $0.489m$, that is held perpendicular to the light in the focal plane of the shadowgraph system. A large calibration object is used

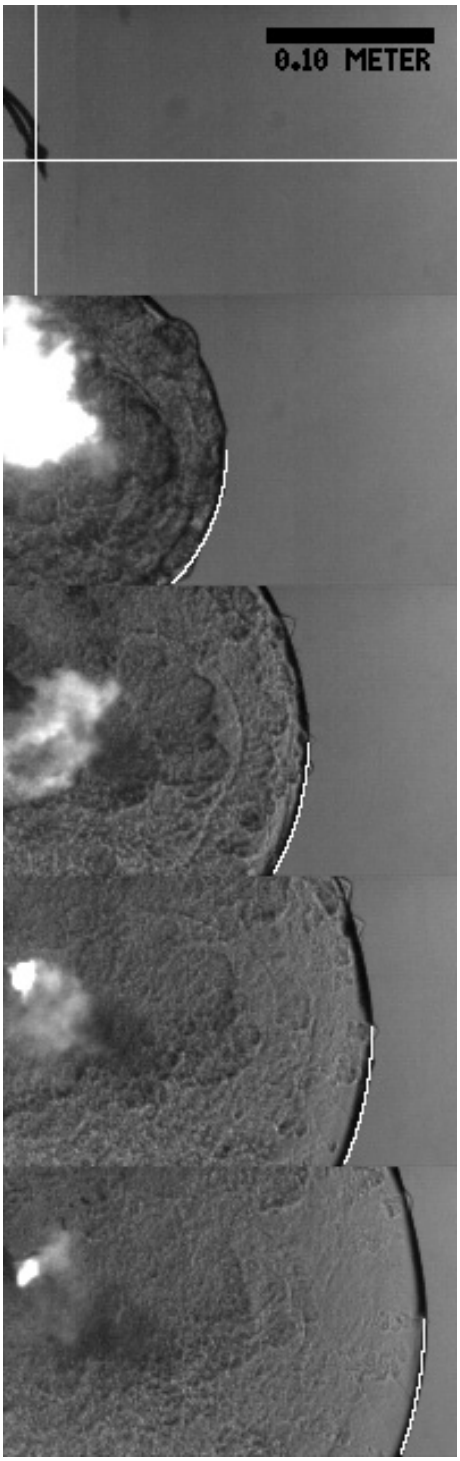

Figure 2.5. Typical sequence of images processed with the MATLAB shock detection procedure

to decrease measurement uncertainties, as is done in typical particle image velocimetry (PIV) techniques [62]. Using MATLAB, the calibration is completed by counting the number of image pixels corresponding to the $0.489m$ width of the metal calibration sheet. This ratio of pixels per meter is used to scale all pixel measurements within images to obtain actual shock position data.

The next step in the process is to define the center of the explosion. Small variabilities in the charges used causes the explosion to not always appear to originate from the physical center of the charge. To compensate for this it is important to place the explosion center at the center of origin for the spherical shock wave. The center used for the above sequence of images is shown in Figure 2.5 by the crossed white lines. The horizontal center is typically placed through the center of the charge because variabilities in this direction cannot be seen from the asymmetric field of view of the explosion. The vertical position is selected so that the curvature of the shock wave matches this apparent point of origin.

The program starts at the end of the image sequence and locates the shock wave as it propagates backward in time. Using the knowledge that the shock will appear as a dark circular arc in the image plane, the program looks for this feature. The program starts at the previous shock location, or edge of the image, and steps in single pixel increments toward the designated center. At each pixel distance from the center, the program creates an arc of pixels that are a uniform radius from the center. An average pixel intensity value for each arc is determined, where low intensity designates black. Since the shock is physically located at the leading edge of the dark arc in the shadowgram, the first arc of pixels with an average intensity lower than a threshold value

is determined to be the shock position in that frame. The threshold intensity value is set by the background intensity level, possible noise or fragments in the shadowgram, and program user experience. For ideal images, an edge detection sequence can also be used, although this is not typically needed. A manual shock location override is also built into the program for adjusting the shock position for individual images if required. Once the shock is found in one image, the next image is selected and processed accordingly until all images have been processed.

From the sequence of images, shock radius as a function of time is known. The radius measurements are fit by least squares to Equation 1.8. The equation is only fit to radius positions known with high confidence and no constraint at $t = 0$ is provided. The curve-fit is not forced through 0 because there is some uncertainty in when the charge is actually initiated, whereas the shock position change between two image frames is well known on both spatial and temporal scales. This variability can cause some discrepancies in the radius versus time plots, but data in terms of Mach number versus radius become independent of the initiating time. The radius versus time plot can also be shifted along the time axis slightly, without changing radius, in order to account for such variations. Later results show that the correct constraint for the curve-fit is to force the shock radius to be equal to the charge radius at $t = 0$.

Final program outputs, given in Appendix B, include shock position in each frame, several curve-fits, images, and a movie. The shock position data, including the curve-fit coefficients, are the most useful. Different curve-fit coefficients, as discussed in Section 1.2.1, are given so that the best fit to the experimental data can be used. The curve-fits also are given for both the scaled and un-scaled data, where scaled data refers to Sachs

scaling to $1g$ equivalent charges. The images produced by the data analysis include an $x - t$ diagram compiled from the centerline pixel row of each image in the sequence, as shown in Figure 2.6. The $x - t$ diagram is useful for examining the shock propagation and other wave phenomena throughout the event. Finally a movie showing the detected shock location in each image is given. This movie is useful for troubleshooting the data analysis process and ensuring that the MATLAB program correctly detected the shock front.

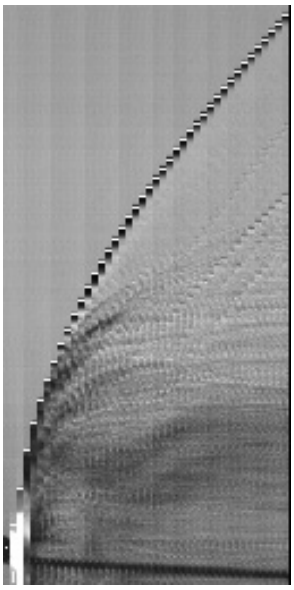

Figure 2.6. Sample $x - t$ diagram produced by MATLAB shock detection program

2.2.4 Pressure Gage Measurements

Another part of the explosive characterization process is the documentation of the overpressure duration variation with distance from the explosive center [1]. PCB Piezotronics model 105C13 pressure gages and a model 481 signal conditioner are used to measure the shock overpressure duration at various distances from the explosive charge. Gage output is recorded with a Tektronix TDS2000 digital oscilloscope and saved through MATLAB to a text file for post-processing.

Two pressure gages are used at once to obtain two point measurements from a single experiment. The gages are placed at discrete distances from the charge center and aligned within the plane of greatest symmetry, as discussed in Section 3.1.1. The gages are oriented face-on to the blast, as described by Rahman et al. [63]. This orientation requires that the gage face is perpendicular to the shock propagation direction at the measurement point. A typical pressure trace is shown in Figure 2.7. The pressure gage output is noisy but maintains the general shape and characteristics expected and described by Figure 1.1. The trace is filtered digitally using a MATLAB $100kHz$ low-pass filter to reduce the high frequency noise. Gage inertia affects the ability to accurately capture the pressure rise at shock incidence [1], thus the Rankine-Hugoniot relationship and optical measurements are used to determine the maximum pressure for ideal gas conditions [64]. This approximation of an ideal gas will fail close to the explosive charge. The pressure units on Figure 2.7 therefore remain uncalibrated since the gage traces are used only for determination of the positive overpressure duration as defined by Kinney and Graham [1].

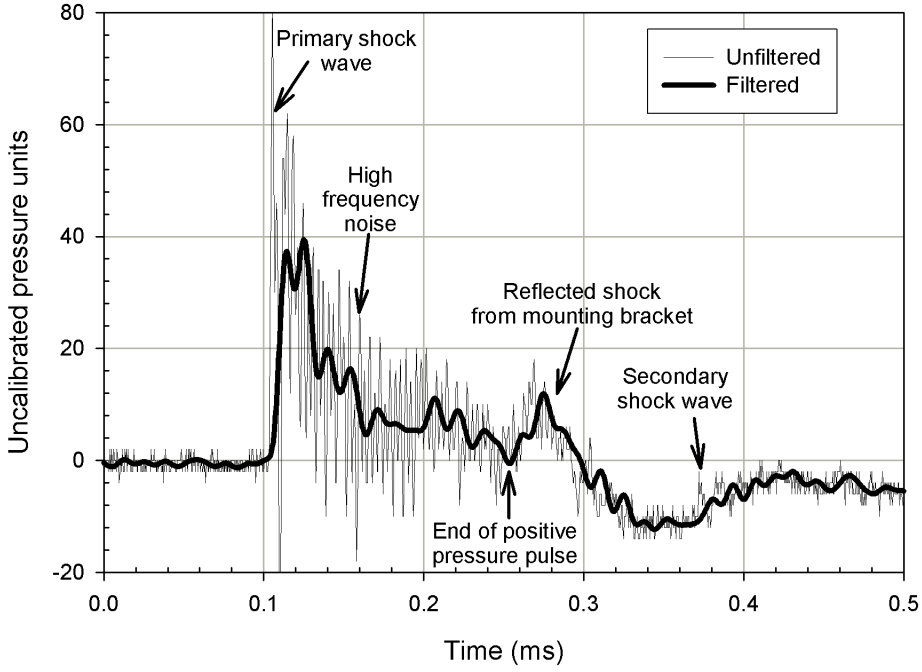

Figure 2.7. Typical pressure gage output used for measuring overpressure duration

The pressure gage output as shown in Figure 2.7 shows other interesting phenomena, including a reflected shock, secondary shock, and the negative pressure phase. The reflected shock wave indicated in the figure is from the bracket used to mount the pressure gage. This reflected wave does not interfere with the primary measurement, since only the data between the initial pressure rise and the start of the reflection are used in calculations of the overpressure duration. The pressure rise from the secondary shock is insignificant compared to that from the primary shock. The location of the secondary shock was verified by comparing the time of arrival from the pressure trace with an image sequence showing the secondary shock passing the pressure gage. The negative pressure phase occurs when the pressure is less than atmospheric pressure and is ignored in all present calculations [2]. The shape of the pressure signal throughout the negative pressure phase is also distorted in the present measurements due to the influence of the reflected wave.

Although the present pressure signals are noisy and imperfect, the data can nonetheless be used to determine the overpressure duration. Some of the experimental noise and irregularities could be a result of the small explosive charges used and small abnormalities within the shock front. Typical large-scale tests do not show this same level of gage noise [17, 65], most likely due to the large distances between the charge and the gages. Large distances allow the shock front to become smooth and the ratio of the gage face dimension to the blast radius to decrease, improving the ability to accurately make a point measurement.

2.2.5 Computational Modeling of Explosions using AUTODYN

The commercial software package AUTODYN, from ANSYS, is used here to model the explosions of TNT and PETN. These computational simulations are performed to support the experimental results and to test the scalability of the gram-scale charges used here. Other researchers [66] have used AUTODYN to model shock wave motion with apparent success. Thus, AUTODYN is used here to model scenarios similar to the experiments performed in the present research.

A $1kg$ TNT explosion is simulated to validate the computational model before investigating the PETN explosions of primary interest here. The $1kg$ charge is modeled in order to allow a direct comparison with the standard TNT data [1], which is later used for determining TNT equivalence. By performing the computations on $1kg$ charges, potential charge-size limitations on the equation of state can be avoided. The equation of state, as discussed below, is based on experimental data and therefore may not be applicable for gram-scale explosions because this topic has been little investigated until the present study. The experimental PETN data collected here at the gram-range are scaled up to $1kg$ charge results, as discussed in Section 1.2.1. Through this process the experimental results can be compared on both the small and large scales simultaneously.

AUTODYN is a versatile software package capable of explicitly modeling the non-linear dynamics of fluids and solids, including fluid-structure interactions [67]. For the present work, the application of the code is limited to solving the Euler equations describing inviscid flow in an explicit, finite-volume, one-dimensional, radially-symmetric formulation. The equations of mass, momentum, and energy are supplemented with

equations of state for air and the gaseous explosion products. The air is modeled as an ideal gas, and the explosive materials are modeled with the Jones-Wilkins-Lee (JWL) equation of state. The JWL equation of state is an empirical expression used to define the pressure-volume relationship for detonation products [68]. This equation relies on six parameters to define the pressure-volume-energy relationships for detonation and combustion products. The required parameters used here are those built into the standard AUTODYN package, which have been validated against archival explosion data.

The one-dimensional, radially-symmetric computational domain is shown in Figure 2.8. One-dimensional problems are represented as "wedges" by AUTODYN, as seen in the figure. The wedge represents the radially symmetric domain, showing a simulated planar angle, θ, even though no angular variations exist. The explosive material is positioned at the apex of the wedge, the explosion and resulting shock wave thus propagate from the apex toward the open end. The open end is modeled as an outflow boundary condition to allow the air to exit after being accelerated by the shock wave. The domain is modeled out to a radius of $3m$ and consists of 3000 equally-spaced cells, providing a grid resolution of $1mm$. This chosen domain resolution was determined from a simple grid-independence study in order to provide a balance between computational time and accuracy.

The air portion of the domain is modeled as a standard atmosphere as defined in Section 1.2.1. Thus computational results can be compared directly to scaled experimental results. The explosive material is fills a region representative of the radius of a $1kg$ explosive charge at standard packing density. The resulting explosive radii are $53mm$ and $51mm$ for TNT and PETN respectively. The detonation is initiated at the charge

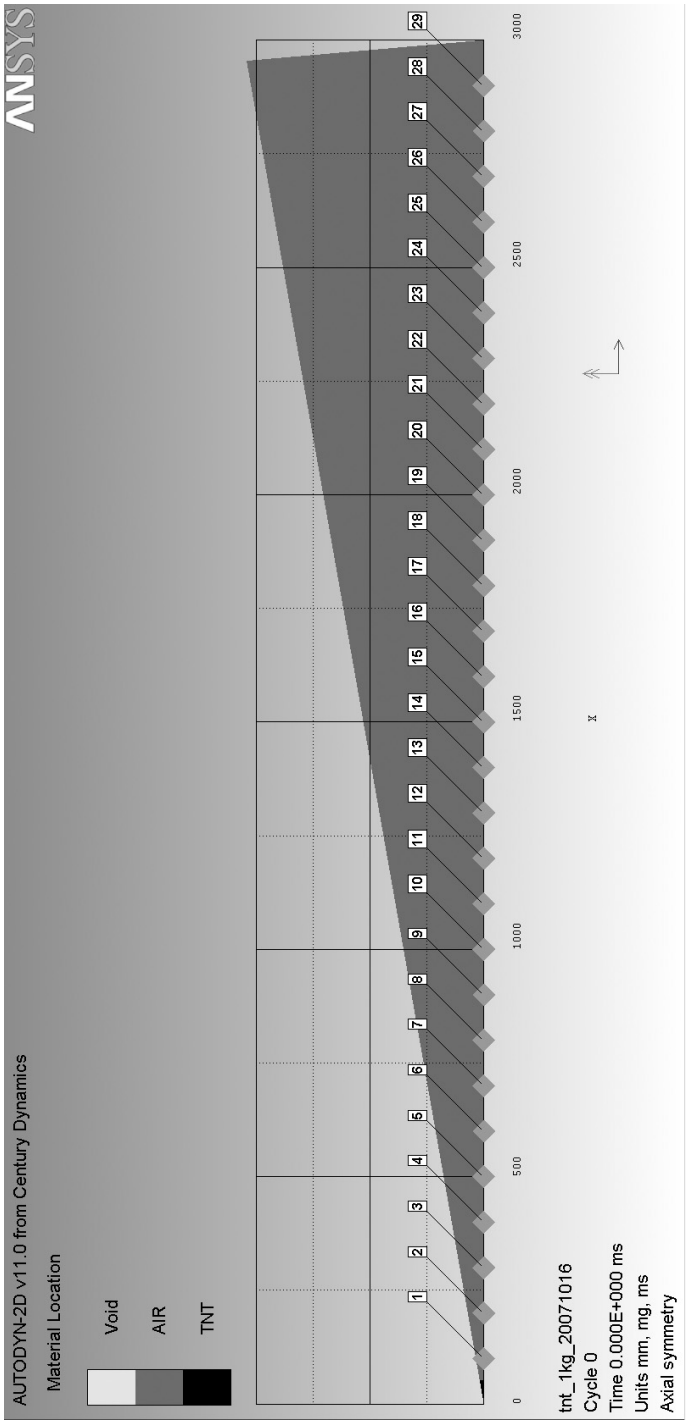

Figure 2.8. Computational domain for present explosion simulations in AUTODYN, showing pressure gage locations

center using the Lee-Tarver model, which assumes a combined ignition and expansion process, tuned with coefficients to match experimental data over a wide range of radii from the explosive [67].

Within the computational domain, 29 simulated pressure gages are positioned every $100mm$ starting $100mm$ from the charge center. The pressure gage locations are labeled in Figure 2.8 and are represented by diamonds on the radial axis. Each pressure gage records the local static pressure as a function of time from the initiation of the detonation until the end of the simulation. The gage records are used to determine the shock time of arrival, maximum overpressure, and time of pressure return to atmospheric at each location. These data yield shock wave radius versus time, shock Mach number versus distance, and overpressure duration versus distance, respectively.

The contact surface between the explosion products and ambient air is modeled as a material interface. This material interface is not recored by the pressure gages, but is recorded on computed images at regular time intervals during the simulation. These images, showing the domain and material locations, as in Figure 2.8, are used to determine the contact surface location as a function of time. Initially this was not a parameter of interest, but later became one due to the overpressure duration results to be discussed in Section 3.1.6.

2.3 Material Blast Research

The second primary objective of the present research is to develop the techniques required for measuring material responses to explosive impulses. This research is dependent on accurate characterization of the explosives used and on high precision measurement of material deformation. A characterized explosive is exploded at a known distance from a thin aluminum plate, deforming the plate due to explosive impulse. Optical techniques are used to measure the time-resolved, three-dimensional surface shape of the deforming plate throughout the explosive event. The experimental techniques and apparatus described here are the basis for all material research presented.

2.3.1 Material Blast Test Setup

Aluminum alloy 3003, $0.406mm$ thick, was selected because it is readily available and its static and low-speed properties are well-documented, making it an ideal material for initial high-speed blast deformation research. A single plate of aluminum is bolted into the fixture shown in Figure 2.9. This fixture was designed in order to conduct research similar to military "shock-hole" tests [69]. The fixture is made of aluminum, $0.02m$ thick and $0.46m$ square.

The exposed portion of the aluminum plate is a $0.25m$ diameter circle and is centered on the plate. The rest of the plate remains firmly clamped within the shock-hole fixture by the 12 symmetrically arranged bolts, which are hand-tightened with a crescent wrench. This fixture is a second-generation design developed to reduce wrinkling and pulling of the test plate at the clamped boundary. The original fixture design used

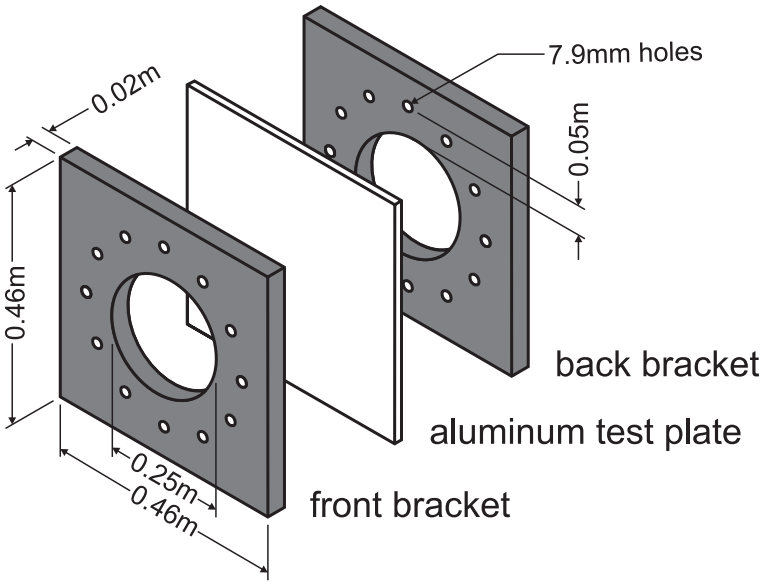

Figure 2.9. Schematic of "shock-hole" fixture

only 4 bolts and $0.30m$ plates with the same exposed area. The original experimental plates showed a wrinkling of the aluminum along the boundary and pulling marks around the bolts. The new fixture design better clamps the plates and appears to eliminate all wrinkling and material motion from the clamped region into the deformed area.

The plate fixture was also designed to provide the optical access required to make deformation measurements. The deformation measurement, as described in Section 2.3.2, requires two cameras to image the plate surface as it is deforming. The complete setup for the present material deformation research is shown in Figure 2.10. The plate fixture location relative to the cameras is fixed and the "stand-off distance" from the plate surface to the center of the explosive charge is the primary research variable. As the stand-off distance is changed, the explosive impulse applied to the plate is varied. The face of the plate nearest the explosive will be referred to as the "front" of the plate and the "back" will indicate the face being imaged by the cameras.

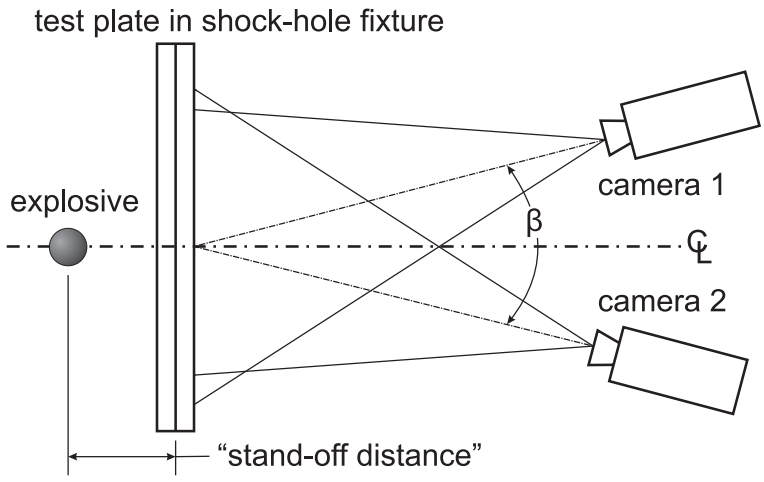

Figure 2.10. Experimental setup for material deformation research

By placing the characterized explosive at a given stand-off distance from the plate, the explosive energy is coupled to the plate through the atmosphere. This technique is different from that of Nurick et al. in which the explosive energy is conducted to the plate through a foam material in contact with both the explosive and plate itself [25]. The present technique is used because shock propagation through air is well documented, and this also allows direct application of the explosive characterization developed here.

For a given stand-off distance, the explosive impulse upon the test plate is determined from the measured shock Mach number and overpressure duration at the radius from the charge equal to the stand-off distance. The actual impulse described in Section 1.2.1 is not used here, but rather a triangular impulse approximation is used [1]. Figure 2.11 shows the actual impulse as the cross-hatched region and the triangular impulse approximation as the gray area. At any stand-off distance the impulse is known from measurements made during the explosive characterization procedure.

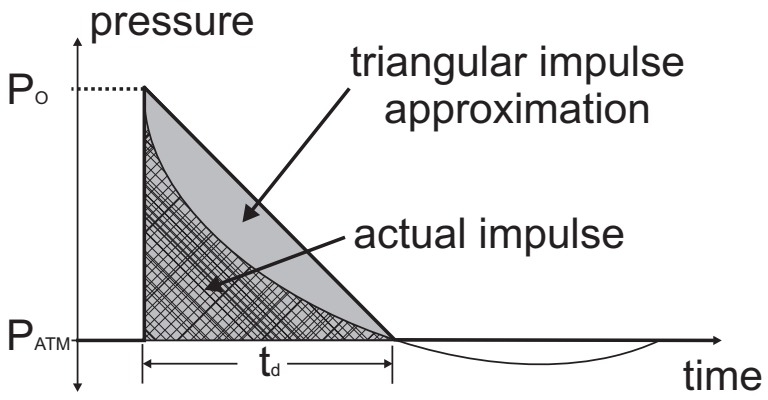

Figure 2.11. Pressure-time history of an ideal, explosively driven shock wave showing actual and triangular approximation of explosive impulse

The actual impulse is not used because the actual pressure decay is not precisely known. The measured pressure duration profiles include significant noise, therefore limiting the ability to determine the actual impulse. With improved pressure duration measurements, the actual impulse could be used. The present approximation procedure over-estimates the applied impulse, but all observed trends with impulse are expected to hold if the actual impulse is used.

2.3.2 Stereoscopic Digital Image Correlation

Commercial software by Correlated Solutions is used in the present research to measure test plate material deformation [70]. This software uses simultaneous images from two cameras in parallax to digitally measure an actual surface of arbitrary shape. With the use of digital high-speed video cameras, a time-resolved shape history can be created and deformation information thus inferred.

The first step in using this software is to perform a calibration for the orientation of the cameras relative to each other and the field of view. The two cameras must be positioned so that they both image the desired field of view, in this case the back side of the plate. The cameras are placed at a given angle, β, relative to each other as shown in Figure 2.10. This angle should be approximately $20^\circ \leq \beta \leq 40^\circ$ in the plane shown. The stereo calibration accounts for this primary stereo angle and also the corresponding angles in the two other planes, which are arbitrary and are approximately zero in the present research.

The calibration procedure requires at least seven images of a standard pattern, printed on a rigid board, which is moved and rotated throughout the field of view. The

calibration pattern is provided by Correlated Solutions and consists of a series of circles with precisely known size and distribution, including three with white centers. The software uses the images from each camera to triangulate the location in space of each dot on the calibration pattern in each image pair. A sample image pair, shown in Figure 2.12, shows the differences in field of view and orientation between the two cameras. From a series of calibration image pairs, the focal length, camera orientation, and pixel size calibrations are performed for the system. Once calibrated, the system can be used to make precise measurements within the field of view.

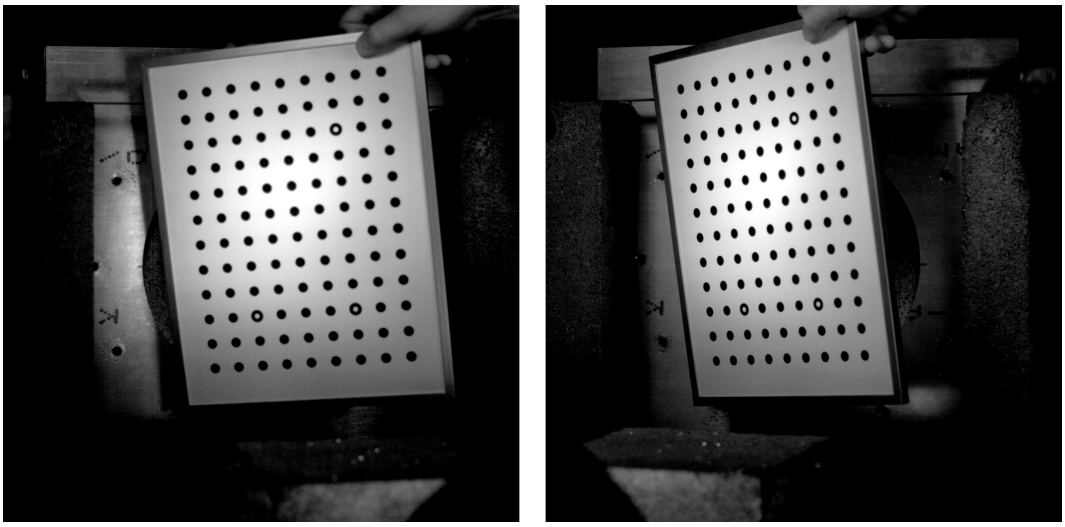

Figure 2.12. Typical image pair with calibration pattern in the field of view

A calibration is required whenever the cameras are moved or if the lens focus is changed. Typically, a calibration is performed at the beginning and end of a series of experiments. Occasionally, the data reduction procedure from a single test implies that

the previous calibration is no longer valid, in these cases a new calibration is performed immediately, and the data are reprocessed. The calibration could become invalid due to camera movement caused by the explosion or human contact with the setup.

Once calibrated, the software is able to interpret where in space an object is located, based on its appearance from the two camera perspectives. In order to make measurements on a surface, the surface is painted with a high-contrast random dot pattern. The random dot pattern provides unique regions across the surface that can be identified and analyzed by the software. The analysis algorithm uses an interrogation window to compare the dot pattern between the two images of a pair and infers the shape of the surface from differences in dot appearance between the two images. Ideally the dot pattern contains dots of about 5 pixels in area, compared to square interrogation windows of side lengths 11 to 19 pixels for the present work. Larger interrogation windows can not resolve small details but are more robust and less likely to produce erroneous results. The interrogation window sizes used here are selected to balance resolution with robustness so that all experiments can be processed with the same approximate interrogation window size. Overall the general results are independent of interrogation window size, which should be set as needed for each experiment.

The random dot pattern is applied to the back side of each aluminum plate before being placed into the test fixture. The plate surface is first roughened by lightly sanding with 100 grit sandpaper. The plates are then painted with a white base coat of "Plasti-Kote Sandable Primer" spray paint. Once the base coat is dry, a black spray paint is used to create the random dots. The dots are created by lightly depressing the spray nozzle such that the paint is ejected in spurts, instead of a continuous spray. Commercial trigger

handles that attach to the top of spray paint cans can be useful to simplify the process. The final dot pattern should have a large quantity of dots, of the appropriate size, across the area to be analyzed. Figure 2.13 shows the dot pattern on a plate surface as seen from the two cameras. The field of view shown is typical of all present experiments and focuses on the centerline of the plate to maximize the spatial and temporal resolution capabilities of the camera. The shock-hole plate fixture edge can be seen in the images. The horizontal marks on the fixture indicate the horizontal diameter of the opening, and are used for centering the cameras and field of view.

The plate fixture is illuminated with three, $600W$ continuous Calumet flood lights. The lights are positioned at oblique angles to the plate surface to decrease glare reflection from the plate into the camera lens. The illumination was experimentally chosen to fully and evenly illuminate the plate surface and allow camera shutter speeds as short as $4\mu s$, to decrease image blur during the explosive event. Greater illumination, if available, could be used and would allow an increase in lens f-stop and a further decrease in shutter speed. Trial-and-error methods with the dot pattern show that black dots on a white field requires less illumination than the opposite, and are therefore used throughout the present work. Illumination requirements change with camera settings, field of view, choice of lens, and f-stop settings.

Each plate deformation experiment includes the recording of image pairs of the plate surface as it deforms and a single image pair of the final plate shape after all vibration has stopped. A portion of the image data set is processed immediately following an experiment to ensure a proper camera calibration and to determine the explosive impulse conditions for the next experiment. In the present research the primary data

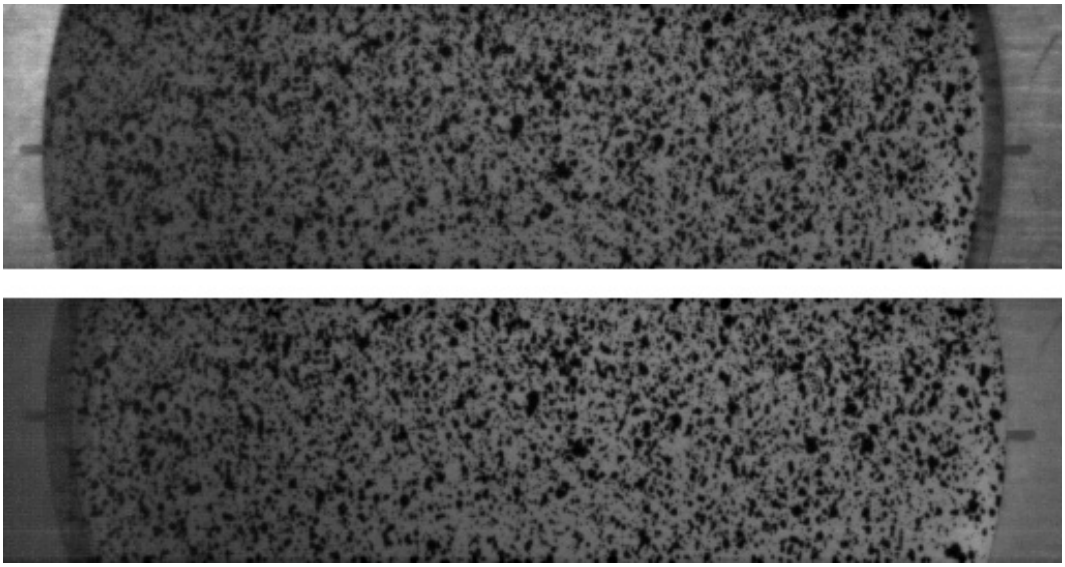

Figure 2.13. Typical image pair showing the random dot pattern and field of view for a standard experiment, the distance between the horizontal marks on the shock-hole fixture is approximately $0.25m$

examined are the maximum and final deformations of the plate surface along a diameter in the field of view. Initial experiments with full plate imaging showed a high degree of symmetry in the deformation and vibration of the plate, therefore only a portion of the plate surface is imaged and analyzed.

Chapter 3

RESULTS AND DISCUSSION

3.1 Gram-Scale Explosive Characterization Results

Pentaerythritol tetranitrate, PETN, and triacetone triperoxide, TATP, have been characterized in terms of shock Mach number and overpressure duration versus radius profiles. This characterization has been performed for a range of explosive charge masses and has been shown to scale among experimental and computational results.

3.1.1 Symmetry of Explosions

The explosive characterization procedure is based on determining shock wave radius versus time for explosions of different materials. Shock propagation from an explosion can be assumed to be spherical according to Huygen's Principle [71], but cylindrical explosives are known to produce more complicated shock propagation patterns [21]. In order to determine the degree of asymmetry for the present research, simultaneous shadowgraph visualizations were performed from perpendicular directions. These experiments used both the z-type focusing and retro-reflective shadowgraph systems described in Section 2.2.2 to obtain images of shock propagation in two perpendicular planes. A schematic of the setup of the combined system is given in Figure 3.1.

The two high-speed digital cameras were synchronized, as discussed in Section 2.1, to provide simultaneous imaging. A sequence of images from one experiment with

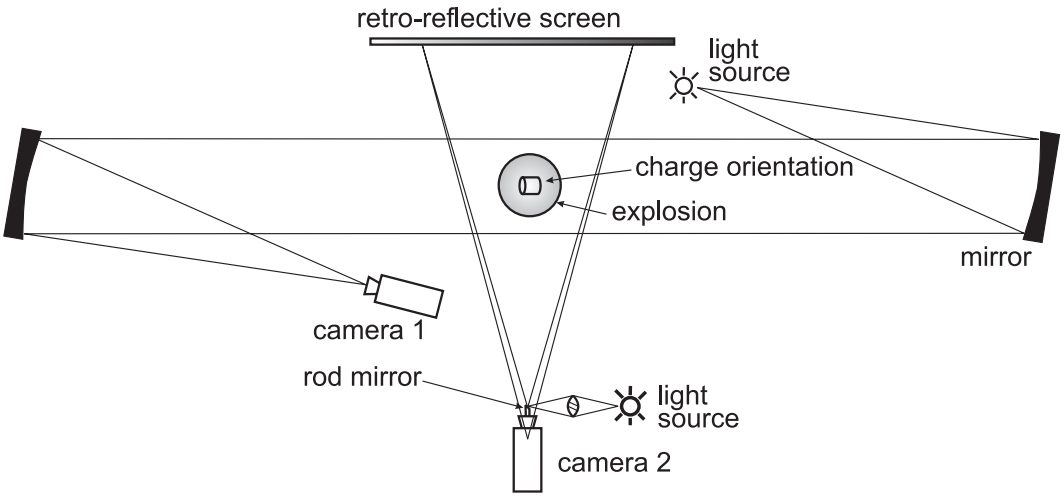

Figure 3.1. Schematic of the combined shadowgraph systems used to produce simultaneous perpendicular shock wave visualization

a $1g$ PETN charge is given in Figure 3.2. The cylindrical PETN charge was oriented with the axis of the cylinder along the optical axis of the z-focused shadowgraph system. The retro-reflective shadowgraph system recorded the shock propagation in the plane of the charge axis. The images on the left in Figure 3.2 are from the z-focused system, and those on the right are from the retro-reflective system. The frames shown are $67\mu s$ apart.

The images in Figure 3.2 show, among other things, the differences between the focused and retro-reflective shadowgraph visualization techniques. The focused shadowgraph images are sharper and show more detail, as expected [24]. The retro-reflective images are less sharp and not as detailed, though the shock front is still clearly visible. The images were scaled so that the length scales in both image planes are the same [9].

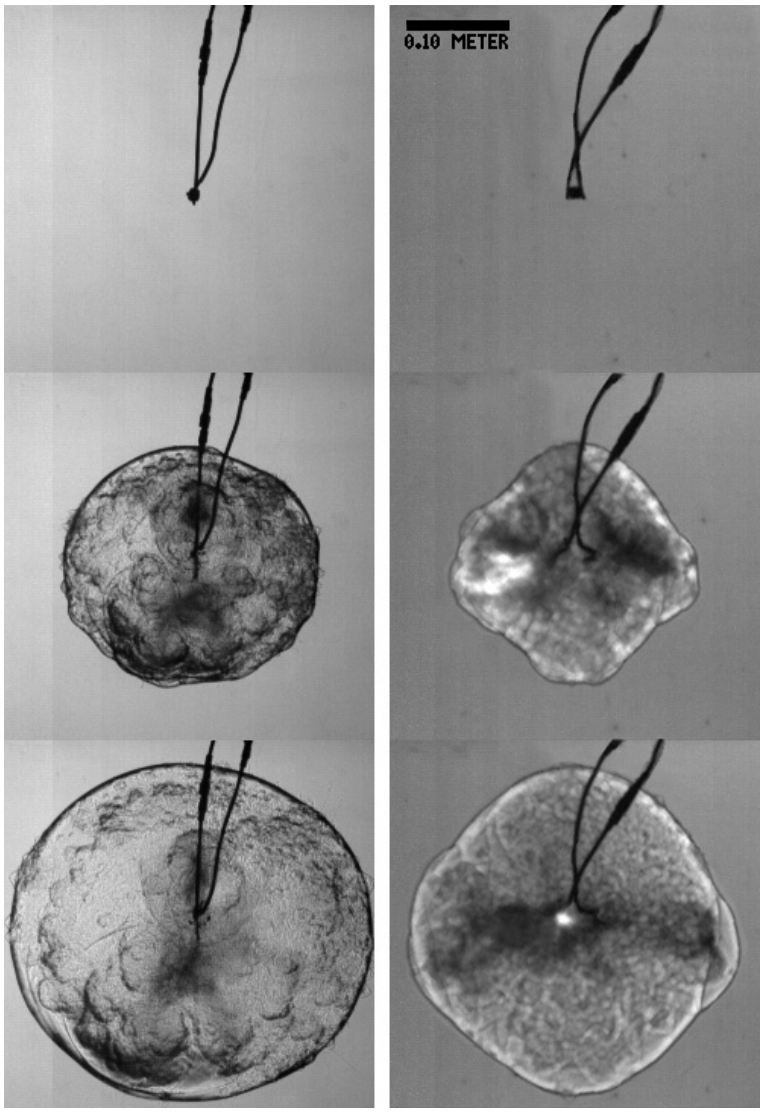

Figure 3.2. Simultaneous images from the z-focused ($left$) and retro-reflective ($right$) shadowgraph systems showing shock wave asymmetry for $1g$ PETN explosion in the radial and axial planes, respectively

The two views of the shock wave propagation provide an estimate of the degree of spherical symmetry. Shock propagation in the radial plane, perpendicular to the charge axis, is shown to be almost perfectly circular. This plane is expected to be symmetric and is the plane in which all shock wave measurements are made. Small local disturbances and turbulence can be seen at the shock front, these small irregularities potentially contribute to the noise in the pressure gage measurements discussed in Section 2.2.4, but do not affect the full-field shock propagation. A few small fragments can also be observed traveling supersonically, ahead of the blast wave. These fragments represent unexploded material, likely binder, that is propelled by the explosion process. Care is taken in the production of charges and reduction of data to ensure complete explosions so that particles do not interfere with any measurements, experiments where excessive particles are observed are rejected.

The axial plane shadowgraph in Figure 3.2 shows asymmetrical shock propagation and a residual shock shape reflecting the cylindrical shape of the charge. The shock shape is the same as that shown schematically by Held [21]. The asymmetry, however, decreases as the shock propagates away from the charge, resulting in a nearly-circular shock within $0.15m$ from the charge center.

The shock asymmetry in the present work is less severe than that documented by Kleine et al. for their experiments [7]. The present work initiates the explosive charge along the cylinder axis, instead of the laser initiation at the end face used by Kleine et al. [7]. The shock propagation asymmetries documented here and by Kleine et al. are directly related to the charge initiation techniques and explosive charge shapes. In order to produce the most symmetric shock propagation, spherical charges with central

initiation should be used. Spherical PETN charges, however, were not used here due to charge production constraints.

The spherical TATP charges used here show no noticeable asymmetry when examined in the same manner as in Figure 3.2. The shock propagation is circular in both planes and there are almost no particles or irregularities along the shock front. The TATP is initiated at an unknown position along a diameter of the sphere, but this does not appear to affect the resulting shock symmetry. The spherical charge shape with initiation along a diameter thus represents the ideal charge configuration and should be used whenever possible.

3.1.2 Experimental Shock Radius versus Time

Characterizing and predicting the effects from an explosion requires an understanding of the changes in physical properties following the explosion. The shock wave produced by an explosion propagates through the ambient air and causes changes in local pressure, density, and temperature which can be calculated based on typical gas-dynamic assumptions [10]. The classical similarity solution for a point energy release and strong shock wave formation by Taylor predicts the motion of the shock wave and the resulting physical property distributions [15]. This ideal prediction however cannot be directly applied to typical explosions where the energy is released over a finite time. These real explosions are better analyzed experimentally by measuring shock propagation or property variations then applying scaling laws. Here, the shock propagation is measured from the center of the explosive as a function of time and becomes the primary data for developing an explosive characterization.

As described in Section 2.2.3 and shown in Figure 2.5, the shock radius versus time is determined from a set of digital shadowgraph images using a MATLAB data reduction program, presented in Appendix B. Approximately 20 charges of each material were exploded and analyzed in order to precisely determine the shock radius versus time. These 20 experiments, however, represent only a fraction of the total number of experiments, of which some were rejected due to particles or irregularities at the shock front which prevented accurate data reduction. The large number of experiments was required to determine the experimental error and to obtain measurements over a large range of radii. Multiple camera frame rates were required in separate explosive events to measure the shock propagation through different radius regimes. These results were then combined to obtain the final data set.

Sample data for the shock radius as a function of time from PETN charges are given in Figure 3.3. The data are for charges of varying mass, produced from the cylindrical molds discussed in Section 2.2.1. The charge masses are slightly less than the nominal mold masses because some mass is lost when the charges are removed from the molds. Mass can also be lost during the transport and handling of charges before an experiment. The actual charge mass is measured just before an experiment.

The size of the symbols in Figure 3.3 represent the approximate uncertainty in the measurements. The uncertainty in radius is primarily due to pixel resolution within the camera and field of view. The MATLAB program determines the shock position as a given pixel location, thus the uncertainty is approximately ± 1 pixel. The physical size representationed by one pixel is calculated as described earlier in Section 2.2.3. Time

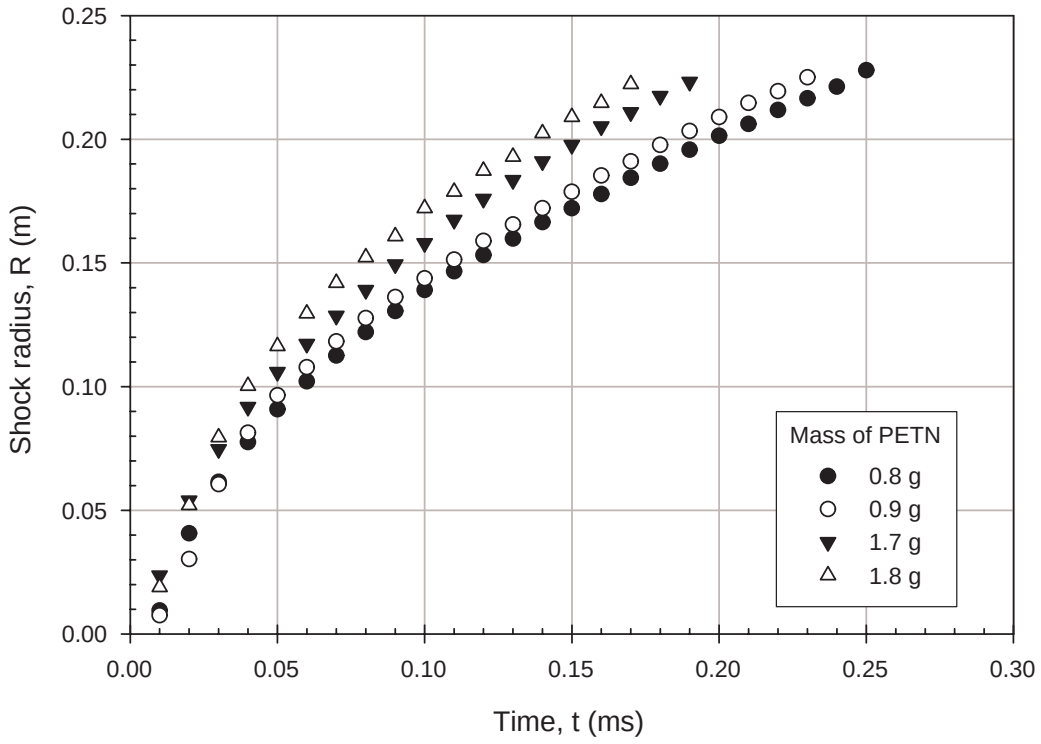

Figure 3.3. Measured shock radius as a function of time for PETN charges of varying mass

uncertainty is generally less than half the time between frames and is not explicitly explored here in general.

However, one aspect of time uncertainty that is investigated is the determination of the shock radius limit as time approaches zero. A time difference is accurately known for the measurement of radius changes between frames, but the instant of charge initiation cannot be determined. The shadowgraph images do not show the actual initiation of the charge, but rather the shock as it emerges from within the solid explosive. The charge initiation occurs in a very short time and is less than the smallest time increment measurable with the current cameras. The initiation of a charge can only be estimated to within one time-step of the camera frame rate for that experiment. The shock radius versus time data therefore can be shifted along the time axis slightly to account for this uncertainty. This analysis is explored by the comparison of experimental data to computational predictions for PETN, as presented in Section 3.1.6.

The same type of measurements of shock radius versus time have also been made for TATP. Figure 3.4 shows shock propagation results from four sample TATP charges. Again the approximate uncertainty is represented by the symbol size in the figure. A larger range of charge masses than before was used for TATP because of its lower TNT equivalence, as determined and discussed in Section 3.1.3. The lower yield of TATP allowed larger-mass charges to be safely exploded in the experimental facility.

Figures 3.3 and 3.4 both show that larger explosive masses create shock waves that propagate faster than those from smaller masses. This simple result is expected since a larger explosive mass, produces a larger energy release. In order to compare these experiments of different-mass explosives, each set of experimental data must be

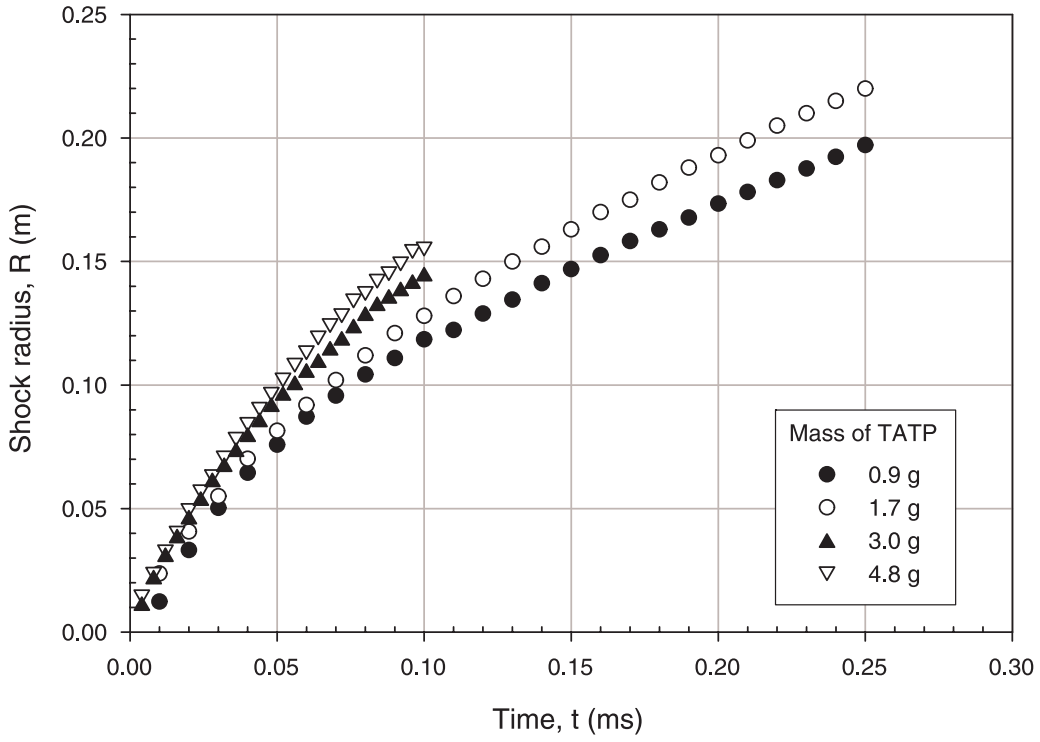

Figure 3.4. Measured shock radius as a function of time for TATP charges of varying mass

scaled according to the scaling laws discussed in Section 1.2.1. With the application of scaling laws, experimental data with variable charge masses of a particular explosive can be evaluated at a standard charge mass. For the present work the standard charge mass is $1g$, and all experimental data are scaled to this value. Results of scaling the data in Figures 3.3 and 3.4 are given in Figures 3.5 and 3.6 respectively.

Figures 3.5 and 3.6 show only a fraction of all the experimental data obtained for each explosive material. All data collected for each explosive material collapses to a single shock radius-versus-time curve when scaled to represent $1g$ charges of that material. The scaled data are fit to Equation 1.8 and used to determine the shock wave Mach number versus radius as discussed in Section 3.1.3. The curve-fit coefficients for PETN and TATP, as experimentally determined here, are given in Table 3.1. The curve-fit equations are valid for the range of data presented in Figure 3.7. The curve-fit coefficients also reflect the adjustment made for the shock radius originating at the charge radius for $t = 0$ as discussed in Section 3.1.6. The curve-fits are used here to simplify data manipulation and to provide an algebraic representation of a large total data set.

Table 3.1.
Experimentally determined curve-fit coefficients for PETN and TATP

Explosive	**A**	**B**	**C**	**D**
PETN	-0.009434	1.000	-1.268	0.9317
TATP	-0.01071	1.000	-0.8768	0.6959

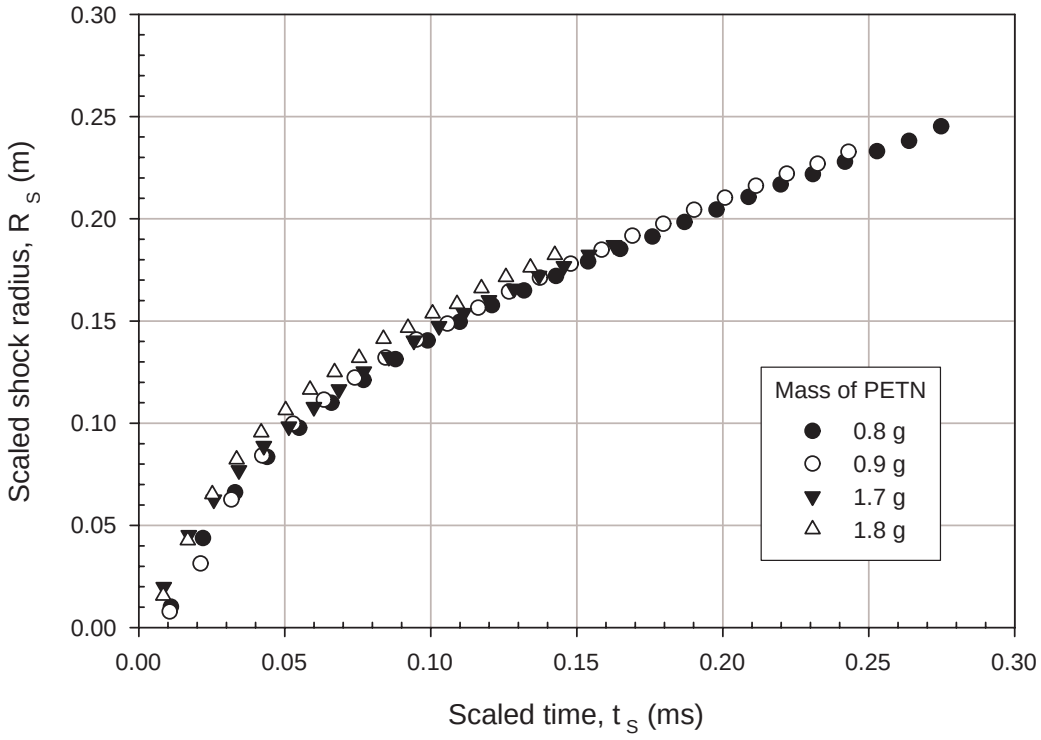

Figure 3.5. Scaled shock radius as a function of scaled time for PETN charges of varying mass, scaled to $1g$

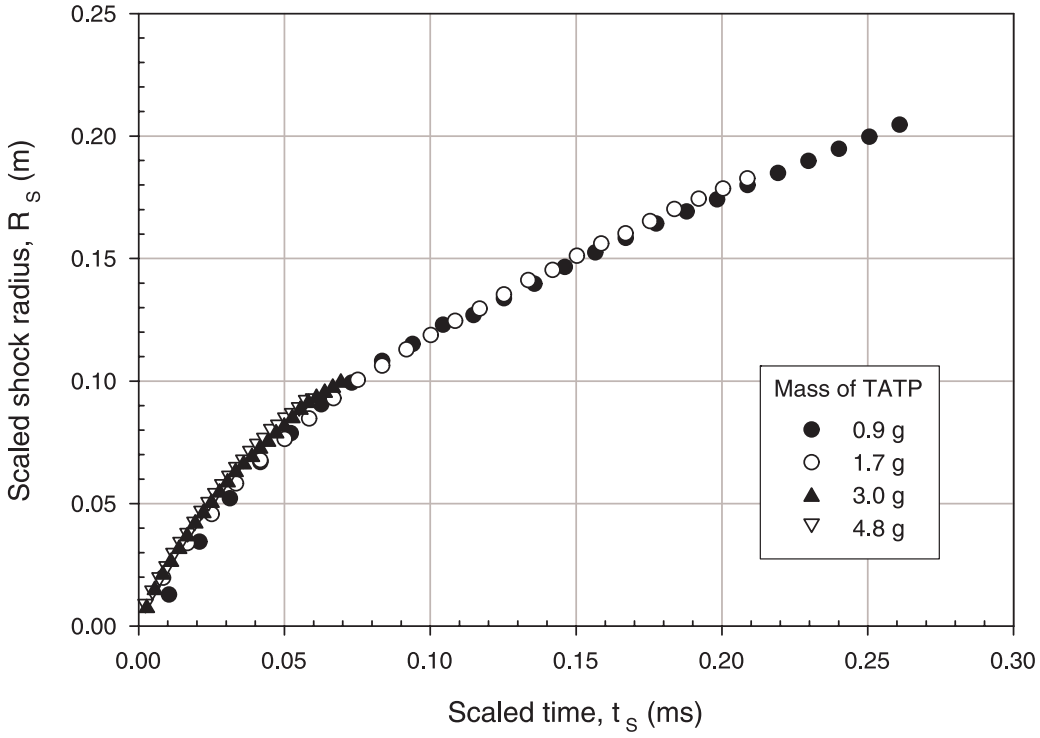

Figure 3.6. Scaled shock radius as a function of scaled time for TATP charges of varying mass, scaled to $1g$

The spread in the experimental data shown in Figures 3.5 and 3.6 is used to estimate the uncertainty in the Mach number versus radius graphs. As seen in these data, the uncertainty in radius is greatest near the center of the charge, which is due to the rapid rate that the shock is moving. At high shock speeds, the measurement is limited by the field of view and available frame rates of the high-speed camera. As the shock wave decays toward a sound wave, the measurement is more easily and exactly made with the frame rates available with the high-speed camera.

3.1.3 Experimental Shock Mach Number versus Radius

Once the shock radius as a function of time is known and is fit to Equation 1.8, the equation can be differentiated to obtain Equation 1.9, resulting in shock velocity as a function of time. These two equations can then be combined to produce the more useful curve of shock Mach number versus radius. This curve is essentially the explosive characterization, since all other useful data can be obtained from it.

Figure 3.7 shows the Mach number versus radius for PETN and TATP as experimentally determined here. The figure also shows TNT, plotted from the standard $1kg$ TNT data [1], scaled to $1g$ for comparison purposes. The range of data shown in Figure 3.7, for radii from about 0.03 to $0.25m$, covers the primary region where data were collected and is the only region where the curve-fit equations are valid with the coefficients given in Table 3.1. This region is also the only one wherein later material deformation experiments were performed.

The measurement uncertainty increases at small radii, as shown by the error bars in Figure 3.7. Typical errors for all measurements with $R_s > 0.10m$ are on the

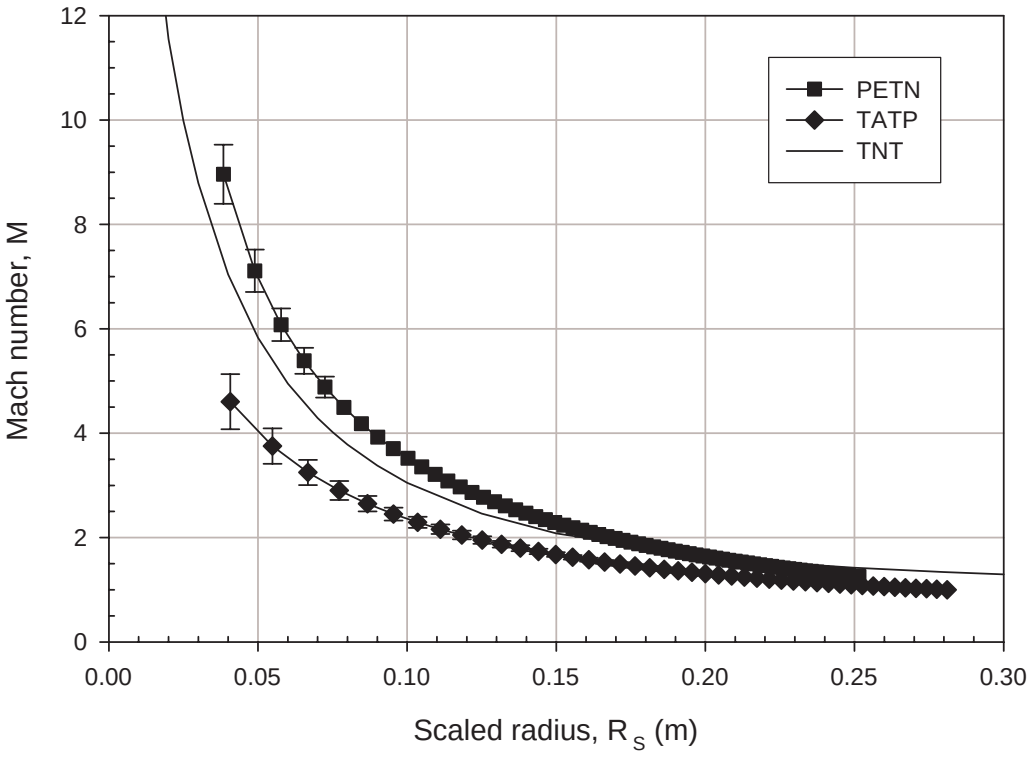

Figure 3.7. Mach number versus radius for $1g$ charges of PETN, TATP, and TNT

order of $\pm 3\%$ of the measured value. The error bars are either shown explicitly or are represented by the size of the data-point symbols. The uncertainty is estimated from the variability between individual experiments and also by the shock tracking program based on the pixel calibration and other information required to perform the measurements. At high shock speeds the high-speed digital camera does not have the time resolution to sufficiently resolve the shock motion accurately. As the shock speed decays toward Mach 1, however, the frame rate capabilities of the camera allow this measurement to be made with high precision. Given a camera capable of recording at rates greater than $250,000 fps$, the uncertainty could be reduced for measurements within $0.05m$ of the charge center.

As seen in Figure 3.7, the shock Mach number for both explosives tested here decays to approximately 1.0 within $0.3m$ radius. This is an important result that reinforces the safety considerations for these gram-scale explosive charges. A shock wave at Mach 1 is a sound wave, traveling at the local speed of sound and with essentially zero pressure change across it. These charges are therefore extremely safe because within $0.3m$ the explosive-driven shock wave has decayed to a loud sound wave. In the laboratory setting, where researchers are sheltered behind barricades several meters away, the shock waves pose no danger and require only simple hearing protection during experiments.

Figure 3.7 also shows each explosive's shock propagation characteristics relative to that of TNT. These curves can be used to infer a qualitative "TNT equivalence" for each of these explosives. As seen for the PETN curve, the experimental data show that the shock propagates faster than that of TNT over the range of radii shown. This faster propagation indicates that PETN has a greater yield than TNT, therefore a TNT

equivalence ratio greater than 1. The degree by which the PETN shock stays ahead of the TNT shock however varies, indicating a variable TNT equivalence as a function of radius. The TATP curve is below the TNT curve for all radii, therefore having a TNT equivalence ratio less than 1. Again the distance between the curves changes with radius, indicating a radial dependence of TNT equivalence.

One method of computing TNT equivalence quantitatively is to find the mass of TNT required to cause the same overpressure at the same radius as a different mass of another explosive charge [7]. The explosive overpressure can be determined from the shock Mach number according to Equation 1.10. Thus the TNT standard shown in Figure 3.7 is scaled by mass until the shock Mach number matches that of the desired explosive curve at each point. This process generates a variable TNT equivalence as a function of radius from the explosion center, as previously shown by Kleine et al. [7]. It is shown here in Figure 3.8 for PETN and TATP. The large error bars on the data reflect the imprecision of scaling the TNT curve to match the experimental explosive cuve. Small uncertainties in Mach number result in large uncertainties in TNT equivalence due to Mach number being raised to the second power to obtain overpressure in Equation 1.10.

Previous TNT equivalence estimates for PETN range from 1.2 to 1.8 grams TNT per gram PETN depending on the type of test used to calculate equivalence [1]. The present research shows that the TNT equivalence actually varies between 0.9 and 1.8 depending on the radius from the explosion center. Similar results showing radially dependent TNT equivalence were published by Kleine et al. for silver azide [7].

One published TNT equivalence value for TATP is 0.88 grams TNT per gram TATP [72]. The present data show a TNT equivalence range from 0.3 to 0.5 grams

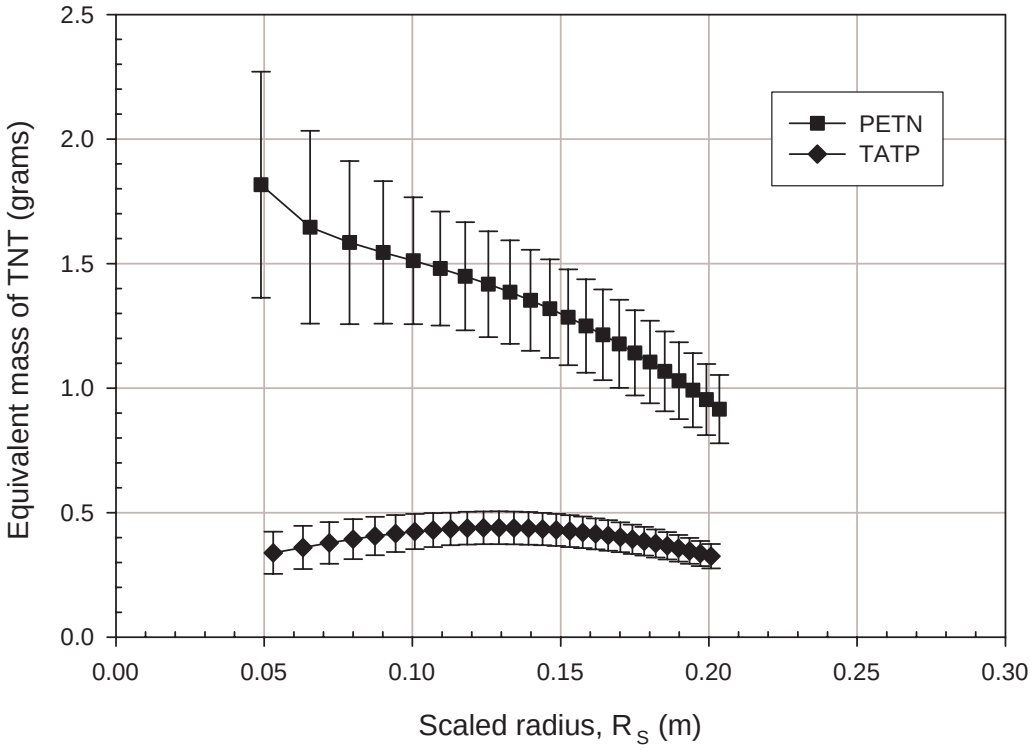

Figure 3.8. Calculated TNT equivalence for PETN and TATP

TNT per gram TATP. The TATP used here, however, included a desensitizing polymer to stabilize the material, reduce volatility, and allow safer handling [58], which could produce a lower TNT equivalence than pure TATP. However, the large discrepancy is more likely due to the different methods used to measure TNT equivalence here and in the work of Kemp [72]. The measurements shown here accurately represent the shock wave strength and the subsequent explosive damage potential. Shock-wave loading as a function of radius determines damage to a structure more accurately than a simple TNT equivalence factor.

These equivalence values based on the standard TNT explosion are expected to be valid over the majority of the shock wave radius range with the exception of its extremes. Both TNT equivalence curves in Figure 3.8 show maximum values between scaled radii of 0.05 and $0.15m$. PETN has a maximum TNT equivalence near the center of the charge, likely due to the higher detonation velocity of PETN relative to TNT. The decrease in equivalence for TATP at small radii is most likely due to significant errors near the explosion center. Limited camera resolution and other factors prevent more accurate measurements in this region as discussed above. The high slope of the TNT Mach number versus radius curve in this inner region region causes small errors in measured Mach number or radius to be magnified when determining TNT equivalence.

The decay of the equivalence curve with increasing radius is likely due to different chemical processes among the explosives considered. TNT is known to have an after-burning effect which changes the way in which the shock propagates relative to an ideal, point-source explosion. Dewey has shown that TNT maintains a larger overpressure than an ideal explosion at large distances [4]. The difference in shock speed, and therefore

TNT equivalence, is thus highly dependent upon the chemical mechanism by which the explosion process occurs. A detailed study of reaction mechanisms would be required to fully explain the TNT equivalence curve shapes of Figure 3.8.

3.1.4 Experimental Overpressure Duration versus Radius

Measurement of shock wave overpressure duration as a function of radius completes the explosive characterization process as defined here. The overpressure duration must be known to complete the definition of explosive impulse, which is the energy delivered to an object in the path of the shock wave. The definition of impulse is integral to the ability to analyze a material response to an explosive input.

Kinney and Graham suggested that the overpressure duration could be calculated upon knowing the speed of the shock wave as a function of radius [1]. This calculation assumes that the point marking the end of the positive pressure pulse, the "end-of-duration point" as shown in Figure 3.9, moves at the speed of sound based on the gas temperature behind the shock wave. This "theoretical" duration can be calculated from the shock Mach number versus radius data by invoking the Rankine-Hugoniot theory [10]. Each point in space is assumed to have a static temperature caused by a shock wave passing at a given Mach number through the ambient air. Simple gas dynamics and a finite difference scheme can be used to propagate the shock front and end-of-duration point through space using the measured Mach number versus radius profile. This numerical scheme, based on the experimental data, is used to produce the theoretical overpressure duration versus radius profiles for PETN and TATP as shown in Figure 3.10. The curves plotted are valid only in the regions where PETN and TATP

Mach number versus radius data are valid. As calculated, the curves appear to not originate exactly at the origin, but this is expected to be purely a numerical and non-physical result and is discussed further in Section 3.1.6.

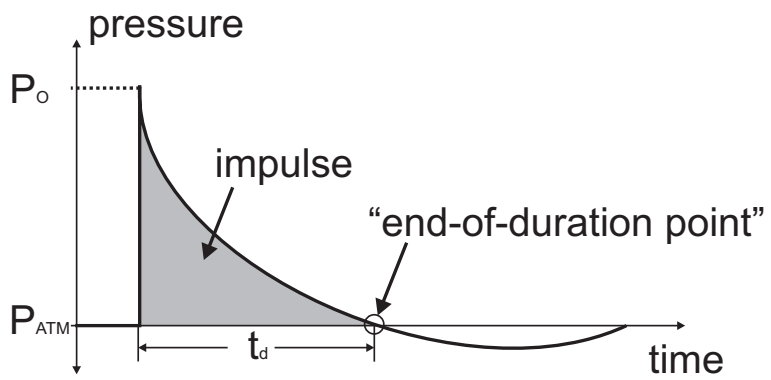

Figure 3.9. Pressure-time history of an ideal, explosively driven shock wave showing the "end-of-duration point"

The overpressure duration for PETN was measured experimentally and is also shown in Figure 3.10. Table 3.2 gives details for the experimental measurements for the case of PETN. Each test was conducted according to the procedure described in Section 2.2.4. The data plotted in Figure 3.10 are scaled to reflect the actual charge mass scaled to a $1g$ charge. The scaling procedure as discussed in Section 1.2.1 affects both the time and distance scales. Experiments in which the pressure gage was struck by a fragment or where the gage failed to trigger are not included in Table 3.2.

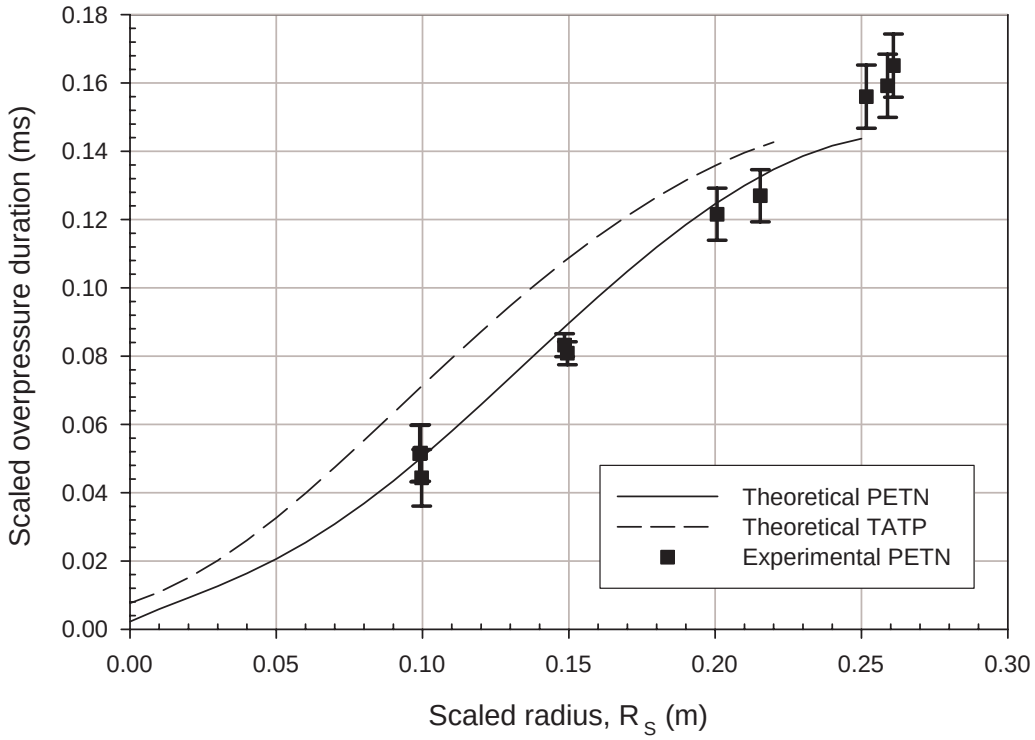

Figure 3.10. Theoretical and experimental overpressure duration for PETN and TATP

Table 3.2.
Experimental overpressure duration measurements and scaled values for PETN charges

Test	**Mass**	**Gage**	**Radius**	**Duration**	**Scaled radius**	**Scaled duration**
	(g)		(m)	(ms)	(m)	(ms)
1	0.80	1	0.20	0.118	0.215	0.127
2	0.90	1	0.25	0.154	0.259	0.159
3	0.88	1	0.25	0.158	0.261	0.165
4	1.03	1	0.15	0.084	0.149	0.083
4	1.03	2	0.10	0.052	0.099	0.051
5	1.02	1	0.10	0.052	0.099	0.052
6	0.99	1	0.10	0.045	0.100	0.045
6	0.99	2	0.15	0.081	0.151	0.081
7	1.01	1	0.20	0.121	0.199	0.121
8	0.98	1	0.25	0.155	0.252	0.156

The error bars plotted on Figure 3.10 reflect twice the standard deviation of the measurements at the nominal radii of 0.10, 0.15, 0.20, and $0.25m$. This error bar represents approximately $\pm 5\%$ of the measurement and is representative of the uncertainties inherent in the duration measurement. To decrease the error, the method of determining overpressure duration from a pressure trace cited by Kinney and Graham was used [1]. This method allows the error to be mitigated by examining the broad exponential decay trend in the pressure data. Although the pressure gage measurements are noisy, as previously shown in Figure 2.7, all measurements show good repeatability.

The experimental error varies inversely with radius, similar to all other measurements presented here. The error at small radii is likely due to irregularities at the shock front. The experimental error is also large there because the noise in the pressure gage signal becomes more significant relative to the actual duration measurement. At radii greater than $0.25m$ the theoretical overpressure duration curve is not plotted because this region is outside of the measured range of radii for the PETN charges. The data points at the edge of this region show that the duration continues to increase, even though the theoretical curve appears to level off.

No data was obtained for radii less than $0.10m$ because the pressure increase here was greater than the maximum rating for the pressure gages used. The shock front is also expected to be irregular in this region due to local instabilities, which will complicate the measurement accuracy. Future work should collect data in this region using more robust pressure gages.

No duration data were obtained for TATP because explosive charges were not available for these experiments.

The present experimental pressure duration measurements support the theoretical duration calculation hypothesis of Kinney and Graham to within experimental error, as shown in Figure 3.10. Prior to the present study, no experimental data have been presented to confirm or disprove this hypothesis. Thus, more experiments should be performed to further confirm this theoretical approach, especially in the limit of small radii. The present experimental and theoretical match, however, shows the value of knowing the shock Mach number versus radius profile for an explosive, since it also determines the overpressure duration.

3.1.5 Experimental Explosive Impulse versus Radius

As stated in Section 2.3.1, the explosive impulse for the material deformation experiments is approximated as a triangular function. This assumption, involving a linear pressure decay from maximum overpressure to atmospheric pressure, is a simplification frequently used to avoid details of the pressure distribution immediately behind the shock wave [1]. The assumption typically over-estimates the explosive impulse.

Explosive impulse varies with both charge mass and radius from the explosion origin. Figure 3.11 shows the triangular impulse variation for $1g$ PETN and TATP charges, as determined from the experimental data presented here. The figure shows an inverse relationship between explosive impulse and distance from the explosive charge. Again, the graph shows that, within $0.3m$ of the explosion, the strength of the blast has decayed to approximately zero and therefore poses no safety risk for researchers.

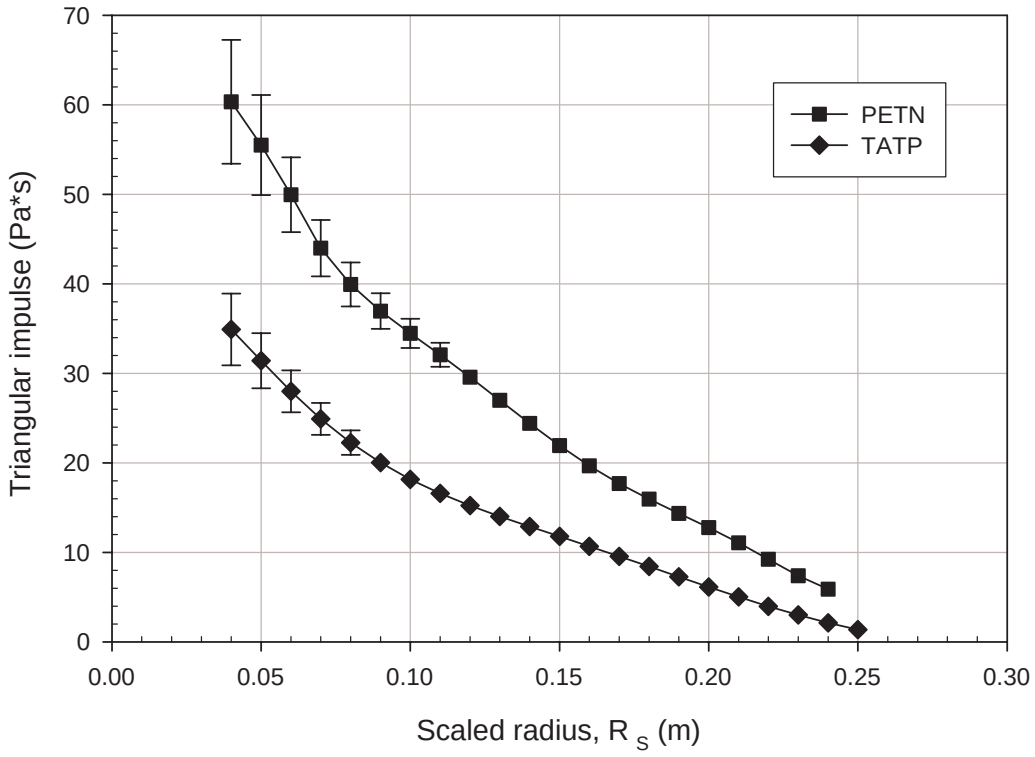

Figure 3.11. Experimentally determined triangular explosive impulse versus radius for $1g$ PETN and TATP charges

Significant error exists in the determination of the explosive impulse for radii less than about $0.07m$. This error reflects the uncertainty in shock Mach number and overpressure duration for this same range of radii. By improving the shock Mach number and overpressure duration measurements through more experimentation and higher camera resolution, the error in impulse will decrease.

The triangular impulse in Figure 3.11 uses the incident shock wave overpressure defined by Equation 1.10 as the maximum pressure. If the reflected-shock overpressure is used instead, the impulse increases by as much as an order of magnitude. The incident and reflected overpressures are both functions of the incident Mach number [1], further showing the importance of the Mach number versus radius relationship. The reflected-shock overpressure, P_{ref}, can easily be determined from Equation 3.1, but is not used here. The final form the equation has been simplified for $\gamma = 1.4$.

$$\frac{P_{ref}}{P_{atm}} = \frac{[(3\gamma-1)M^2 - 2(\gamma-1)][2\gamma M^2 - (\gamma-1)]}{(\gamma^2-1)M^2 + 2(\gamma+1)} = \frac{(4M^2-1)(7M^2-1)}{3(M^2+5)} \tag{3.1}$$

Both the incident and reflected overpressure are used in the material deformation scaling, presented later in Section 3.2.4. Both overpressure values can be easily determined with a known Mach number versus radius profile.

3.1.6 Computational Explosion Modeling

Computational modeling with the commercial software AUTODYN were used to compare with and to validate the gram-scale explosion measurements. The computational domain, described in Section 2.2.5, was first used to solve a standard TNT explosion, then to solve a similar PETN explosion.

Each simulation, of a $1kg$ explosive charge, was run until the primary shock wave had propagated approximately $3m$ from the charge center. Simulated pressure gage output was generated at 29 locations, documenting the pressure-time history beginning at charge initiation. These data were used to determine the shock wave time of arrival and the overpressure duration at each location. The time of arrival was determined by finding the maximum pressure at each gage location, and designating this time as the shock arrival time for that location. The maximum calculated pressure was also recorded in order to infer a shock Mach number based on Equation 1.10. When the recorded pressure decreased below atmospheric pressure, the arrival of the "end-of-duration point", the time was again recorded. The difference between the time of shock arrival and end-of-duration point arrival is the overpressure duration. The pressure gages locations were thus analyzed computationally to determine all information previously measured in experiments.

The TNT simulation was of a $1kg$ charge exploded in a standard atmosphere. This simulation was used to validate the computer model by comparison with the standard TNT data as published by Kinney and Graham [1]. The scaled shock wave radius versus scaled time results are shown in Figure 3.12. The computational result and standard

data for TNT are an almost identical match for scaled time up to about $2ms$. After this point the TNT standard data shows the shock propagating at a slightly faster rate, although the discrepancy is negligible. This close match shows that the AUTODYN computational domain and approach are valid and can be applied to PETN.

The experimental radius versus time for TNT shows that the shock radius does not actually begin at the origin. The standard TNT data and the computational TNT simulation both show that the shock appears to originate from the radius of the explosive charge at $t = 0$. This result can be interpreted by considering that the shock propagates through the solid material of the explosive charge several times faster than is possible through the ambient air. The shock propagation through the solid explosive is also being driven by the detonation reaction. This reaction does not extend into the air, therefore further slowing the shock propagation in air compared to the solid explosive. The shock can thus be assumed to originate from the solid explosive radius when considering the time-scales of shock propagation through air as the primary result.

This boundary condition helps to fix the experimental PETN data along the time axis. As originally stated in Section 3.1.2, the experimental data set for shock position versus time contains a large uncertainty when determining the absolute time of charge initiation. The final data, as assembled with no constraint upon radius when $t = 0$, can now be shifted along the time axis so that the radius at $t = 0$ is equal to the charge radius. This shift along the time axis does not change the shape of the radius-versus-time curve and does not alter the measured data, it is done only to accommodate the charge initiation which occurs between frames in the experimental data. After this shift is performed, the data are then re-fit to Equation 1.8 and the coefficients thus determined

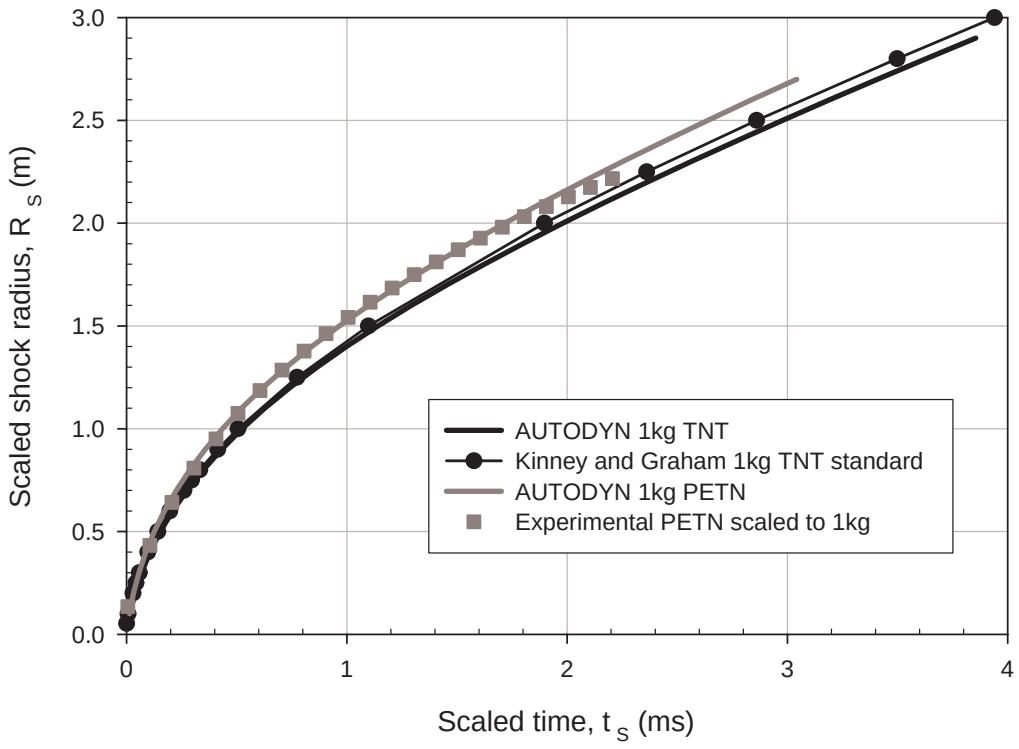

Figure 3.12. Shock wave radius versus time for TNT and PETN

are given in Table 3.1. The curve-fit is again used for purposes of manipulating the data without having to deal with individual data points.

In order to match the simulation conditions of the TNT computations, a $1kg$ PETN charge was used for the computational simulation of the experimental data. The simulation of a $1kg$ charge is within the typical range of application of the JWL equation of state for PETN and most explosive events. The results from this simulation therefore accurately reflect the large-scale PETN results and provide an opportunity to validate the small-scale results and scaling approach. The experimental radius versus time data for PETN measured here for a $1g$ charge were scaled to represent a $1kg$ charge. This results in $S = 0.1$, from Equation 1.6, which leads to a factor of 10 difference in both time and radius. The scaled experimental data and computational data are shown in Figure 3.12.

The experimental PETN data match the computational prediction almost exactly. The two results begin to diverge at a radius of approximately $2.0m$, which through the scaling, corresponds to a radius of $0.20m$ in the experiments. The radius of $0.20m$ is at the edge of experimental measurements, thus some deviation at this extreme is not unexpected.

From the computational prediction, the maximum pressure at each pressure gage location was determined. These data, when used with Equation 1.10, yielded a shock Mach number corresponding to that radius from the charge center. Figure 3.13 shows the computational and experimental Mach number profiles versus radius for PETN. Again the experimental data are scaled from a $1g$ charge to a $1kg$ charge in order to match the simulation and demonstrate the scalability of the data.

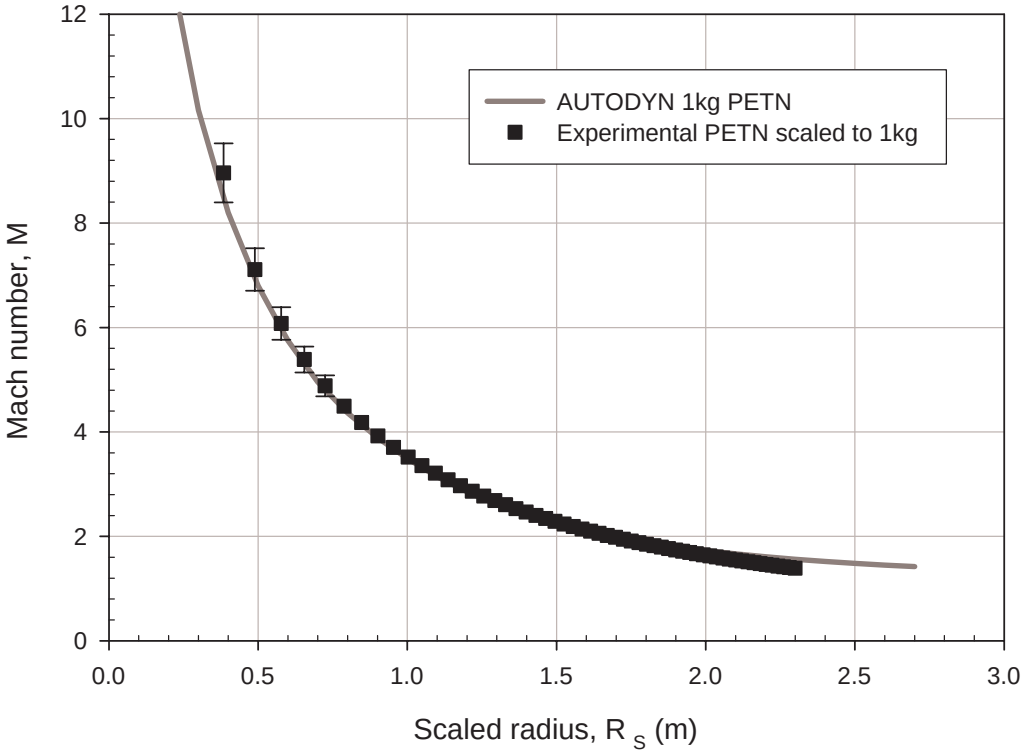

Figure 3.13. Shock Mach number versus radius for $1kg$ PETN charges

The scaled experimental data agree well with the computational results in Figure 3.13. The data, however, diverge at the small and large radius extremes. For small radii the divergence is still within the error bar of the experimental data, but is also at the edge of the measurement region due to the high-speed digital camera time resolution. The discrepancy at large radius is the same as seen in Figure 3.12, due to limited data at radii larger than $0.20m$. Again the scaling from $1g$ to $1kg$ results in a factor of 10 difference in radius. The scaling, however, does not affect the Mach number since that is already non-dimensional and the ambient air temperature was the same in the experiments and simulations.

The computational results for the shock motion show that the simulation closely matches the experimental data, especially for the region of interest where shock Mach number, M, is $1.5 \leq M < 7$. This is the region of interest because the shock Mach number is large enough to produce a significant overpressure but low enough to avoid gross violation of the ideal gas assumption for air [10].

Although the shock propagation data match, the pressure behavior after the shock do not agree among Kinney and Graham's theoretical approach, present experimental data, and computational simulation. Computed pressure traces, useful to measure the overpressure duration, were obtained from the AUTODYN simulations of TNT and PETN explosions. The computational pressure data is shown in Figure 3.14. Also shown in this figure are the standard TNT overpressure duration [1], the theoretical PETN result from Kinney and Graham, and the experimental PETN measurements. These PETN data are the same data presented in Figure 3.10, only scaled from a $1g$ to a $1kg$ charge.

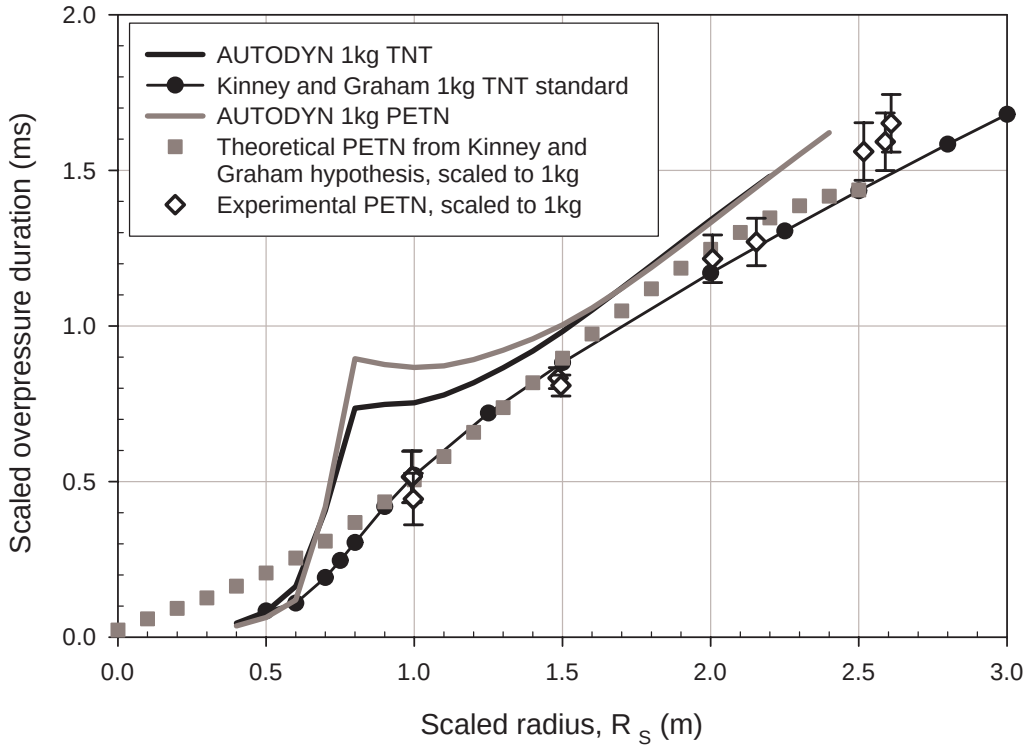

Figure 3.14. Overpressure duration versus radius for $1kg$ TNT and PETN charges

First consider in Figure 3.14 the region where $R_s \leq 0.7m$. This area shows somewhat different behavior between the theoretical PETN and the combined group of the TNT standard and the AUTODYN simulations. The simulations and standard TNT data appear to originate from a point of finite radius. This radius is difficult to estimate from the simulation because data for $R_s \leq 0.4m$ becomes non-physical and therefore is not plotted or used. The theoretical estimation from the PETN data, on the other hand, originates approximately from the graph origin. This result, however, conflicts with the previous observation that the shock wave essentially originates at the radius of the charge. These data were analyzed repeatedly through various calculation methods for the theoretical duration profile. Each calculation method resulted in the same shape and values of the predicted overpressure versus radius, thus the original and simplest method is chosen here, as previously discussed in Section 3.1.4. Future work will be required to analyze and reconcile the small-radius data in Figure 3.14.

Another region of interest of Figure 3.14 is for $0.7m \leq R_s \leq 1.3m$. The overpressure duration profile predicted by AUTODYN in this region contains an unusual and seemingly non-physical shape. The duration rises quickly from the value at $R_s \approx 0.6m$ to a maximum value. The immediate decrease after this maximum produces an unlikely curvature discontinuity in the graph. This discontinuity in the evolution of a physical property is unlikely because no shock wave or other compressible-flow phenomenon is occurring in that region of space and time. To learn more about this region, a wave diagram showing the location of important explosion features in time and space was created.

Figure 3.15 shows the relative positions of the shock front, contact surface, and end of overpressure duration for a $1kg$ TNT charge, as calculated using AUTODYN. The figure also shows the end of the positive duration for the standard $1kg$ TNT explosion [1]. The time of arrival of the shock and of the overpressure duration ending at each pressure gage location was determined as described above. The positive overpressure duration can be measured from this graph as the time interval between the shock-front and the end-of-duration curves at a given radius. The difference between the computed and "standard" durations can be seen as the difference in arrival time of the end of duration at each radius.

The contact surface propagation in Figure 3.15 is driven by the shock motion and the expansion of the product gases as calculated by the AUTODYN Eulerian solver. The contact surface was defined as the foremost point within the computational domain into which TNT explosive product species propagated at each time step. The location of the contact surface was determined by hand from a sequence of AUTODYN image outputs at each time step of the simulation. By tracking the contact surface, the effects of the hot combustion gases on the pressure gage readings can be analyzed.

Although difficult to see in the figure, the first two data points for the AUTODYN end-of-duration, at radii of 0.4 and $0.5m$, are the same as the TNT standard at the same radii. Thus the overpressure duration for these radii are the same, as shown in Figure 3.14. From this point, the standard TNT end-of-duration appears to follow the contact surface until the contact surface begins to contract, at which point the standard TNT end-of-duration continues to propagate outward almost linearly. The computational end-of-duration, however, falls behind the contact surface and propagates at a slower

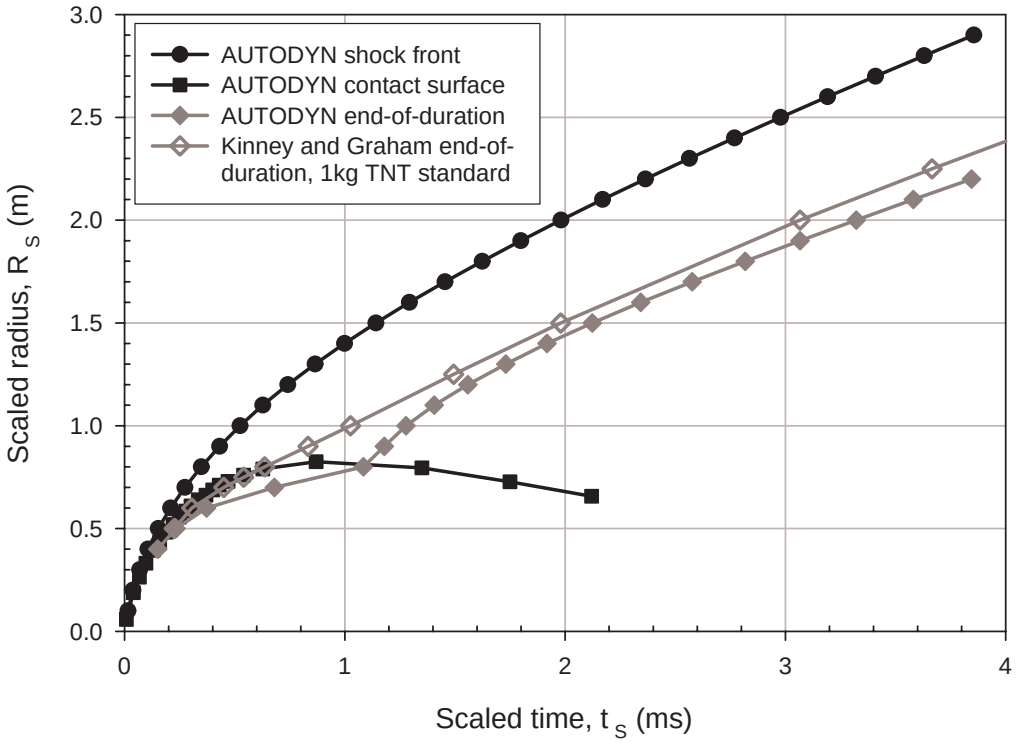

Figure 3.15. Wave diagram for a $1kg$ TNT charge explosion

rate. This end-of-duration point appears to propagate slower because it takes longer for the hot combustion gases to return to atmospheric pressure, the condition defining the location of the end of duration.

Once the contact surface begins to contract, the computational end-of-duration point emerges from within the TNT combustion gases. At the point of emergence, the end-of-duration point immediately accelerates, producing the non-physical AUTODYN result curvature discontinuity shown in Figure 3.14 at $R_S \approx 0.8m$ and discussed above. The end-of-duration point, however, quickly decelerates and eventually propagates approximately linearly and parallel to the trend of the standard TNT data.

This wave diagram shows the important role that the contact surface plays in the computational simulations. If the contact surface is actually present in this region and affecting the overpressure as computed by AUTODYN, then it must be accounted for or a different definition of explosive overpressure must be developed for this region. The experimental pressure measurements, however, as shown in Figure 3.14, suggest that this computed pressure behavior may be non-physical.

This anomalous region also appears to affect the far-field overpressure duration calculation. For $R_s \geq 0.15m$ in Figure 3.14 the AUTODYN computed duration increases linearly and approximately parallel to the experimental duration increase. The matching slopes imply that the computed propagation rate for the region is appropriate, but the initial condition for the AUTODYN case is incorrect.

The present research does not experimentally document the propagation of the contact surface. Future research should address these issues of overpressure measurement and prediction in the near-charge region. For the application to material blast research

in the present study, however, the overpressure duration is henceforth assumed to follow the theoretical curve developed from Kinney and Graham, which is also supported by the present experimental measurements.

3.2 Gram-Scale Material Blast Results

Thin aluminum plates are deformed by the explosion of previously-characterized gram-scale explosive charges. The deformation process is recorded to reveal the dynamic, three-dimensional plate deformation throughout the explosive event. The measurements made here show that the dynamic deformation scales according to the applied explosive impulse. These laboratory experiments demonstrate a range of potential applications and the benefits of performing small-scale experiments instead of the typical full-scale outdoor tests. The present research develops the basic apparatus and procedure for these experiments and presents results that can be further developed and explored to improve current material models.

3.2.1 Symmetry of Material Deformation

At high frame rates, the high-speed digital camera pixel resolution is insufficient to measure the entire plate surface motion at one time. Thus, only a fraction of the plate surface is measured in order to obtain the required frame rate and spatial resolution to fully capture the plate motion. For the present research, the horizontal diameter of the exposed plate surface is centered within the field of view and approximately $0.03m$ of the plate surface above and below this region is imaged. This strip-wise view conforms to the Photron APX-RS camera's field-of-view capabilities at high frame rates. Before limiting

the field-of-view to this region, experiments were performed to measure the degree of symmetry of the material deformation.

To measure the deformation symmetry, experiments were performed in which the cameras imaged the entire exposed plate surface and recorded its motion at $10000fps$. At this frame rate, the pixel resolution is $512x512$, providing the same horizontal resolution as the frame rate used for the primary measurements. At $36000fps$, the primary measurement frame rate, the frame resolution is $512x128$, providing the maximum spatial and temporal resolution balance possible for imaging an entire diameter of the plate in the test fixture. Figure 3.16 shows the entire plate surface and the approximate area imaged at the higher measurement frame rate.

A test was performed to measure the plate deformation symmetry at the time of maximum dynamic deformation and at the final plastic-deformation state. Figure 3.17 shows out-of-plane deformation contours at the time of maximum deformation. Also shown in the figure are four diameters, numbered $1-4$ which are used to measure the symmetry of deformation. The deformation recorded here is not used as final data because this frame rate does not capture the actual maximum deformation adequately for this explosive impulse. Figure 3.18 shows the deformation recorded along each of the 4 diameters selected for analysis. As shown in Figures 3.17 and 3.18, the plate deformation during an experiment is highly radially-symmetric. The central region of the plate deforms, showing nearly concentric contours.

Figure 3.17 also shows minor regions where the Correlated Solutions software was unable to perform a correlation. These locations can be seen in the bottom left corner where the contours are not plotted, and instead the speckled plate surface can be seen.

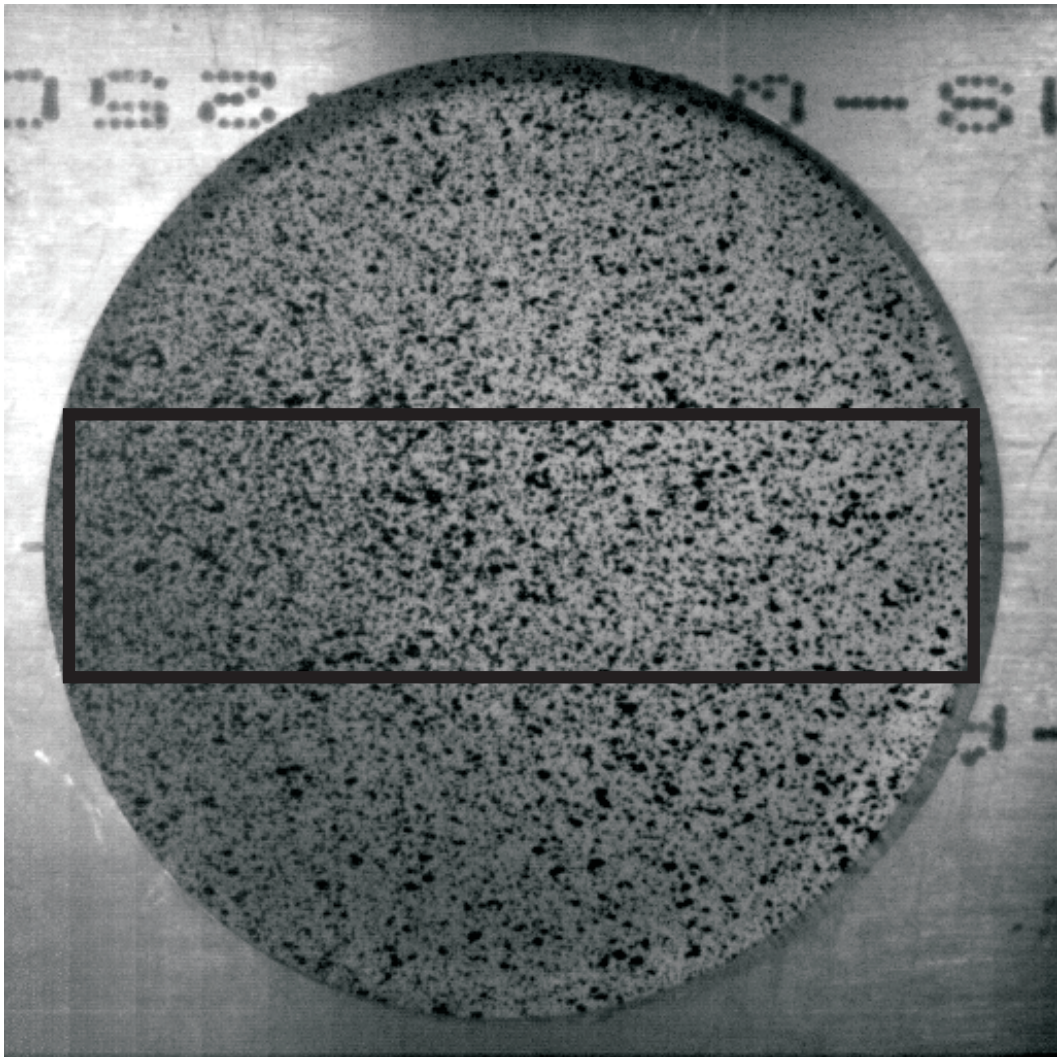

Figure 3.16. Image of the exposed area of a speckle-painted witness plate in the shock-hole fixture, with the approximate measurement region boxed

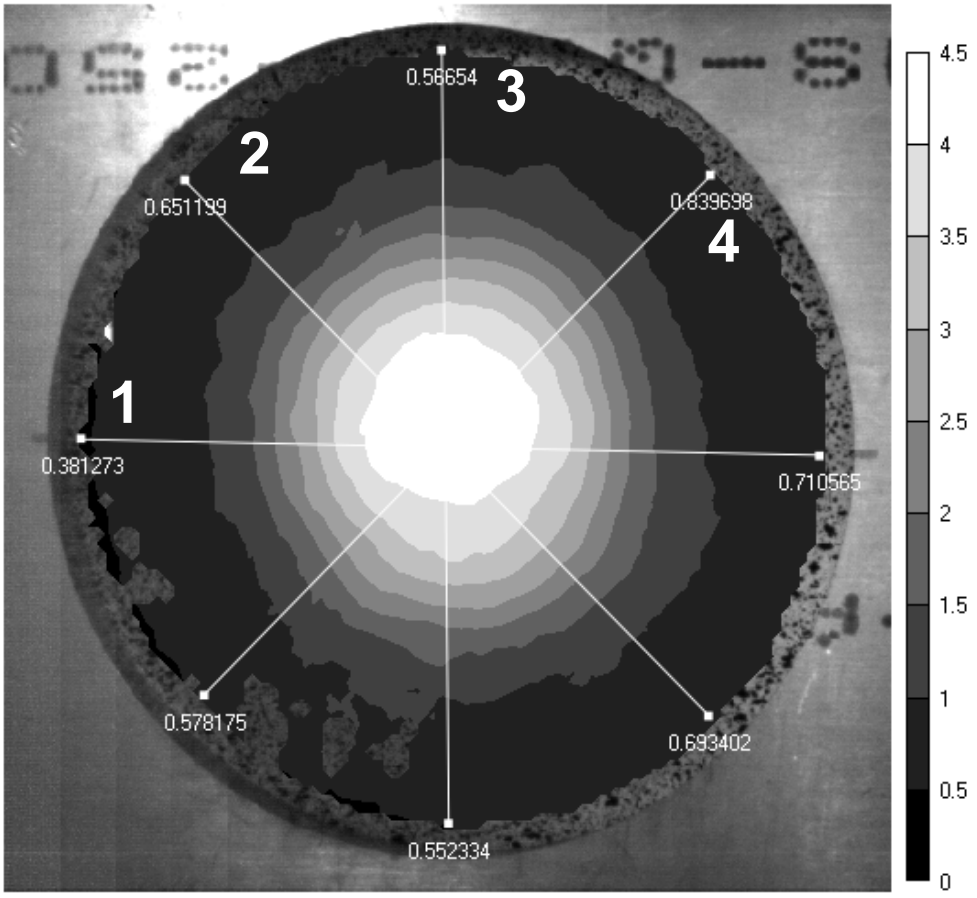

Figure 3.17. Out-of-plane deformation contours in mm, showing deformation symmetry and locations of the 4 diameters analyzed at time of maximum deformation

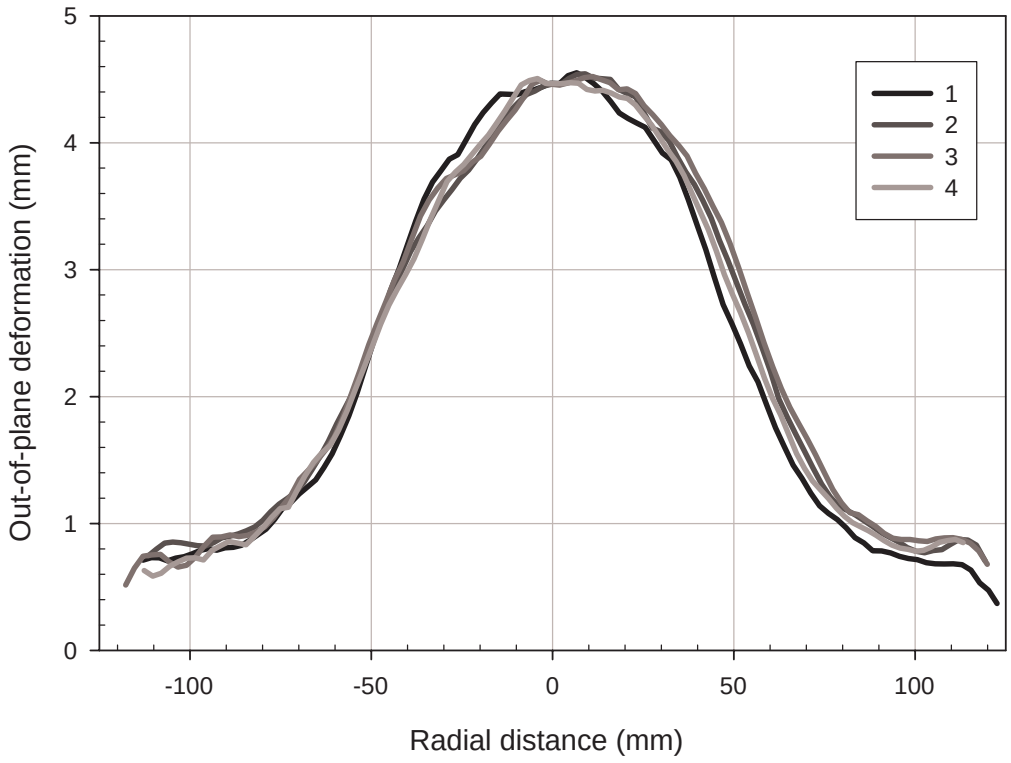

Figure 3.18. Deformation measurements along plate diameters showing high degree of symmetry at time of maximum deformation

During an experiment, such errors can occur when the plate surface loses paint due to the deformation or is over- or under-exposed. These regions are minimized by ensuring that the paint is applied evenly and smoothly and that the plate is uniformly illuminated at all times. When an explosive charge produces a large number of fragments, these fragments can dimple or puncture the thin aluminum plate and cause local paint loss. Un-encased, fragment-free explosives are therefore a requirement in order to accurately conduct these experiments. Each experimental data set is analyzed immediately to determine whether the required measurements can be made. If the area of interest is adversely affected and no correlation is possible, then the data set is rejected.

Figure 3.18 shows that the deformation measurements extracted from the high-speed video are independent of which diameter is analyzed. All 4 diameters show the same shape and maximum deformation. Small differences occur in location, but all slopes and trends are matched among the various diameters.

The final plastic deformation of the plate is shown in Figure 3.19. This figure presents a contour plot with the same four diameters highlighted as in Figure 3.17. The contours again form nearly-concentric circles around the maximum deformation point, which is at the center of the plate. The deformation profiles along each diameter are plotted in Figure 3.20.

The deformation profiles and values shown in Figure 3.20 are similar among all diameters within the estimated experimental error, as discussed in Section 3.2.2. The agreement among diameter measurements for both dynamic and permanent deformation supports the decision to measure only a fraction of the plate surface. The horizontal

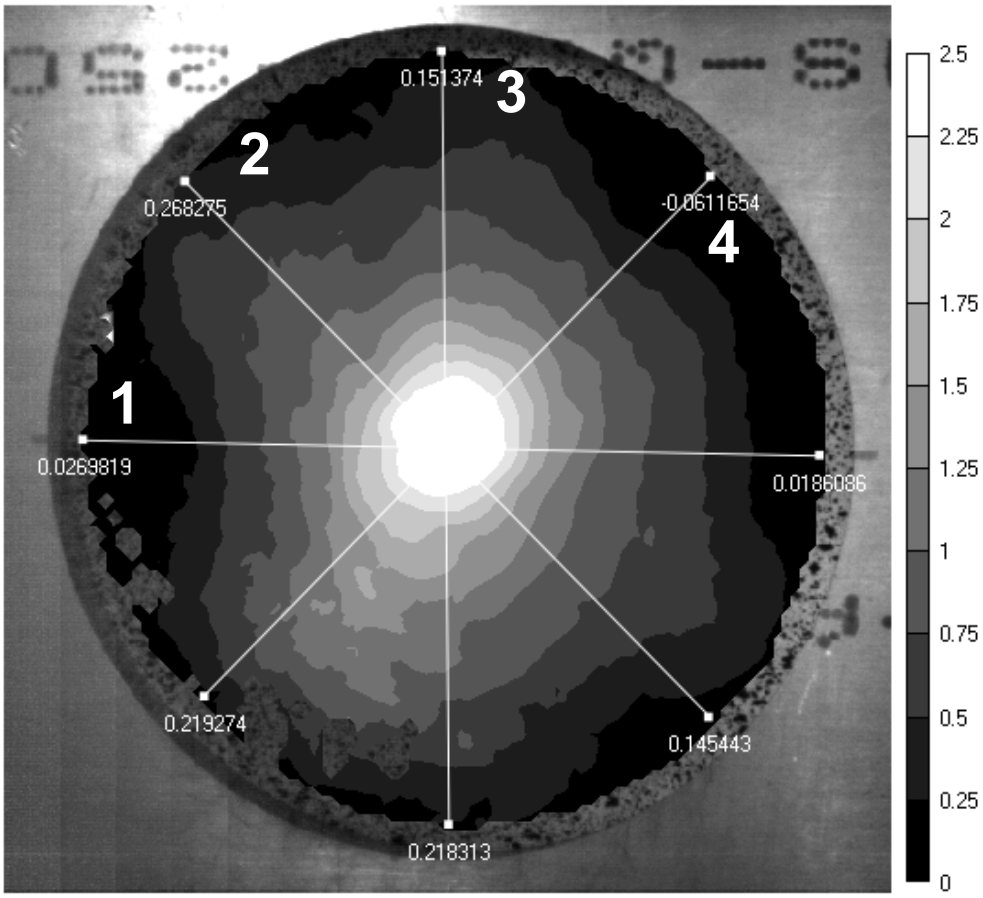

Figure 3.19. Out of plane deformation contours in mm, showing deformation symmetry and locations of the 4 diameters used to measure final plate shape after all motion has stopped

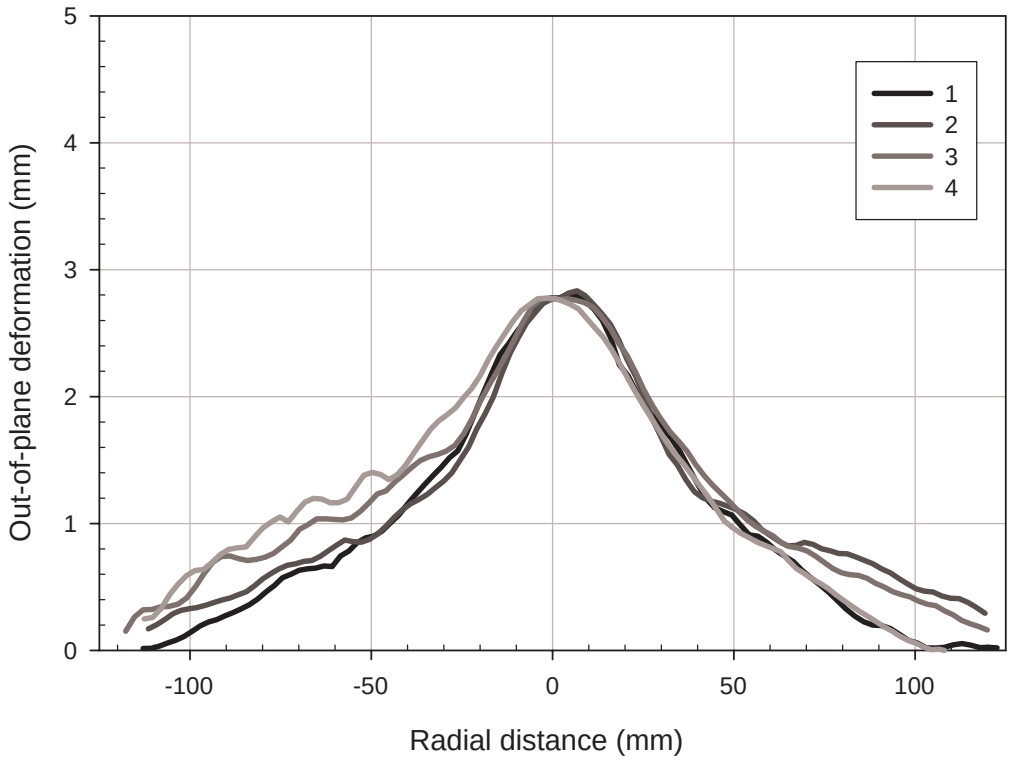

Figure 3.20. Deformation measurements along plate diameters showing high degree of symmetry for the final plate shape after all motion has stopped

diameter of the exposed plate area is therefore imaged in all subsequent experiments and symmetry is assumed.

Although radial symmetry is assumed, the entire plate diameter is nonetheless measured. It was found that the point of maximum deformation does not always occur perfectly centered on the plate, as seen in Figures 3.18 and 3.20. These small variations occur if the explosive charges are not perfectly positioned. If only a radius of the plate is measured, this small variability can cause data reduction to be more problematic, and can potentially lose information about the deformation process. Also, by recording an entire diameter, the center of the plate can easily be located using fiducial marks on the plate fixture.

It was subsequently determined that small variations in maximum deformation location do not affect the magnitude of the deflection or the final plate shape. This variability was found to be within the variation of explosive impulse and deformation measurement accuracy.

3.2.2 Experimental Error Estimation

The experimental error of the plate deformation measurements is divided into the error in computed plate deformation profile and the error due to fixture motion during an experiment.

The Correlated Solutions software claims sub-pixel spatial resolution for deformation measurements [70]. The error associated with these calculations is therefore a function of both the physical area imaged and the camera pixel resolution used. The ratio of pixel resolution to physical length is the same in the symmetry measurements as it is

for the high-speed data collection. The experimental error determined in the symmetry measurements can therefore be directly applied to the high-speed experiments.

To estimate this error, the plate surface profile was measured before the experiment, using the same techniques as used in the symmetry measurements. Figure 3.21 shows the pre-test witness-plate surface with contours of out-of-plane deformation. The out-of-plane deformation is the comparison of one image set to the reference image pair. This comparison to a reference image pair is how all deformation magnitudes are calculated. The error in comparing the flat plate surface from one image pair to the flat plate surface in the reference images therefore estimates the average error associated with any deformation measurement. The resulting calculated deformation profiles along the four diameters are given in Figure 3.22.

The contours and profiles in Figures 3.21 and 3.22 respectively, show that the calculated deformation is approximately random "noise" across the witness-plate surface. From the profiles in Figure 3.22, the experimental correlation error can be estimated as uniform and approximately equal to $\pm 0.05mm$.

The lower left hand corner in Figure 3.21 shows slightly more noise along with regions where the correlation algorithm failed as mentioned earlier. This is reflected in Figure 3.22 in the areas where the noise is somewhat larger. These figures reinforce the importance of ensuring that the pre-test plate surface is properly painted and illuminated. In regions where the correlation algorithm does not have sufficient contrast, the correlation can either fail or result in a large local experimental error. This is important for all experiments, but especially for those where paint may flake off and degrade

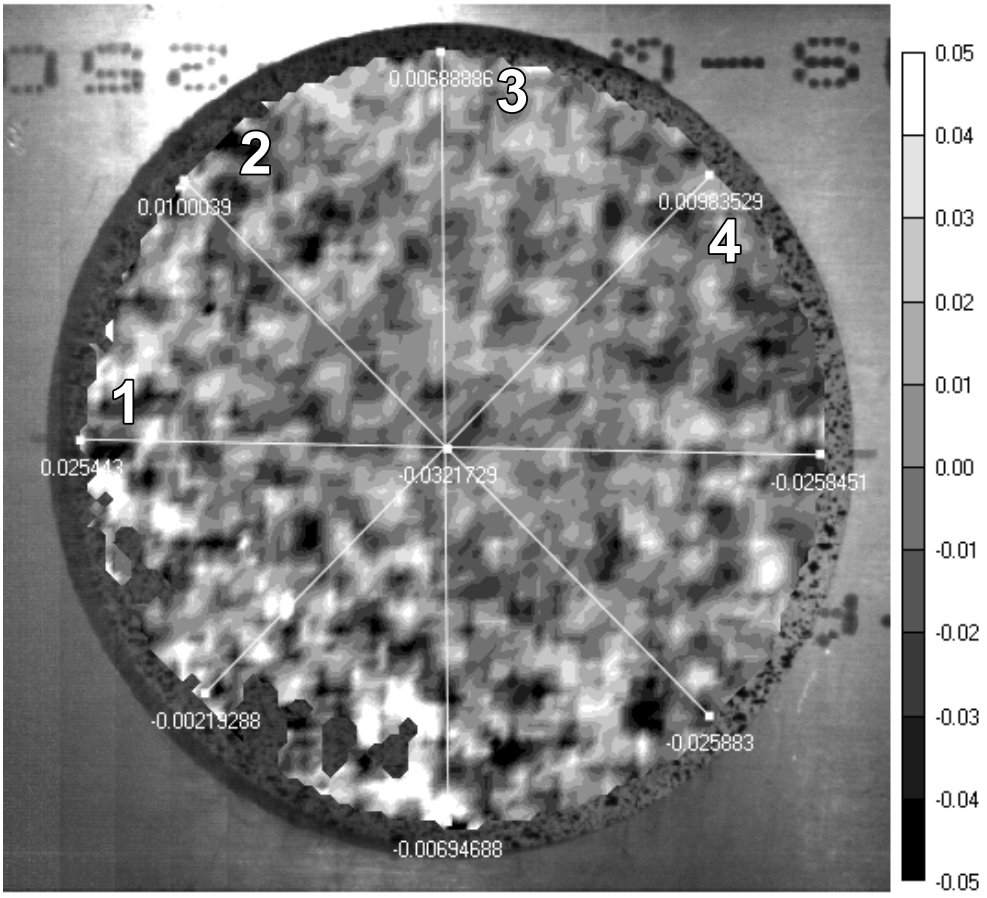

Figure 3.21. Out-of-plane deformation contours in *mm*, showing the small calculated error in determining the flat surface shape of a pre-test aluminum witness plate

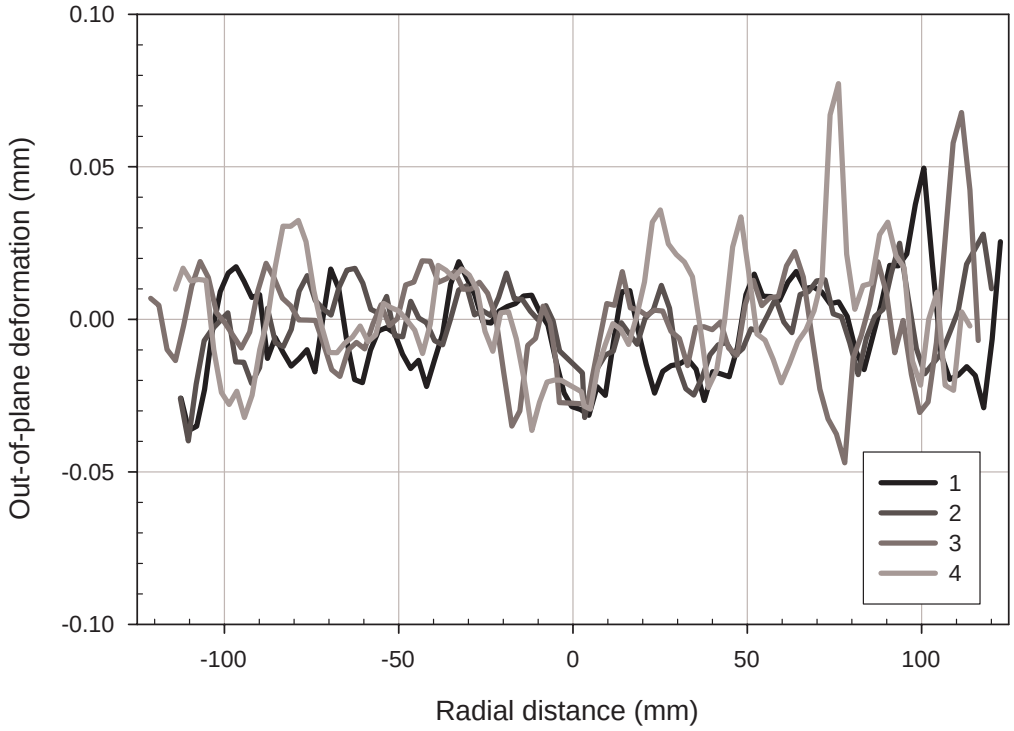

Figure 3.22. Deformation measurements along pre-test plate diameters, showing random "noise" variation in determining flat surface shape

the correlation in one region. All experimental data are therefore carefully examined to ensure that the local correlations, and thus experimental error, are within normal limits.

Motion of the "shock-hole" mounting fixture is inevitable during these explosive impulse experiments. Experimental data from the symmetry experiments were used to estimate this fixture motion and the resulting additional error in plate deformation measurement. Figure 3.23 shows the out-of-plane motion for four sample points on the plate mounting fixture. These four points, selected from a larger data set including two different experiments, show the maximum and the average motion of the fixture. The deformation is over the first $1ms$ of the experiment, sampled at $10,000fps$, and the last data point is the final fixture position.

The data in Figure 3.23 show random motion of the fixture and no coherent oscillation. The motion, however, has a slightly larger error than the measurement of the flat witness-plate surface. The present measurement varies approximately $\pm 0.05mm$ from the assumption of a stationary fixture. The data at $1ms$, showing the final fixture position, are within the $\pm 0.05mm$ for static measurements, indicating that the fixture does not have any translational motion during the event.

Through superposition, the total experimental error in all plate surface measurements is determined to be $\pm 0.10mm$. This error applies to both static and dynamic deformation measurements for all impulse conditions.

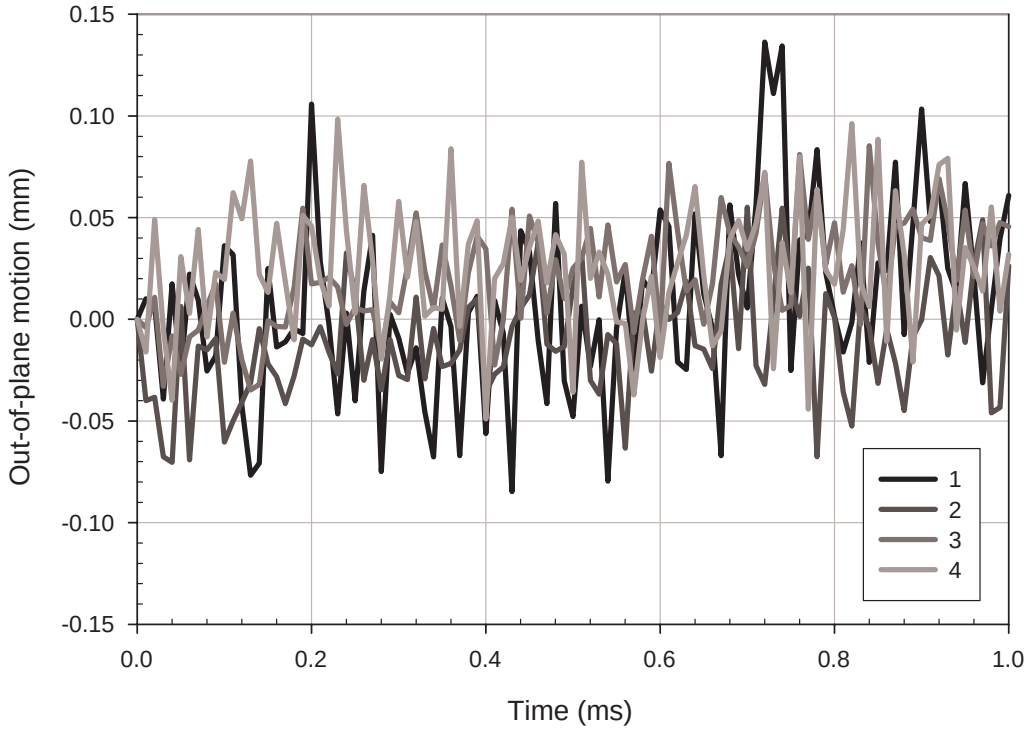

Figure 3.23. Plate mounting fixture out-of-plane motion versus time during symmetry experiments, measured at 4 selected points

3.2.3 Qualitative Description of Material Response

The witness-plate material response to the explosive blast is primarily dependent on the applied explosive impulse and the boundary conditions applied by the "shock-hole" plate mounting fixture. The explosive impulse, as determined by the explosive characterization procedure, determines the amount of energy delivered to the material for a given explosive charge material, mass, and location. Fixture boundary conditions influence the dynamic plate motion and the ultimate plate shape, and thus cannot be neglected in these experiments.

For a given experiment, the explosive charge is massed and positioned at a known stand-off distance from the center of the plate. The explosive charge mass and stand-off distance are scaled to a $1g$ charge to determine the explosive impulse from the experimental data and Figure 3.11. The explosive impulse associated with each plate response is the maximum impulse to the plate, which occurs at the plate center. The impulse decays along the radial direction of the plate surface, but the nature of this decay is not extensively considered in the present work.

Qualitatively, the plate surface motion is initiated by the midpoint acceleration, at the point of first shock incidence and maximum impulse. This motion drives the plate shape for approximately the first $500\mu s$ of the event. Then a deformation wave, reflected from the circular shock-hole fixture boundary, dominates the plate motion and ultimately determines the final plate shape. To analyze the initial plate motion, five physical locations on the plate surface are used as shown in Figure 3.24: LL, L, M, R, RR. These

five points are symmetrically positioned, with point M being the midpoint. The deformation contours shown in Figure 3.24 are those at the time of maximum deflection, also shown quantitatively along the plate diameter in Figure 3.26 at $t = 167\mu s$.

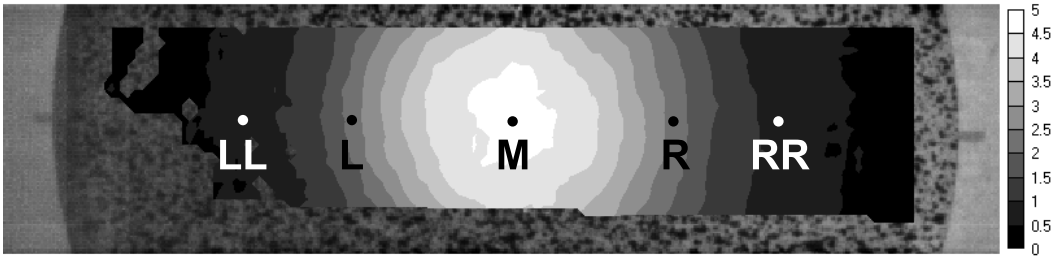

Figure 3.24. Physical location of points used to examine symmetry of deformation wave propagation, showing out-of-plane deformation contours at time of maximum deflection in mm

By analyzing the deformation-time history of each of these points, as shown in Figure 3.25, the initial plate deformation process can be understood. The center of the plate, M, is accelerated first and, as it deforms, the rest of the plate surface also begins to deform, starting at the innermost points L and R. The center point reaches its maximum deformation and then begins to move in the reverse direction. The other points reach their maximum deformations at short times later. The arrival of an in-plane deformation wave can be observed at points LL and RR at about $t = 0.3ms$, or $300\mu s$ after the initial deformation. The deformation wave propagates toward the plate center and arrives at the next points, L and R, at about $t = 0.5ms$. The deformation wave

arrival is noted by the change in slope of the plate deformation at these times, but is more easily seen in Figure 3.26.

Figures 3.26 and 3.27 show the deformation profiles of the plate diameter through the first $1500\mu s$ of the explosive event. After reaching its maximum deformation, as shown at time $t = 167\mu s$ in Figure 3.26, the plate begins to deflect back in the direction of the explosion center, as seen from Figure 3.25. This is the beginning of plate oscillations that occur for approximately $10ms$ before damping and leaving the plate in its final deformation profile.

After the plate has progressed through its maximum deformation, a deformation wave enters the measurement region near the circular fixture boundary, as noted above. This deformation wave appears to be a reflection from the clamped plate boundary. This wave grows in amplitude as it approaches the center of the plate. It can first be seen at $t = 333\mu s$ in Figure 3.26, but is more clearly visible at the two later times in the same figure. The deformation wave reaches the center of the plate between $t = 833\mu s$ and $t = 1000\mu s$ as shown in Figure 3.27. After this time the deformation wave decreases in amplitude and cannot be seen easily, although it continues to play an important role.

After the time shown in Figure 3.27 the plate continues to oscillate, completing a total of approximately two periods before damping to the final shape. The final profile, as shown in Figure 3.27, is highly dependent on the deformation wave that distorts the plate surface. The influence of this wave is further explored in Section 3.2.5.

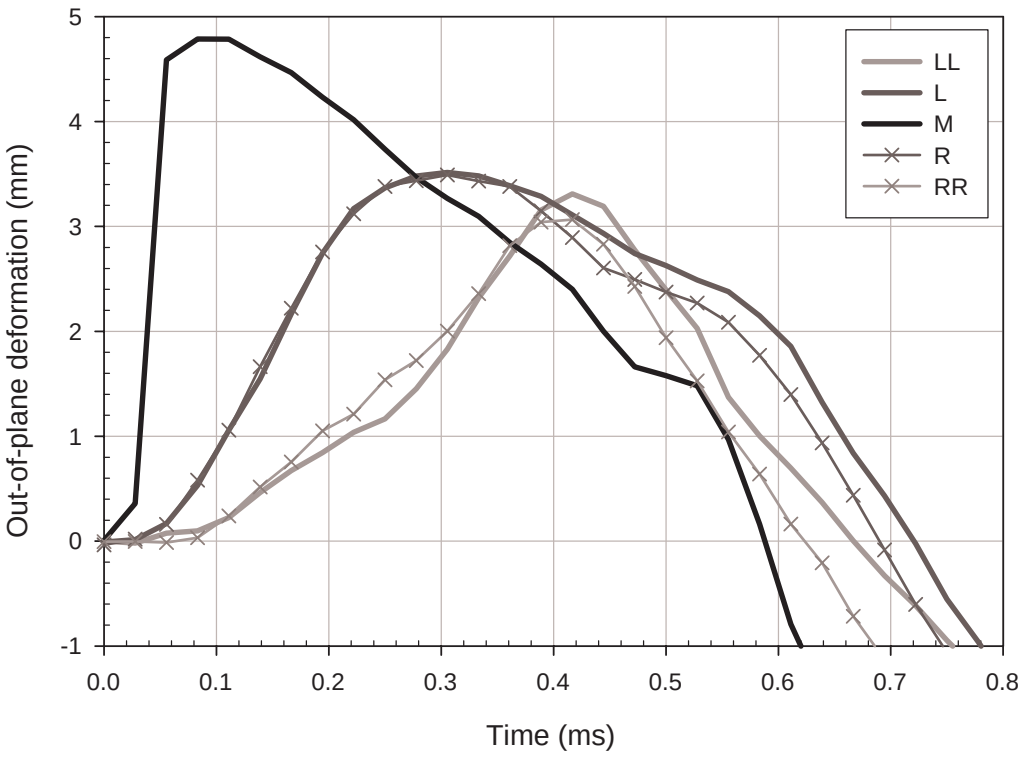

Figure 3.25. Deformation versus time for points along the plate surface showing initial plate motion

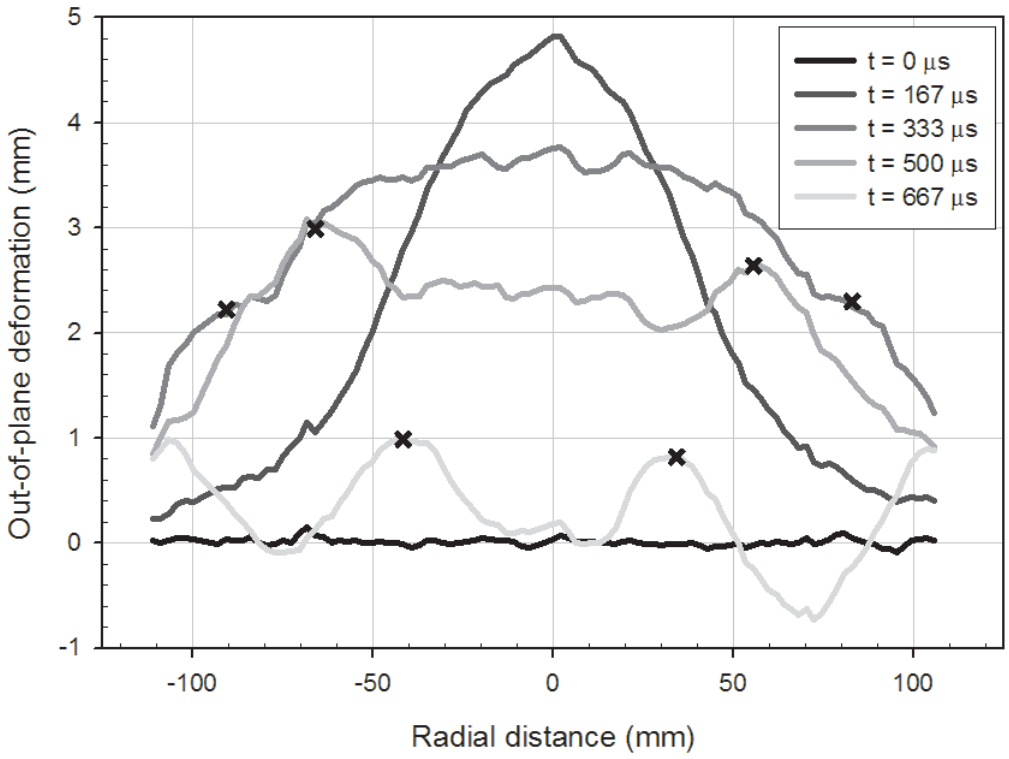

Figure 3.26. Out-of-plane deformation versus time for the horizontal diameter of a witness plate during the first $667\mu s$ of a typical test, each x represents the approximate position of the deformation-wave crest

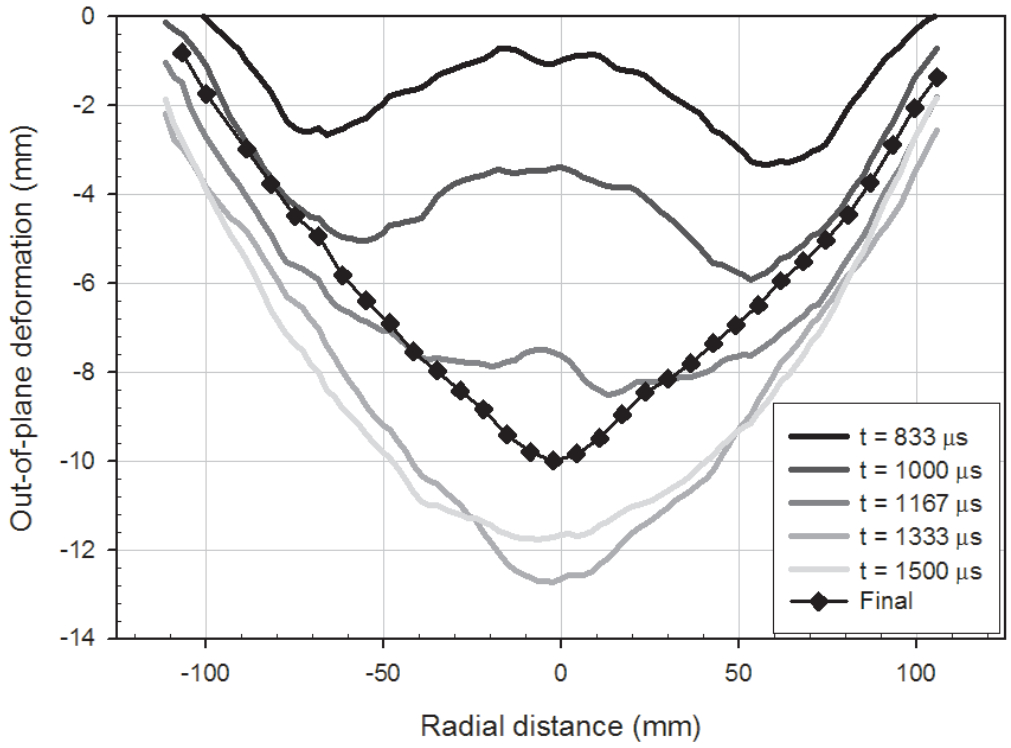

Figure 3.27. Out-of-plane deformation versus time for the horizontal diameter of a witness plate during the next $833\mu s$ of a typical test, also showing the final plastic deformation profile

3.2.4 Dynamic Material Deformation Results

The observed dynamic material response scales according to the explosive impulse applied to the witness plate. For the present study, the analysis of the dynamic response is limited to the initial plate motion up to its maximum deformation. Thereafter, the deformation wave created at the clamped plate boundary severely affects the total plate motion and complicates the results. The maximum plate deformation is therefore the final step of the dynamic response that can be simply analyzed with high accuracy in the current research setup.

Data from the present "shock-hole" witness-plate deformation experiments are summarized in Table 3.3 for PETN and in Table 3.4 for TATP. These results include the actual mass and stand-off distance for each charge. The explosive impulse is calculated by first scaling the charge mass and distance to a $1g$ charge, then determining it from the data presented in Figure 3.11. Two impulse values are given, a maximum and an average. The maximum is the impulse applied at the plate center. The average impulse is calculated by first determining the incident impulse at each location on the plate surface. These incident values are then integrated over the entire plate surface to determine an average incident impulse for each experiment.

The dynamic deflection is the maximum plate deformation along a diameter of the exposed plate surface, prior to the arrival of the deformation wave. Figure 3.25 shows that the plate surface begins to move away from its maximum deformation before the in-plane deformation wave interferes with the measurement. Thus the maximum

deflection is independent of the deformation wave, and is a straightforward indicator of the witness-plate response.

The final plastic deformation measurement data are also presented here, but are not discussed until Section 3.2.5. Dynamic deflection data are not given for TATP experiments 3 and 13 because these experiments were recorded at only $10,000 fps$ for the symmetry measurements, Section 3.2.1, and thus did not accurately capture the maximum deformation.

The maximum dynamic deformation data versus maximum impulse from Tables 3.3 and 3.4 are shown in Figure 3.28. Figure 3.29 shows the same data, but with limited axes to better show the TATP results. The error bars in both figures represent the uncertainty in explosive impulse as shown in Figure 3.11. The error increases with increasing impulse for each explosive material. The error in deformation measurement, as discussed in Section 3.2.2, is approximately $\pm 0.10 mm$ and represented by the symbol size in Figure 3.28.

Figure 3.28 shows one benefit of using multiple explosive materials: error reduction in the region of impulse overlap. The error for TATP at an impulse of $20 Pa * s$ is large, but at the same impulse, PETN has a much smaller error bar. The error for TATP is larger because the TATP must be placed closer to the plate surface to obtain the same impulse as PETN at a larger stand-off. The present experimental data have increasing error at decreasing stand-off distance from the explosive. Thus, measurement error can be minimized by conducting experiments at larger stand-off distances. The stand-off distance can be increased without limit, although at larger distances the shock wave becomes almost planar and impacts the entire plate surface at once. This change

Table 3.3.
Summary of material deformation experiments using PETN

Test	Charge mass (g)	Stand-off distance (m)	Incident impulse Maximum ($Pa*s$)	Incident impulse Average ($Pa*s$)	Dynamic plate deformation (mm)	Final plate deformation (mm)
1	0.82	0.145	19.5	14.8	5.91	–
2	0.84	0.130	23.6	17.6	6.49	–
3	0.94	0.120	28.4	21.3	8.33	–
4	0.90	0.115	28.8	21.4	7.55	−16.73
5	0.64	0.080	31.2	21.7	7.80	−16.24
6	0.74	0.090	31.3	22.5	8.49	−16.48
7	0.75	0.075	35.5	25.3	10.51	−17.88
8	1.02	0.091	37.1	28.3	11.51	−20.00
9	0.89	0.080	37.4	27.6	11.10	−19.59
10	1.00	0.085	38.4	29.0	10.94	−18.89
11	0.65	0.060	38.4	25.2	10.20	−17.73
12	0.70	0.060	40.1	26.5	10.54	−17.49
13	0.59	0.050	42.1	25.2	9.98	−16.82
14	0.98	0.070	43.5	31.2	12.49	−19.88
15	0.85	0.055	48.7	31.1	11.77	−18.75
16	0.90	0.050	55.1	33.2	14.09	−22.13
17	0.82	0.035	57.0	34.3	15.41	−20.46
18	0.88	0.035	58.6	35.9	16.57	−20.72
19	0.90	0.035	59.1	36.4	16.20	–

Table 3.4.
Summary of material deformation experiments using TATP

Test	Charge mass (g)	Stand-off distance (m)	Incident impulse Maximum ($Pa*s$)	Incident impulse Average ($Pa*s$)	Dynamic plate deformation (mm)	Final plate deformation (mm)
1	0.60	0.150	5.5	2.8	1.94	−7.13
2	0.60	0.110	9.5	6.4	2.66	–
3	0.59	0.080	12.6	8.5	–	2.31
4	0.61	0.080	12.9	8.7	3.48	2.12
5	0.55	0.070	13.2	8.7	3.21	1.32
6	0.67	0.070	14.6	10.1	4.04	−9.17
7	0.62	0.060	15.2	10.2	4.01	2.34
8	0.53	0.050	15.3	9.7	3.79	−7.75
9	0.63	0.060	15.3	10.3	4.03	2.18
10	0.67	0.060	15.8	10.8	4.27	2.13
11	0.62	0.050	16.5	10.8	4.61	−8.59
12	0.59	0.040	17.5	11.0	4.83	−10.00
13	0.60	0.040	17.7	11.2	–	2.81
14	0.55	0.030	18.5	11.0	5.42	–
15	0.69	0.040	18.8	12.2	5.14	−10.18
16	0.65	0.030	19.9	12.2	5.16	−9.93
17	0.72	0.030	20.7	13.0	6.65	–

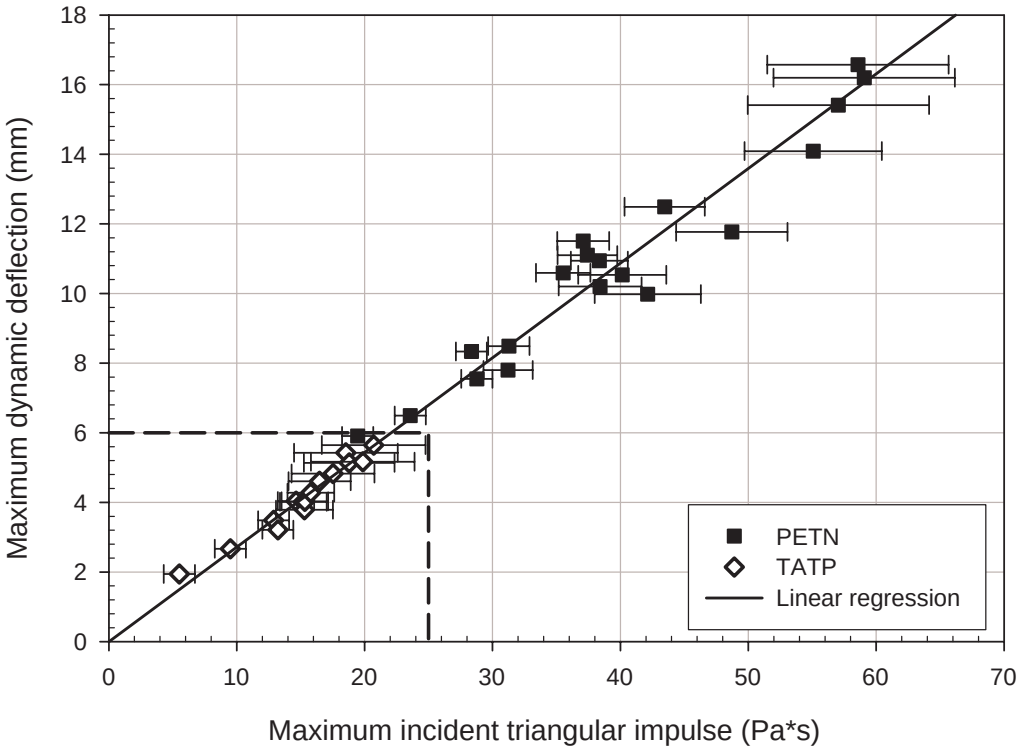

Figure 3.28. Maximum dynamic deformation versus maximum incident triangular explosive impulse, the region of Figure 3.29 is shown by the dashed line

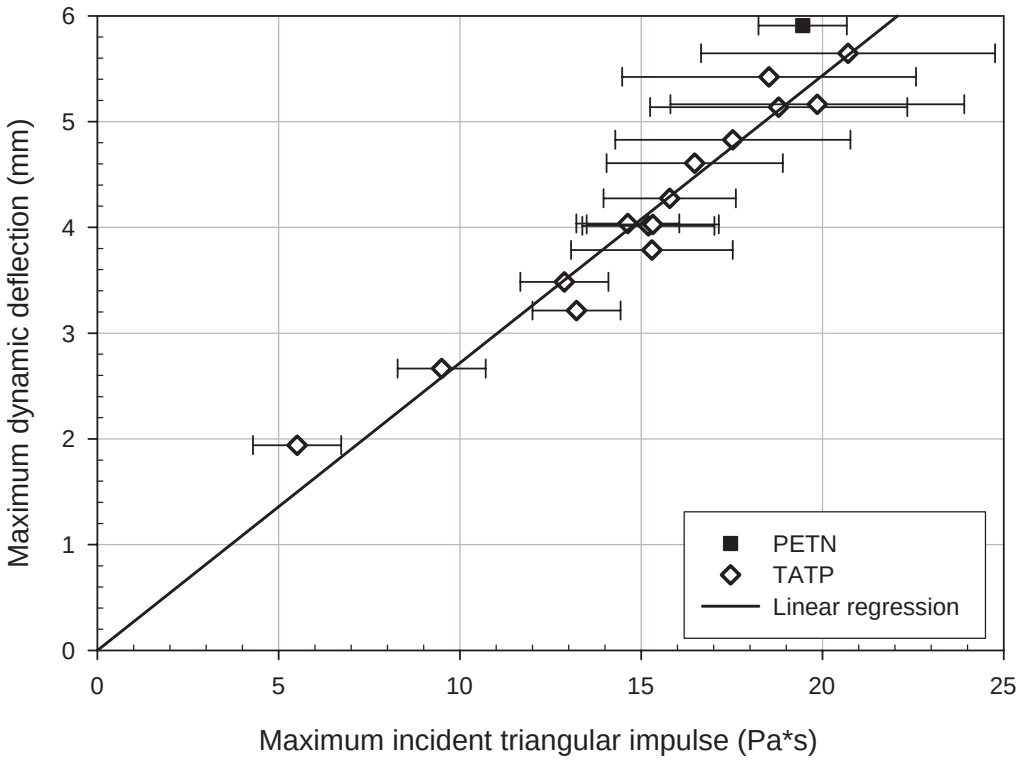

Figure 3.29. Maximum dynamic deformation versus maximum incident triangular explosive impulse, detail

in plate loading could affect results but is not presently studied. The present results use both PETN and TATP across a range of stand-off distances. By judiciously experimenting with two explosive materials, the range of applicability of each can be explored, while using the combined data to reduce overall errors.

Figure 3.30 shows the maximum plate deformation as a function of average incident explosive impulse. This figure is similar to Figure 3.28, but shows a slightly different qualitative data collapse. The one region of particular interest is for experiments $7-13$, with maximum incident impulses from about 35 to $42 Pa*s$. This region has a distinct spread about the linear regression line in Figure 3.28, but collapses almost perfectly in Figure 3.30. This significant data collapse suggests that some degree of impulse averaging is required.

The extremes of the PETN data in Figure 3.30, however, appear to deviate slightly from the linear regression when the impulse is averaged. This deviation suggest that a simple averaging is not appropriate for all stand-off distances. Some time averaging is likely also required to accurately determine the precise average impulse value to collapse all data. Computational investigation of the effect of impulse variation would assist in the development of an appropriate averaging function for these experiments.

Overall, the regressions shown in Figures 3.28, 3.29, and 3.30 highlight the approximately-linear relationship between maximum dynamic deflection and explosive impulse. The regression calculations were forced to go through the origin to maintain physical realism. This linear relationship is valid for the present data, but is not expected to be applicable outside of the present data range. The present data range is limited to experiments where the witness plate did not fail or tear. More experiments should be

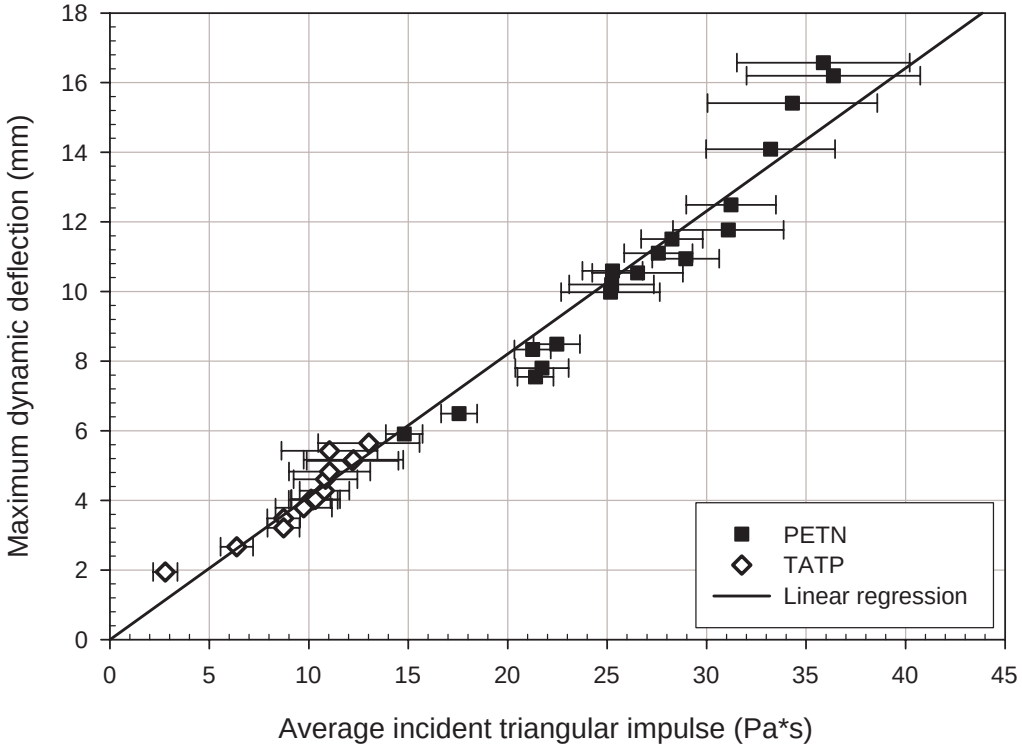

Figure 3.30. Maximum dynamic deformation versus average incident triangular explosive impulse

performed with larger PETN charges or another, more powerful explosive to explore the limits of the trend as the witness plates approach failure.

The present results are also only expected to be valid for the same aluminum alloy and witness plate dimensions. Ultimately, similar research conducted with witness plates of various thickness and exposed surface area would build a broader understanding of the scaling of material responses. With more experimental data, a process for extrapolating small-scale results to full-scale predictions can also be developed.

The present work can also be used to validate computer models. Computational models of the small-scale experiments can be directly validated with this experimental data set and procedure, with no scaling required. These ideas are discussed further in Section 4.2.

3.2.5 Plastic Material Deformation Results

The permanent plastic plate deformation measured here is highly dependent on the plate mounting fixture. The present fixture causes a deformation wave to occur within the plate surface which affects the plate motion after the time of the maximum deformation. The final deformation profile is also affected by small asymmetries in explosive charge placement and the resulting asymmetry of the deformation wave motion.

The results presented in the last column of Tables 3.3 and 3.4 are the maximum permanent deformation along the horizontal diameter of each experimental witness plate. The image pair used to determine the final plate shape is recorded about 3 minutes after the experiment. This measurement is therefore free of all plate and fixture motion. Experiments with no final deformation either had correlation failures preventing the final

measurement, or had significant asymmetries. As discussed, asymmetries arise after the maximum deformation occurs, and can inhibit the ability to perform a final deformation measurement.

The results, presented graphically in Figure 3.31, show that the final plate shape can be either positively or negatively deformed, but is usually the latter. Positive deformation indicates that the plate surface deformed away from the explosive charge, in the same direction as the initial deflection. Negative deformation occurs when the final plate surface is closer to the explosion center than its original position at the experiment start. The error associated with each data point is based on the error in the determination of the explosive impulse and is the same as that discussed in Section 3.2.4 and shown in Figure 3.28.

The data can be clearly segregated into two distinct groups. Although scattered, each group appears to have a clear relationship between average incident explosive impulse and resulting plastic deformation, connecting both explosive materials used. The linear regressions shown represent the general data trends, with the realistic constraint of zero deformation at zero impulse applied.

The two data groupings, however, cannot be separated by examining impulse or any other input variable conditions. The results show that, for an impulse within a certain range, either a positive or negative final deformation profile is possible. The final deformation is apparently determined by the symmetry of the deformation wave motion within the plate surface during the event, following maximum deformation.

The first difference between the two groupings can be seen by examining the deformation-time histories of witness-plate center points. Figure 3.32 shows the plate

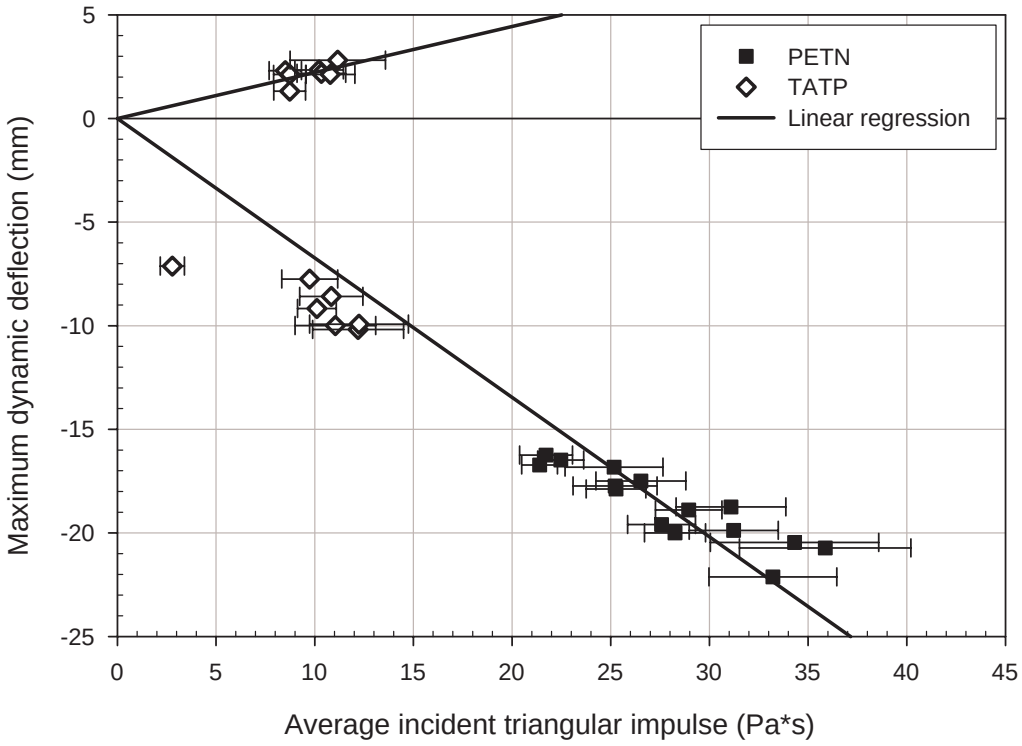

Figure 3.31. Maximum plastic deformation versus average triangular explosive impulse

center deformation throughout the explosive event for four representative TATP experiments. The TATP experiments are numbered according Table 3.4. The last point on each curve is the final deformation measurement reported in Table 3.4. The maximum deformation in the first peak is also the maximum dynamic deflection recorded in the same table.

Figure 3.32 shows that, for these experiments, the deformation history is essentially the same through the first period of oscillation. Once the center point begins to retract following the second maximum deflection, the profiles diverge into two primary groups. The first two experiments, 4 and 7, move in the negative direction fastest, but also have a small ripple of positive motion before moving toward a minimum deflection. Experiments 12 and 16 maintain the second maximum deflection before moving in the negative direction, at approximately the same rate as in the previous experiments. Experiments 4 and 7 return to a positive deformation while experiments 12 and 16 settle to a negative deformation approximately equal to the second negative deflection. These experiments typify the differences between the deflection profiles for tests that result in positive versus negative deformations.

Experiment numbers 4 and 12 are investigated further to show more differences in these deformation histories and resulting permanent deflections. To document the location of the in-plane deformation wave, the five points previously shown in Figure 3.24 are used. The point labels are used to refer to each point throughout Figures 3.33 and 3.34 and also within the following discussion.

The first case considered is that for symmetric motion of the deformation wave, as seen in experiment 12 and Figure 3.33. As the plate approaches the second minimum

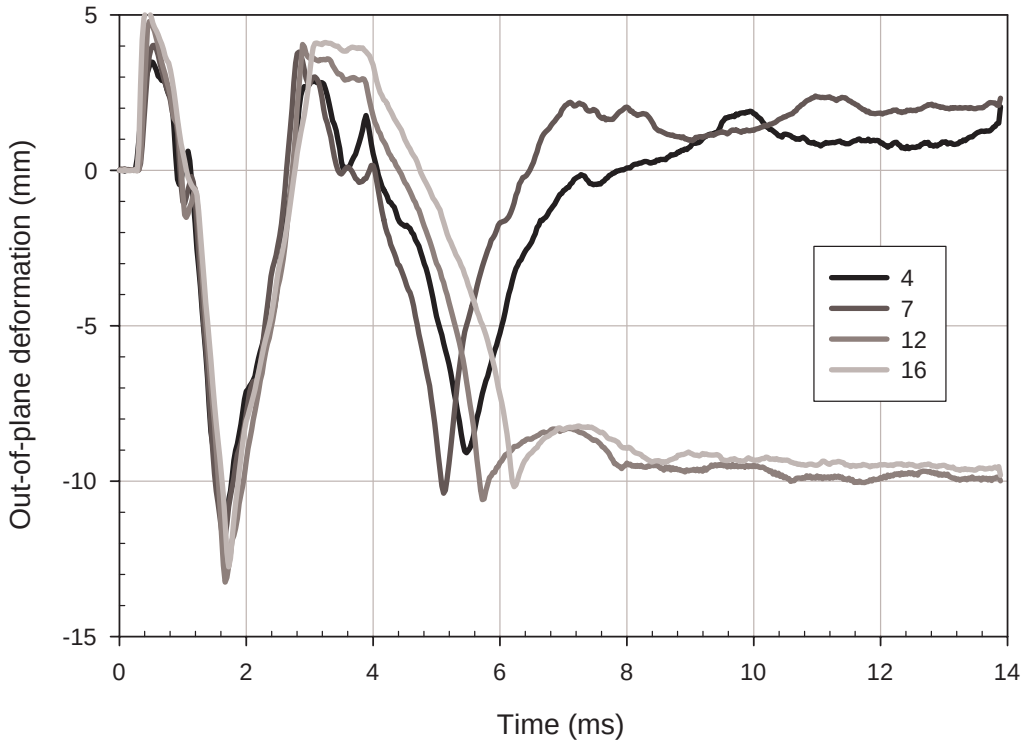

Figure 3.32. Plate center deformation versus time for representative TATP experiments

deformation, the center of the plate, M, is the last of all the points to reach its minimum. The edge points, LL and RR reach a minimum and rebound, indicating that a deformation wave passed these points at approximately $t = 5ms$. The wave then travels through points L and R, causing a local minimum at a time of about $t = 5.5ms$. Finally the wave arrives and focuses at point M, creating the second minimum. The entire plate surface rebounds slightly but quickly settles to the final deformation profile, with local deformations similar to the values obtained as the deformation wave passed.

The symmetric deformation wave arrives almost simultaneously at points of equal radial distance from the center, as shown in Figure 3.33. The symmetric arrival of the deformation wave at the plate center causes a maximum negative deformation to occur. This maximum negative deformation is approximately equal to the final plate deformation profile. The strain measurement shows that the deformation wave effectively cancels itself through destructive interference at this point.

The asymmetric deformation wave motion is observed in experiment 4 and shown in Figure 3.34. As the asymmetric plate deformation approaches the second negative maximum deformation, the two sides of the plate reach local minimums at different times. As shown in Figure 3.34, the left side of the plate, points LL and L, are the first to reach minimums. The plate center, M, is then affected, followed by points R and RR respectively. In this asymmetric case, the deformation wave appears to be propagating through the plate from left to right. This case has no destructive interference during the second oscillation, allowing the plate surface to rebound to a positive final displacement.

Figure 3.35 shows principle strain versus time for the plate center, and provides insight in determining the final plate deformation profile. The noise in the data is likely

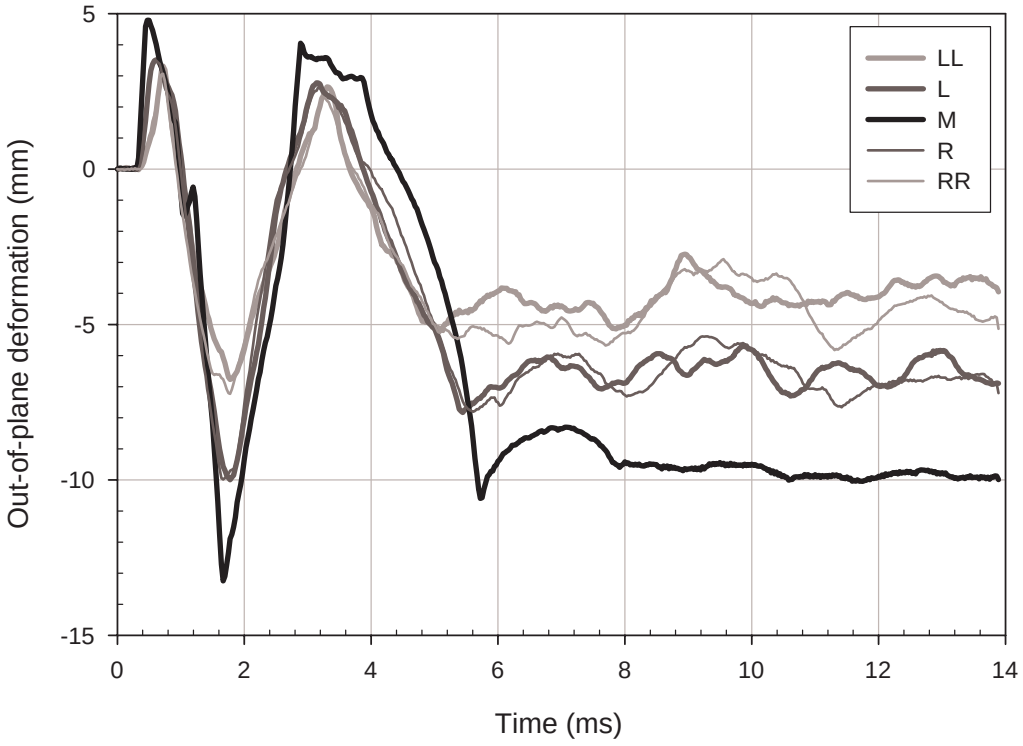

Figure 3.33. Deformation versus time for points along the plate surface during experiment 12 showing symmetric deformation wave propagation

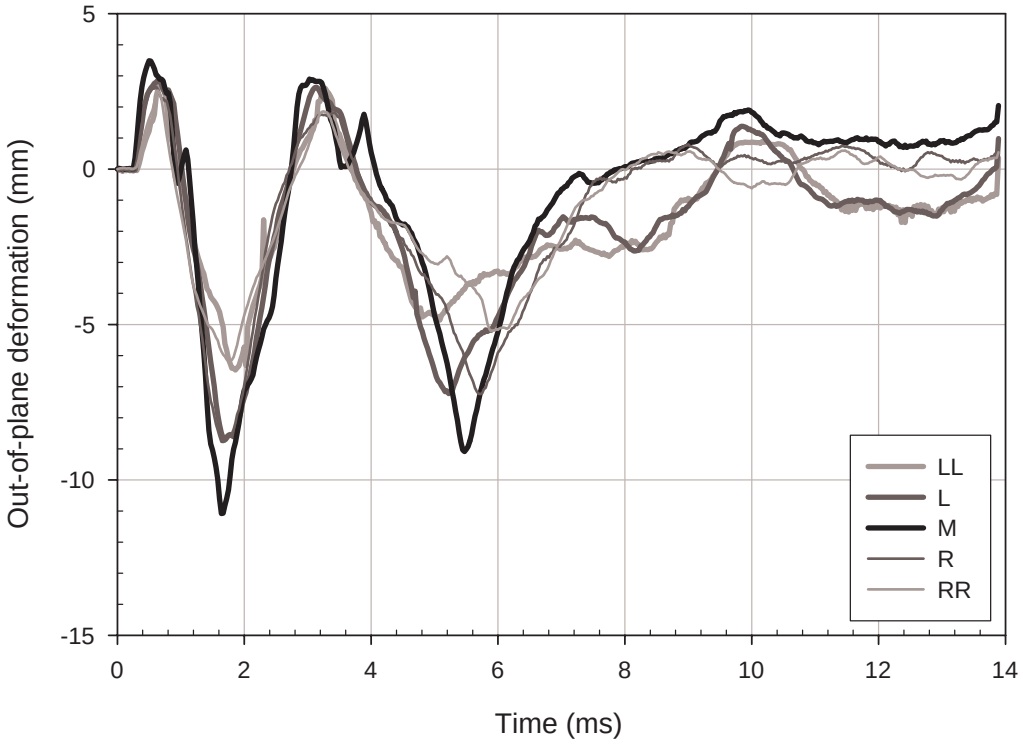

Figure 3.34. Deformation versus time for points along the plate surface during experiment 4 showing asymmetric deformation wave propagation

due to the numerical method by which the Correlated Solutions software determines strain. Although the data are noisy, the general trends are used to infer information about the deformation event.

Both plates initially show approximately the same strain profiles up to a time of $3ms$, which corresponds to the end of the first period of oscillation and the occurrence of the second maximum positive deformation. At $3ms$ both experiments have an sudden increase in strain, but the symmetric plate in experiment 12 has a more significant increase followed by a plateau at the higher strain level.

Another strain increase occurs for both plates at about $4ms$, which corresponds to the unusual spike in Figure 3.34 and the beginning of negative motion for the plate in Figure 3.33. This second spike in the symmetric case could correspond to constructive interference of the deformation wave, creating a peak in strain at the plate center. The corresponding strain profile in the asymmetric case shows systematic increases and decreases in strain between 4 and $6ms$, potentially showing the motion of asymmetric deformation waves traveling within the plate.

The symmetric plate strain is rapidly relieved at $6ms$, corresponding to the time of the second maximum negative deformation in Figure 3.33. This sudden drop in strain essentially fixes the plate deformation profile. After this point there is no significant strain relief and the plate oscillations damp to leave the plate in its final shape with minimum strain. The strain and deformation profiles show that the in-plane deformation wave effectively canceled itself at the time of this second negative deflection. After this point, the plate does not appear to oscillate or change strain, indicating that motion has

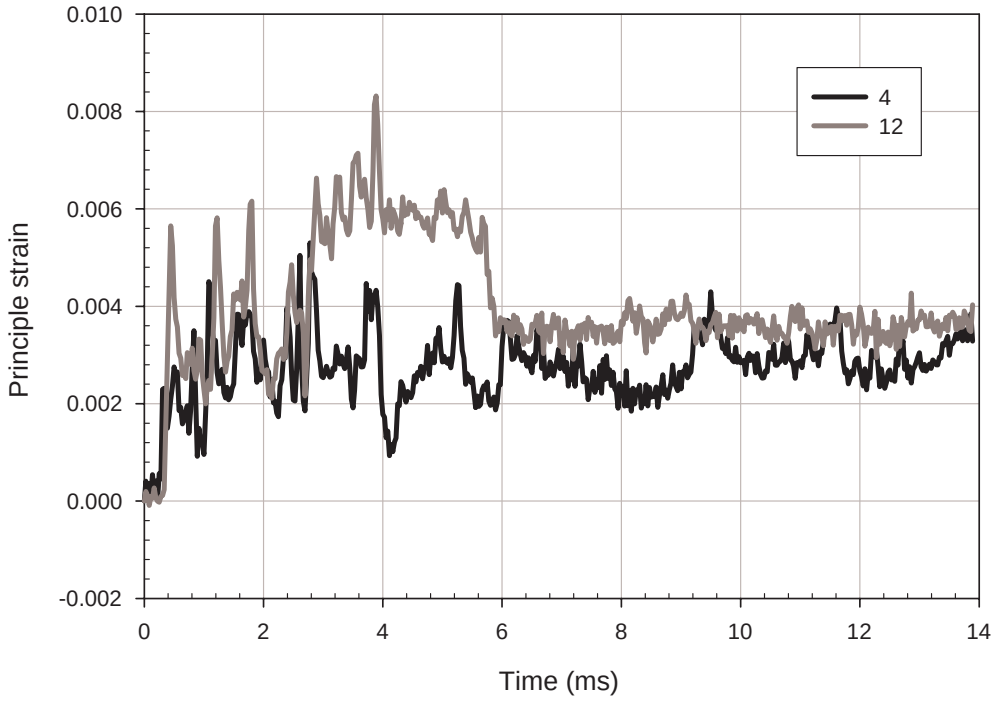

Figure 3.35. Principle strain versus time for the plate center point in experiments 4 and 12

ceased and that the energy imparted to the plate by the explosion has been dissipated through plastic deformation.

The asymmetric plate case has nearly continuous, low-level motion occurring throughout the time period analyzed. This continuous motion suggests that the deformation wave is still moving within the plate, oscillating in a near-random reflection pattern. The plate center point also has a continually oscillating strain profile. This point has several times at which strain is rapidly relieved, but the plate does not appear to be able to maintain a strain level as the symmetric case did.

Figure 3.35 shows that the final deformation of both plates results in a similar strain at the center of the plate. This final strain could be indicative of the amount of energy each plate absorbed during the explosive event. The strain for experiment 12 is slightly larger than experiment 4, reflecting the slightly larger impulse applied to 12 compared to 4. Further research could be conducted to determine the amount of energy absorbed by the plate and compare this to the total strain throughout the plate surface. Determining the amount of energy absorbed by a material would assist in developing blast-resistant materials.

The asymmetric deformation wave propagation is most likely due to the explosive charge being positioned improperly. If the shock wave from the explosion does not impact the plate center first, deformation inconsistencies and asymmetries would be expected. These asymmetries, however, do not affect the measurement of the maximum witness plate deformation. The initial deformation data can also be used for the inverse material property definition process. If permanent plastic deformation measurements are desired, the asymmetries must be eliminated. To do this, future experiments should

investigate new methods to accurately and precisely position the explosive charge on the plate centerline at a known distance. Future research should also focus on changing the plate fixture design in an to eliminate any reflections from from the boundary and thus inconsistencies in the final deformation profiles.

Chapter 4

CONCLUSIONS AND RECOMMENDATIONS FOR FUTURE RESEARCH

4.1 Summary and Conclusions

Modern laboratory equipment and techniques provide novel opportunities to conduct explosive research on the laboratory scale. Traditional scaling techniques allow these experiments to be conducted in a controlled environment where new data collection techniques can be applied, then scaled for comparison with full-scale explosions. High-speed digital cameras combined with traditional shadowgraph visualization and modern digital image correlation techniques facilitate unprecedented experimental approaches to measuring explosive yield and an associated material witness plate blast response.

The practice of defining explosive yield through a single TNT equivalence value has become outdated [7]. Modern explosives, including peroxide-based and aluminized mixtures, exhibit unusual explosion or combustion characteristics. These novel characteristics cannot be entirely captured via the traditional explosive characterization procedures. New procedures using both optical shock-wave imaging and piezoelectric pressure measurements must be used to fully characterize explosive yield as a function of distance from a charge.

The initial laboratory-scale explosion research concentrated on schlieren measurements of shock propagation from ideal milligram explosions [7]. The present research has expanded upon this earlier work to include piezoelectric pressure measurements and computational simulations of two radically different explosive materials. Pentaerythritol tetranitrate (PETN), an ideal secondary explosive, was used to validate the measurement techniques with archival data and computational models. Triacetone triperoxide (TATP), a highly non-ideal primary explosive, was used to extend the verified techniques toward understanding the yield of a modern explosive material.

Results from PETN experiments extend the traditional scaling laws to the gram-range for this conventional military explosive. The measured shock propagation from a $1g$ explosive charge matches the computed shock propagation from a $1kg$ charge when both are scaled according to the traditional Hopkinson scaling [4]. This agreement extends the traditional scaling law and validates the novel laboratory-scale experimental procedure given here. Prior to the present work, no research had compared laboratory-scale shock propagation measurements with similar large-scale computational or experimental results.

The experimental measurements of overpressure duration supported Kinney and Graham's theory for obtaining the overpressure duration from a shock Mach number versus radius profile. The present research showed that the measured overpressure duration from $1g$ PETN charges matched that predicted from the measured shock Mach number versus radius profile. These data are the first experimental measurements that have been compared to Kinney and Graham's theory. The agreement between the physically-derived theoretical argument and experimental measurements support the theory within

experimental error. The experimental and theoretical results, however, did not agree with computational predictions.

Computational predictions showed a non-physical increase in overpressure duration within a specific range of radii from the explosive charge. Upon further investigation it was determined that the computationally-determined contact surface was affecting the overpressure duration within this radii range. The contact surface propagation prevented the overpressure from decaying to atmospheric pressure within the expected time, resulting in an artificially high overpressure duration. This discrepancy has not been noted in any previously-published works. The experimental data repeatability and agreement with published TNT data indicate that the computational simulation is suspect. It is recommended that this discrepancy be further explored to determine how the issue should be addressed in future computational simulations.

Experiments were also performed to document the shock propagation and thus explosive yield from charges of TATP. The explosive properties of this novel explosive material were previously under-documented, with most work focusing on the chemical decomposition process. The present work applied traditional scaling laws and found that TATP shock propagation results do indeed scale for charges of mass within the 0.5 to $5g$ range. The TNT equivalence value was also found to vary as a function of shock wave radius, and was significantly lower than previously-published estimates. This disparity is likely due to different initiation and measurement methods, with the present result accurately reflecting the explosive damage potential for this material.

The experiments using PETN and TATP resulted in shock Mach number versus radius profiles for each explosive material. These profiles represent a detailed characterization of the explosion in terms of the shock wave propagation and subsequent explosive impulse. This relationship determines an explosive impulse versus radius curve for each explosive, which is essential for estimating the potential damage to an object near an explosion of a given mass. The explosive impulse is the product of the measured incident shock overpressure and its duration at each radius. It is the explosive impulse thus determined that is used as an input condition for the present witness-plate blast response research.

Thin witness aluminum plates were clamped into a "shock-hole" fixture, then subjected to known explosive impulse loads. The shock-hole fixture was designed to allow optical access so the aluminum plate deformation could be dynamically measured. The resulting three-dimensional optical measurements of the plate response showed that the deformation was dependent on both the applied explosive impulse and the geometry of the shock-hole fixture.

The explosive impulse was found to be the controlling parameter in the dynamic deformation of the aluminum plate. The applied impulse caused localized deformation at the center of the plate. The plate surface was found to reach a deflection in the direction away from the explosive charge. This maximum deflection magnitude was determined to be linearly dependent on the applied explosive impulse, over the range of conditions tested. This linear relationship was found to be independent of explosive charge material used. Experiments performed with PETN and TATP at the same impulse conditions showed the same dynamic deformation, within the experimental error. The explosive

impulse as determined here, from the shock Mach number versus radius explosive characterization procedure, is therefore the primary variable controlling dynamic material deformation.

After the initial deformation, however, a deformation wave reflection from the clamped boundary condition affected the remaining deformation measurements. This reflection wave was found to induce significant, complex strain within the witness plate. The reflection was also highly dependent on the charge placement and resulting impulse symmetry. Small errors or asymmetries in the explosive charge placement and initial maximum deformation translated into radically-different final deformation profiles. The more symmetric experiments resulted in final plate deformations in the negative direction, i.e. toward the explosive charge location. This result seems counterintuitive, but can be explained by examining the local strain extrema caused by the interference of the reflection wave with itself. Asymmetric wave motion resulted in final witness-plate deformation in the same direction as the initial plate deformation.

The witness-plate material response results show the importance of the shock-hole fixture design. All motion after the initial deformation is affected by the observed in-plane deformation wave. This deformation wave is independent of the explosive impulse magnitude, but is dependent on the fixture design and experiment symmetry. Future experiments should therefore utilize a new fixture to prevent a significant deformation reflection from the witness-plate boundary. More advanced methods should also be incorporated to improve the symmetry of impulse application, and thus better resulting deformation trends.

Although the final witness-plate deformation profiles are corrupted by fixture design and experiment symmetry, the dynamic deformation measurements have been shown to be independent of these variables. It is this initial dynamic deformation measurement that is the most important result from these experiments. The initial witness-plate deformation process and data can be analyzed to inversely determine high-speed material properties or to validate computer models. The present research has developed the techniques required to perform these measurements and has shown the limitations of traditional methods which only examine permanent witness-plate deformation.

Overall, the present research has demonstrated the capabilities and potential for explosive research on the laboratory scale. These preliminary results have extended previous scientific ideas to the laboratory scale and have applied new techniques toward improving the understanding of explosive events. Laboratory-scale experiments may never completely replace full-scale testing, but they offer a unique opportunity to conduct experiments in a highly-controlled environment with well-documented boundary and input conditions. These laboratory-scale tests therefore provide an appropriate forum for significantly increasing the scientific understanding and knowledge of explosive events and associated material responses.

4.2 Recommendations for Future Research

This thesis covers only a fraction of the experimental research that could be conducted with characterized laboratory-scale explosives. With the continuing development of exotic explosive materials and digital instrumentation technology, the scientific

knowledge potential is expected to continue to increase for the field of laboratory-scale explosive research.

The present work has developed an explosive characterization procedure that has been verified for two different explosive materials. This work can easily be extended to other novel and traditional explosive materials to build a library of explosive characterizations. This has the potential to replace the outdated library of TNT equivalence values and thus help develop an improved standard for explosive characterization.

The ability to apply these techniques could be limited in some cases by explosive material properties that do not scale appropriately to the laboratory scale. This problem is already foreseen, for example, for TNT, which cannot be reliably detonated in charges smaller than approximately $5kg$. Scale limits may also be discovered for other explosive materials, especially those with large critical diameters [48]. In these cases, large-scale experiments should still be performed in order to obtain the same information to continue to build the scientific database.

The experiments documenting shock radius versus time can also be used to develop computational models of explosive materials, including newer exotic explosives. Determining an equation of state or numerical representation for explosion products is difficult from a chemical reaction approach, but with experimental data, JWL equation of state coefficients could be iteratively determined. The present data for TATP could be used to define a JWL equation of state which would then allow its use in larger computational simulations. The present experimental approach avoids the complex chemistry

involved in some explosives, such as thermobaric explosives, and provides a simpler measurement of explosive yield. These results can also be applied directly to the development of computational models.

Along with building an explosive material library, experiments should be completed to further investigate the variation of overpressure duration with respect to radius. The Kinney and Graham hypothesis [1] has been preliminarily confirmed here, but more experiments are required. Future experiments should investigate the propagation of the contact surface between the expanding explosive fireball and the surrounding air. Experimental documentation of the contact surface motion can then be compared with computational results to evaluate its effect on overpressure duration. Understanding the overpressure duration variation is essential in determining the explosive impulse behavior, which is directly tied to material blast response research.

Laboratory-scale material blast response research has many potential directions and applications that should be explored. The present work has demonstrated procedures, the application of optical techniques, and problems with the initial setup which can be further developed. Future work must first develop a new shock-hole fixture to reduce or eliminate the in-plane material deformation wave. A larger exposed plate surface will likely decrease the influence of this deformation wave, but iterative fixture development may be required. Ultimately, a fixture should be developed to avoid reflection from the boundary condition if possible. With such a fixture, more material deformation experiments could be performed to examine permanent witness-plate deformation.

The initial trend of dynamic material deformation versus explosive impulse should also be verified for the new fixture using characterized explosives. The choice of explosive

materials can be expanded to include other explosives that have been characterized through the presented procedure to further support explosive impulse as the controlling parameter.

The range of applied impulses can also be extended up to plate failure. The present research did not explore this region due to safety concerns for researchers and equipment, but future setups could guarantee the safety of both and thus extend the impulse range.

With the entire impulse range explored, the collected data could then be used to determine the high-strain rate material properties for the present aluminum alloy. These material properties could be evaluated through iterative computational simulations or an inverse evaluation algorithm. With known impulse, boundary conditions, and resulting deformation, linear and non-linear material properties could be evaluated for this alloy and any other material that was thus tested. Once the material property evaluation procedure is confirmed, a range of traditional and novel materials could be tested to build a new, broader material property database.

In parallel with this inverse material property evaluation work, high-resolution experimental data for a range of scenarios should be developed. These data could easily be used for computational code validation. After computationally validating a code with laboratory-scale experiments, the computation could be applied to a full-scale blast scenario. Currently, insufficient data exist to validate computer models for large or small-scale scenarios, but the present research techniques could easily be applied to develop the required experimental data.

Additionally, the present optical measurement approach could be applied to material response to ballistic impact. This fundamentally-different phenomenon could be characterized by a localized loading based on the resulting material response. Understanding the loading and material response characteristics could lead to the development of protective materials which could be used in a wide range of fields.

Throughout these suggested experiments, the digital instrumentation technology used will continue to improve. Future high-speed cameras, with greater frame rate and resolution capabilities, will allow explosions to be characterized at smaller radii, eventually approaching the physical charge radius. The material response measurements will also improve. The uncertainty in these measurements will decrease and improved time resolution will allow more precise strain and strain-rate measurements to be made. These improvements will directly affect the material model development and thus computational validation capabilities.

The present research has combined traditional experimental methods with novel technological developments to advance the scientific understanding of explosive characterization and material blast response at the laboratory scale. This initial research effort has developed a basic understanding of the techniques and information required to assist in the development of advanced explosive and blast-resistant materials.

Appendix A

Pentaerythritol Tetranitrate

A.1 PETN Synthesis Procedure

Materials

- $70mL$ HNO_3, $68-70\%$ pure
- $50mL$ H_2SO_4, $95-98\%$ pure
- $20g$ pentaerythritol
- $900mL$ distilled ice water
- $400mL$ acetone heated to $50^{\circ}C$
- $120mL$ distilled ice water
- Sodium bicarbonate dissolved in water for acid neutralization
- Acetone bath, $T < -25^{\circ}C$
- Water bath $45^{\circ}C < T < 50^{\circ}C$
- Ice water bath for emergency reaction stop

Equipment

- $200mL$ beaker
- 2 $1000mL$ beakers
- $2000mL$ beaker
- Funnel
- Filter paper

- Stirring rod
- Water spray bottle
- Heated bath
- Insulated cold bath
- Thermometers
- Safety glasses
- Rubber gloves

Procedure

1. Combine HNO_3 and H_2SO_4 in $200mL$ beaker
2. Place acid beaker in cold acetone bath until $T < -15^{\circ}C$
    - If too cold, $T < 30^{\circ}C$, reaction may go too slow, so remove beaker from bath
3. Add pentaerythritol, $4g$ at a time, until all has been added
    - Stir constantly to avoid reaction hot spots and thus dangerous brown gas
    - If a brown gas is seen, immediately dump entire reaction beaker into emergency ice water stop bath
    - Keep reaction $T < -10^{\circ}C$, as reaction heats, slow the rate of pentaerythritol addition
    - Mixture will become thick
4. Stir for 10 minutes after all pentaerythritol has been added, while keeping $T < -10^{\circ}C$
5. Place reaction beaker into hot water bath, $45^{\circ}C < T < 50^{\circ}C$, and stir for 25 minutes
6. Pour mixture into $900mL$ distilled ice water

7. Allow precipitate to settle, then filter and rinse with water and sodium-bicarbonate solution
    - The filtrate is PETN, with some impurities
    - When the sodium-bicarbonate is added, the filtrate will bubble, this is typical and is due to the base neutralizing the acid
    - Continue to alternate water and sodium-bicarbonate washes until the filtrate does not foam when the sodium-bicarbonate is added
8. Add filtrate to $400mL$ acetone heated to $T = 50^{\circ}C$ and stir
    - This is a purification step, PETN will dissolve and impurities will not
    - PETN solubility in acetone = $58g/100mL$ at $T = 50^{\circ}C$
9. Filter acetone solution into $1200mL$ ice water
    - PETN will precipitate as the solution enters the water
    - The water should be as cold as possible
10. Let PETN settle, then filter and dry
    - PETN is now in the form of large icicle-like crystals
    - Typical yield is approximately $40g$ PETN

A.2 PETN Chemical Purity Estimation

X-ray diffraction (XRD) was used to estimate the chemical purity of the PETN produced by the procedure described above. XRD is a non-destructive analysis technique typically used to identify substance composition and purity. A sample of the PETN used here was compared to a PETN reference. This analysis was done at the National Institute of Standards and Technology (NIST) [51].

A qualitative purity estimate is made by comparing the unique diffraction lines of the standard reference material to those of the unknown sample. The output data are shown in Figures A.1 and A.2. Each peak location in the figures represents an underlying structure in the material, thus a chemical component of the sample. Peak intensity is a function of sample preparation only and does not indicate purity. The intensity was not calibrated or considered here.

As seen in the figures, the peak locations align almost exactly between the sample and reference material, with a small anomaly at approximately 39 degrees. This anomalous peak represents the only impurity in the sample. Unfortunately, the chemical identity of the impurity was not determined. Overall, the sample is estimated to be at least 95% pure PETN [51].

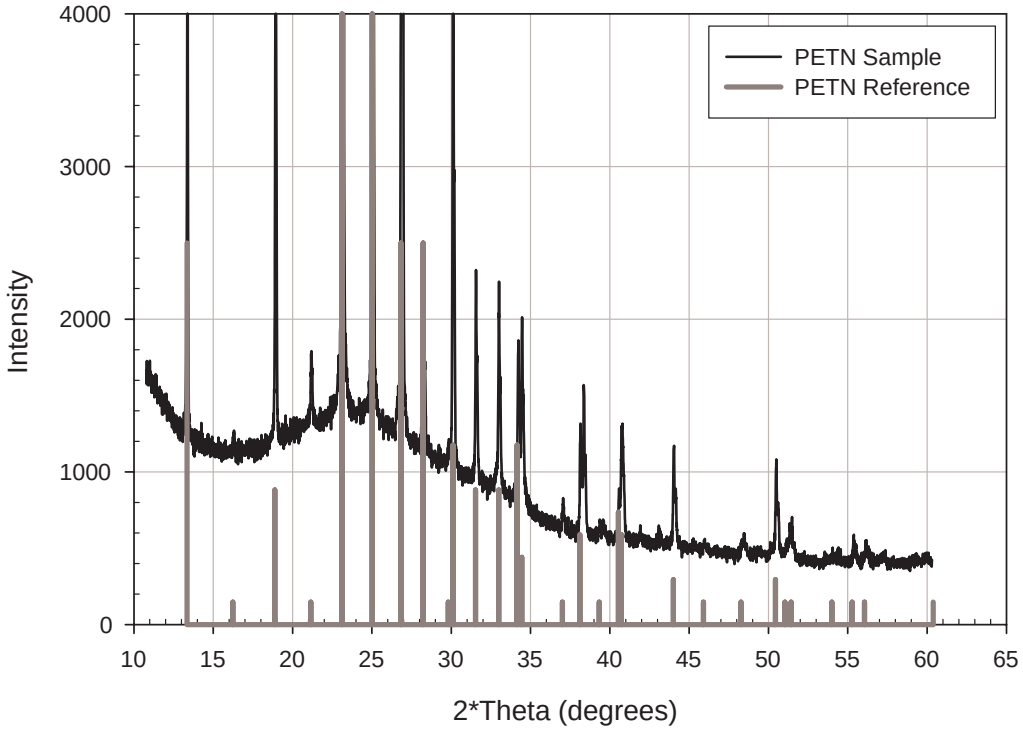

Figure A.1. X-ray diffraction data for PETN showing intensity peaks versus scattering twice the diffraction angle

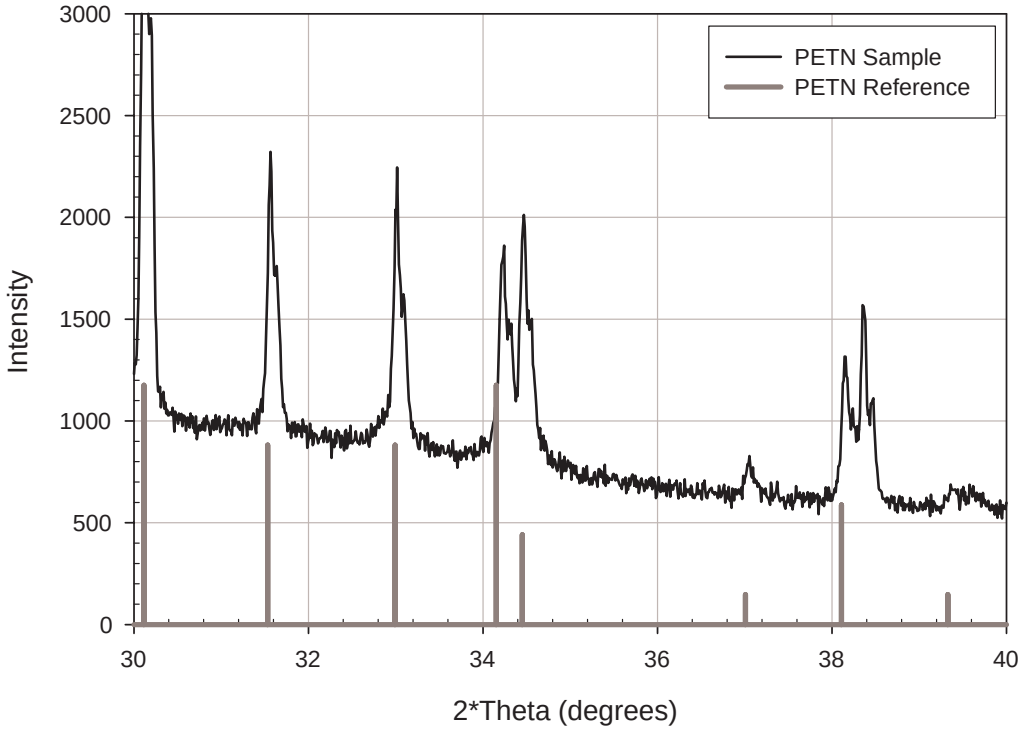

Figure A.2. X-ray diffraction data for PETN showing intensity peaks versus scattering twice the scattering angle, detail

Appendix B

MATLAB Shock Detection Program

B.1 Main Program

```
% mjh_shock_detect2.m
%
% This program tracks a shock wave
%
% Designed to work with APX images with shock moving right to ↘
    left
% across the image
% The program starts at the end of the explosion and tracks ↘
    the shock back
% to the beginning.
% The shock is determined by the line from the shadowgraph ↘
    which is found
% by locating the maximum intensity.
%
% Michael J. Hargather
% Penn State Gas Dynamics Lab
% Written December 1, 2005
%
% Edit History
% This file replaces all mjh_shock_detect_modX.m files
% The last working mod was mod9
% January 30, 2006 - added a second curve fit and changed ↘
    outputting to
%   accomodate
% April 24, 2006 - added more arrays for output
% May 4, 2005 - added one line to make velocity array same ↘
    size as shock
%   radius array, useful for data analysis
% July 27, 2006 - added calculation of curve fits before ↘
    charge scaling and
%   modified the output file accordingly
% August 30, 2006 - added a variable "output_file_name" to the↘
     load file,
```

```
%   used for naming the output file, movie, and the x-t ↘
    diagram

close all;
clear all;
format compact;

% file that all variables are in, which is designated in the ↘
    file call
petn_20060124_9_detect2;

% find the explosion center
pic_exp = [pic_name_prefix num2str(num_pic_exp,'%06d') '.tif'↘
    ];
pic_mark = [pic_name_prefix num2str(num_pic_mark,'%06d') '.tif↘
    '];
orig = imread([file_path pic_exp]);
mark = imread([file_path pic_mark]);

% sequence to crop images
if crop_image == 1
    orig = imcrop(orig, crop_rect);
    mark = imcrop(mark, crop_rect);
end

% flip pictures left and right
if shock_flip_lr == 1
    orig = fliplr(orig);
    mark = fliplr(mark);
end

figure, imshow(orig)

pic_height = size(orig,1);
pic_length = size(orig,2);

max_a=1;
for i=1:pic_height
    for j=1:pic_length
        a=orig(i,j);
        if a>max_a
            max_a=a;
            r_center=i;
            c_center=j;
        end
```

```
    end
end

max_a
r_center
c_center

orig_marked = orig;
orig_marked(:,c_center) = 250;
orig_marked(r_center,:) = 250;
mark_marked = mark;
mark_marked(:,c_center) = 250;
mark_marked(r_center,:) = 250;
figure, imshow(orig_marked);
figure, imshow(mark_marked);

user_cont = input('Do you want to continue with the given ↘
   center? 1=Y 2=N --> ');

% sequence to manually change center if desired
if user_cont == 2
    while user_cont == 2
        r_center = input('Enter a new row number: ');
        c_center = input('Enter a new column number: ');

        orig_marked = orig;
        orig_marked(:,c_center) = 250;
        orig_marked(r_center,:) = 250;
        mark_marked = mark;
        mark_marked(:,c_center) = 250;
        mark_marked(r_center,:) = 250;
        figure, imshow(orig_marked);
        figure, imshow(mark_marked);

        user_cont = input('Do you want to continue with the ↘
           given center? 1=Y 2=N --> ');
    end
end

if shadow_geom==1
    explos_pixel = c_center;                    % pixel number↘
        for explosion center
    half_image = round(pic_length/2);           % half the ↘
       number of pixels in the image
    x_c = explos_pixel-half_image;
```

```
    theta_c = atan(x_c/screen_dist);
    d_cos_theta_c = explos_dist/cos(theta_c);
end

% set y_max so do not try to go outside of picture to find ↘
   shock
if r_center > pic_height/2
    y_max = pic_height - r_center;
end
if r_center <= pic_height/2
    y_max = r_center - 1;
end

% make the matrix to hold the x vs t composite
make_xt = 1;
if make_xt==1
%     xt_pic = zeros(num_pictures, pic_length);
%     xt_pic_shock = zeros(num_pictures, pic_length);

    % for making a thicker x-t diagram, uses 3 center frames
    xt_pic = zeros(num_pictures*5, pic_length);
    xt_pic_shock = zeros(num_pictures*5, pic_length);
end

back_track_change = 0;

% if the user chooses to continue the proceed, if not then end
if user_cont==1
    inten_sum = zeros(num_pictures, pic_length);
    for j=1:1:num_pictures
        % define the picture name
        current_pic_num=last_pic+1-j;
        pic_name = [pic_name_prefix num2str(current_pic_num, '↘
           %06d') '.tif'];

        % read in the picture for a given file path and ↘
           picture name
        pic=imread([file_path pic_name]);

        % sequece to crop images
        if crop_image == 1
            pic = imcrop(pic, crop_rect);
        end

        % flip pictures left and right
```

```
if shock_flip_lr == 1
    pic = fliplr(pic);
end

% adjust intensity, rescales [] to 0-->1
pic_adj = pic;
if pic_intensity_rescale == 1
    pic_adj = imadjust(pic,pic_intensity_new);
end

% add title frame
if j==1
    pic_title = pic;
    pic_title(:,:)=min(min(pic_adj));
    stamp_color = max(max(pic_adj));
    stamp_left = 10;
    stamp_top = 5;

    for m=1:1:num_title_lines;
        stamp_writing = title_slide(m,:);
        pic_title = mjh_text_seq_mod1(pic_title,↘
            stamp_writing,stamp_color,stamp_top,↘
            stamp_left);
        stamp_top = stamp_top + 15;
    end %for

    figure, imshow(pic_title);

    %pic_frame = 1+63*(double(pic)/255);
    mov(1)=im2frame(pic_title, gray);
end %if

% loop to find shock
inten_min = 250;
radius_max = c_center - shock_loc_previous;

% fudge factor for allowing shock to move backwards
% only use if need to, should not be needed in a clean↘
    shot
if back_track > 0
    if shock_loc_previous <= 10
        if back_track ~= 0
            back_track_orig = back_track;
            back_track = 0;
            back_track_change = 1;
```

```
        end
    end
elseif shock_loc_previous > 10
    if back_track_change == 1
        back_track = back_track_orig;
        back_track_change = 0;
    end
end

% sequence for changing to edge detection for center ↘
   of explosion
if current_pic_num <= edge_pic_num
    edge_detect_seq;
    range = range+3;
end

% check to make sure range is within the picture
if radius_max-range<=2
    range = radius_max-1;
end

for radius = (radius_max-range):1:(radius_max+↘
   back_track)
    r_squared = radius*radius;
    x_current = radius;
    y_half_x = 0;
    %inten_sum(radius) = 0;
    inten_count = 0;

    % loop through routine until y reaches end of ↘
       picture
    while y_half_x < y_max
        y_init = y_half_x;
        x_half = x_current - 0.5;
        y_half_x = round(sqrt(r_squared-x_half^2));

        % limit search to within picture
        if y_half_x > y_max
            y_half_x = y_max;
        end

        for ci=y_init:1:y_half_x
            y_plus = double(pic_adj(r_center+ci,↘
               c_center-x_current));
```

```
            y_minus = double(pic_adj(r_center-ci,↘
                c_center-x_current));
            inten_sum(j,radius) = inten_sum(j,radius) ↘
               + y_plus + y_minus;

            inten_count = inten_count + 2;
        end

        x_current = x_current - 1;
        if x_current <= 0
            y_half_x = y_max;
        end
    end %while y_half_x < y_max

    % change total intensity to average
    inten_sum(j,radius) = inten_sum(j,radius)/↘
       inten_count;


    % update shock location if new position is lower ↘
       intensity
    if current_pic_num > edge_pic_num
        if inten_sum(j,radius) < inten_min
            shock_loc = c_center - radius;
            inten_min = inten_sum(j,radius);
            inten_iter(j) = inten_sum(j,radius);
        end
    end

    % for edge detection seq
    if current_pic_num <= edge_pic_num
        if inten_sum(j,radius) >= 0.50
            shock_loc = c_center-radius;
            inten_iter(j) = inten_sum(j,radius);
        end
    end
end % for radius=(radius_max-range):1:(radius_max+↘
   back_track)

% added section for last shock point
if j== num_pictures
    shock_loc = c_center;
end %if

% function for making x vs t picture composite
```

```
        if make_xt==1
%           xt_pic(num_pictures-j+1,:) = pic(r_center,:);

            % sequence for a thicker x-t diagram
            xt_pic((num_pictures-j+1)*5,:)=pic(r_center+2,:);
            xt_pic((num_pictures-j+1)*5-1,:)=pic(r_center+1,:)↘
                ;
            xt_pic((num_pictures-j+1)*5-2,:)=pic(r_center,:);
            xt_pic((num_pictures-j+1)*5-3,:)=pic(r_center-1,:)↘
                ;
            xt_pic((num_pictures-j+1)*5-4,:)=pic(r_center-2,:)↘
                ;
        end

        % sequence for manual shock positioning
        if manual_shock_loc == 1
            if current_pic_num <= manual_shock_pic
                manual_shock_cont = 2;
                while manual_shock_cont ~= 1
                    pic_shock_drawn = pic;

                    % draw the shock as it was calculated - ↘
                        actual arc
                    draw_count = 0;
                    draw_radius = c_center - shock_loc;
                    draw_x_current = draw_radius;
                    draw_y_half_x = 0;
                    while draw_y_half_x < y_max
                        draw_y_init = draw_y_half_x;
                        draw_x_half = draw_x_current - 0.5;
                        draw_y_half_x = round(sqrt(draw_radius↘
                            ^2 - draw_x_half^2));

                        % limit search to within picture
                        if draw_y_half_x > y_max
                            draw_y_half_x = y_max;
                        end

                        for di=draw_y_init:1:draw_y_half_x
                            if (r_center+di) < pic_height
                                if (r_center-di) > 1
                                    if (c_center-↘
                                        draw_x_current) >1
```

```
                                    if (c_center-↘
                                       draw_x_current) < ↘
                                       pic_length
                                        pic_shock_drawn(↘
                                           r_center+di,↘
                                           c_center-↘
                                           draw_x_current)↘
                                            = 250;
                                        pic_shock_drawn(↘
                                           r_center-di,↘
                                           c_center-↘
                                           draw_x_current)↘
                                            = 250;
                                    end
                                end
                            end
                        end
                    end

                    draw_x_current = draw_x_current - 1;
                    if x_current <= 0
                        draw_y_half_x = y_max;
                    end

                    draw_count = draw_count + 1;
                    if draw_count == 100
                        draw_y_half_x = y_max;
                    end
                end %draw loop

                % user input for a new radius
                draw_radius
                figure, imshow(pic_shock_drawn);
                manual_shock_cont = input('Do you want to ↘
                   continue with the given radius? 1=Y 2=N↘
                   ::');
                if manual_shock_cont ~= 1
                    draw_radius = input('Enter a new ↘
                       radius:: ');
                    shock_loc = c_center - draw_radius;
                end

            end %while
        end %if current_pic_num <=manual_shock_pic
    end %manual_shock_loc
```

```
% draw the shock as it was calculated - actual arc
draw_count = 0;
draw_radius = c_center - shock_loc;
draw_x_current = draw_radius;
draw_y_half_x = 0;
while draw_y_half_x < y_max
    draw_y_init = draw_y_half_x;
    draw_x_half = draw_x_current - 0.5;
    draw_y_half_x = round(sqrt(draw_radius^2 - ↘
       draw_x_half^2));

    % limit search to within picture
    if draw_y_half_x > y_max
        draw_y_half_x = y_max;
    end

    for di=draw_y_init:1:draw_y_half_x
        if (r_center+di) < pic_height
            if (r_center-di) > 1
                if (c_center-draw_x_current) >1
                    if (c_center-draw_x_current) < ↘
                       pic_length
                        pic(r_center+di,c_center-↘
                           draw_x_current) = 250;
                        pic(r_center-di,c_center-↘
                           draw_x_current) = 250;
                    end
                end
            end
        end
    end

    draw_x_current = draw_x_current - 1;
    if x_current <= 0
        draw_y_half_x = y_max;
    end

    draw_count = draw_count + 1;
    if draw_count == 100
        draw_y_half_x = y_max;
    end
end

% save position of shock into vector
```

```
        shock(j) = shock_loc;
        shock_loc_previous = shock_loc;

        % corrected shock location if enabled
        if shadow_geom==1
            x_s = half_image-shock_loc;
            theta_s = atan(x_s/screen_dist);
            theta = theta_c + theta_s;
            shock_radius(j) = sin(theta)*d_cos_theta_c;      % ↘
               note radius still in pixels
        end

        % length scaling
        if scale_factors==1
            shock_radius_scale(j) = shock_radius(j) * ↘
               length_scale;
        end

        % mark the line of the shock on the picture for ↘
           validation
        % turn into a movie so can watch to validate
        %pic(:,shock_loc)=0;
        %new_pic=1+63*(double(pic)/255);
        mov(j+1)=im2frame(pic,gray);

        % write each individual picture with the shock ↘
           highlighted
%         imwrite(pic, ['pictures/' 'adj_' pic_name]);

        % function for making x vs t picture composite with ↘
           shock labeled
        if make_xt==1
%             xt_pic_shock(num_pictures-j+1,:) = pic(r_center↘
    ,:);

            % for thicker x-t diagram
            xt_pic_shock((num_pictures-j+1)*5,:)=pic(r_center↘
               +2,:);
            xt_pic_shock((num_pictures-j+1)*5-1,:)=pic(↘
               r_center+1,:);
            xt_pic_shock((num_pictures-j+1)*5-2,:)=pic(↘
               r_center,:);
            xt_pic_shock((num_pictures-j+1)*5-3,:)=pic(↘
               r_center-1,:);
```

```
        xt_pic_shock((num_pictures-j+1)*5-4,:)=pic(↘
            r_center-2,:);
    end

    if j==round(num_pictures/2)
        figure, imshow(pic), title('Middle Picture of Set,↘
            with Shock Highlighted');
    end
end

% velocity calculation for when scaling is enabled
if scale_factors==1
    % 5th order scheme
    %         for r=3:1:(num_pictures-2)
    %             p=r-2;
    %             q=r-1;
    %             s=r+1;
    %             t=r+2;
    %             % 4th order derivative calculation from ↘
        Cheney & Kincaid 2004 with
    %             % sign correction on 2/3 term, found ↘
        error in book
    %             velocity(r) = -(2/3*(shock_radius_scale(↘
        s) - shock_radius_scale(q)) - (shock_radius_scale(t↘
        ) - shock_radius_scale(p))/12)/time_scale;
    %         end

    % 3rd order scheme
    for r=2:1:(num_pictures-1)
        q=r-1;
        s=r+1;
        velocity(r) = -((shock_radius_scale(s)-↘
            shock_radius_scale(q))/2)/time_scale;
    end
    velocity(num_pictures)=0;        % added 5/4/2006
    mach_num=velocity/speed_sound;
end

% display plot of position vs frame #, make a movie
%   figure, plot(shock), xlabel('time'), ylabel('pixel'), ↘
    title('Shock Location');

if shadow_geom==1
    %         figure, plot(shock_radius),xlabel('time'), ↘
        ylabel('pixel'), title('Corrected Shock Location');
```

```
end

% close all figures before putting up final ones
close all;

% show xt composite
if make_xt==1
    xt_pic = mat2gray(xt_pic);
    xt_pic_shock = mat2gray(xt_pic_shock);
    %         figure, imshow(xt_pic), title('X-T Diagram ↘
        of Explosion');
    figure, imshow(xt_pic_shock), title('X-T Diagram of ↘
        Explosion with Shock Highlighted');
    imwrite(xt_pic_shock, strcat('pictures/', ↘
        output_file_name, '.tif'));
end

if scale_factors==1
    figure, plot(shock_radius_scale),xlabel('time [frames]↘
        '), ylabel('length [meters]'), title('Corrected and↘
        Scaled Shock Location - "shock\_radius\_scale"');
    %         figure, plot(velocity),xlabel('time [frames↘
        ]'), ylabel('velocity [m/s]'), title('Velocity');
    figure, plot(mach_num),xlabel('time [frames]'), ylabel↘
        ('Mach Number'), title('Mach Number - "mach\_num"')↘
        ;
end

movie2avi(mov,['movies/' output_file_name '.avi'],'↘
    compression','none','fps',1);

% reset the shock distance to start at 0 for curve fit and↘
    data output
shock_radius_absolute = flipud(shock_radius_scale');
shock_radius_absolute = shock_radius_absolute-↘
    shock_radius_absolute(1);

% sequence to fit a curve to the data
curve_time_all = (linspace(0,size(shock_radius_absolute,1)↘
    -1,size(shock_radius_absolute,1))')*time_scale;
curve_radius_all = shock_radius_absolute;

% routine to remove data points that are unwanted before ↘
    fit curve
adp=0;
```

```
for rdp=1:1:size(shock_radius_absolute,1)
    if curve_radius_all(rdp)>0
        adp = adp + 1;
        curve_radius(adp) = curve_radius_all(rdp);
        curve_time(adp) = curve_time_all(rdp);
    end
end

curve_radius = curve_radius';
curve_time = curve_time';

% curve fit for data before mass scaling
least_sq_curve_fit_shock_mod1;
least_sq_curve_fit_shock_mod2;
curve_coef_unscaled_mod1=curve_coef_mod1;
curve_r_squared_unscaled_mod1=curve_r_squared_mod1;
curve_coef_unscaled_mod2=curve_coef_mod2;
curve_r_squared_unscaled_mod2=curve_r_squared_mod2;

% charge scaling for various masses
if charge_mass_scale==1
    curve_time = curve_time*charge_mass_scale_c/↘
       charge_mass_scale_s;
    curve_radius = curve_radius/charge_mass_scale_s;
end

% curve fits
least_sq_curve_fit_shock_mod1;
least_sq_curve_fit_shock_mod2;

% output
output_mn = flipud(mach_num');

    % uncertainty calculation
uncert_c_sq = (delta_calib/(pixel_length*(↘
   calib_object_length)))^2;
uncert_time_sq = (delta_time/time_scale)^2;
uncert_temp_sq = (delta_temp/(273+(5/9*(room_temp_F-32))))↘
   ^2;
for un=1:1:size(shock_radius_absolute,1)-1
    uncert(un,1) = shock_radius_absolute(un)*sqrt((delta_r↘
       /shock_radius(num_pictures-un+1))^2+uncert_c_sq);
    uncert(un,2) = output_mn(un)*sqrt(2*(uncert(un,1)/↘
       shock_radius_absolute(un))^2+2*uncert_time_sq+0.25*↘
       uncert_temp_sq);
```

```
    end
    un=un+1;
    uncert(un,1) = shock_radius_absolute(un)*sqrt((delta_r/↘
        shock_radius(un))^2+uncert_c_sq);

    % output values
    % also include output_mn, found above the uncertainty calc
    output_coef = [room_temp_F; curve_coef_mod1; a_0; ↘
        curve_r_squared_mod1; frame_rate; speed_sound; ↘
        curve_coef_mod2; curve_r_squared_mod2;...
            r_center; c_center; charge_mass; ↘
                charge_mass_standard; curve_coef_unscaled_mod1↘
                ;...
            curve_r_squared_unscaled_mod1; ↘
                curve_coef_unscaled_mod2; ↘
                curve_r_squared_unscaled_mod2];
    output_coef_label=char('room_temp_F','A_mod1','B_mod1','↘
        C_mod1','D_mod1','a_0',...
            'curve_r_squared_mod1','frame_rate','speed_sound',↘
                'A_mod2','B_mod2',...
            'C_mod2','D_mod2','curve_r_squared_mod2','r_center↘
                ','c_center',...
            'charge_mass','charge_mass_standard',...
            'A_unscaled_mod1','B_unscaled_mod1','↘
                C_unscaled_mod1','D_unscaled_mod1',...
            'curve_r_squared_unscaled_mod1','A_unscaled_mod2',↘
                'B_unscaled_mod2',...
            'C_unscaled_mod2','D_unscaled_mod2','↘
                curve_r_squared_unscaled_mod2');
    output_shock_rad_abs = shock_radius_absolute;
    output_shock_pixel=flipud(shock');
    output_uncert = uncert;

    % create output file
    detect2_output;
end
```

B.2 Typical Variable Load File

```
% petn_20060124_9_detect2.m
%
% This code is loaded into mjh_shock_detect for a specific set↘
    of pictures
```

```
% This includes all run specific variables
% Created so can review what was done for each run
%
% Michael J. Hargather
% Penn State Gas Dynamics Lab
% Written December 1, 2005
%
% edit history
% This file replaces all mjh_shock_detect_modX.m files
% The last working mod was mod9

% variables and settings
file_path = ['/mike/GDL/apx/petn_20060124/↘
    petn_20060124_9_C001S0001/'];
pic_name_prefix = 'petn_20060124_9_c001s0001';
output_file_name = 'petn_20060124_9';
% title slide information
title_slide = char('petn_20060124_9');
num_title_lines = size(title_slide,1);

num_pic_exp = 3;
num_pic_mark = 10;
last_pic = 49;                          % last picture frame ↘
    shock is in, will be first cycled through
num_pictures = last_pic-num_pic_exp+1; % number of pictures ↘
    to look through
shock_loc_previous = 1;                 % side of picture ↘
    where shock exits from
range = 10;                             % limited jump shock ↘
    can make between picture frames
calib_object_length = 19.25             % length of ↘
    calibration object in inches
pixel_length = 18.70;                    % number of pixels ↘
    per inch
frame_rate = 36000;
room_temp_F = 61;
edge_pic_num = 49;                      % picture number for ↘
    transition to edge detection
charge_mass = 0.001003;                 % charge mass in kg
charge_mass_standard = 0.001;           % mass of charge to ↘
    scale everything to in kg
pressure_ambient = 101325;              % ambient pressure in ↘
    Pa
back_track = -1;                        % -1 makes the shock ↘
    always move towards charge center
```

```
                                        % 0 allows shock to ↘
                                            not move between ↘
                                            frames
                                        % +x would allow the ↘
                                            shock to move
                                        % backwards x pixels
manual_shock_loc = 0;                   % activates manual ↘
    shock sequence
manual_shock_pic = 43;                  % picture number to ↘
    switch to manual shock positioning
pic_intensity_rescale = 0;              % enables picture ↘
    intensity rescaling
pic_intensity_new = [0 0.7];            % range to stretch in ↘
    intensity adjustment [] -> [0 1]
delta_r = 2;                            % uncertainty in ↘
    radius measurement in pixels
delta_calib = 2;                        % uncertainty in ↘
    calibration image in pixels
delta_time = 0;                         % uncertainty in time ↘
    measurement
delta_temp = 3;                         % uncertainty in ↘
    temperature in Celsius


% option to crop images
% crop_rect = [xmin ymin width height] - top left corner then ↘
    distances to include
crop_image = 0;
crop_rect = [1,200,512,50];

% option to flip pictures left/right
% explosion center must be on right side of image
shock_flip_lr = 1;

% variables for shadow geometry distortion issue
shadow_geom=1;                      % set to 1 to initialize ↘
    geometry correction
                                    % to disable, set explos_dist ↘
                                        = screen_dist
if shadow_geom==1
    screen_dist = (22*12+3)*pixel_length;    % perpendicular ↘
        distance from screen to camera, in pixels
    explos_dist = (22*12+3)*pixel_length;    % perpendicular ↘
        distance from explosion center to camera, in pixels
end
```

```
% variables for length scaling
% geometry correction must also be activated to do length ↘
    scaling
scale_factors=1;                                    % set to 1 to ↘
    initialize scale correction
if scale_factors==1;
     length_scale = 0.0254/pixel_length;% x meters/pixel
     time_scale = 1/frame_rate;                     % t seconds/↘
        frame
     sq_gamma_R = sqrt(1.4*287);
     speed_sound = sq_gamma_R*sqrt(273+(5/9*(room_temp_F-32)));↘
         % speed of sound for Mach number plotting
end

% variables for mass scaling of charges
% must have other scalings activated
charge_mass_scale = 1;
if charge_mass_scale == 1
     charge_mass_scale_s = (charge_mass/charge_mass_standard)↘
        ^(1/3)*(101325/pressure_ambient)^(1/3);
     charge_mass_scale_c = speed_sound/340.29;
end

shock_loc=1;
```

B.3 Least-Squares Curve-Fit Module

```
% least_sq_curve_fit_shock_mod2.m
%
% this program performs a least squares fit to a data set for ↘
    a given
% equation that the data follows
% the equation for this is the equation for the radius of a ↘
    shock as a
% function of time as stated by H. Kleine in "Studies of the ↘
    TNT
% equivalence of silver azide charges" - Shock Waves (2003) ↘
    13: 123-138
% mjhargather reference id = 2526
% R = A + B*a_0*t + C*ln(1+a_0*t) + D*sqrt(ln(1+a_0*t))
% where a_0 is the speed of sound at NTP = 340.29 m/s
%
```

```
% Written by
% Michael J. Hargather
% Penn State Gas Dynamics Lab
% April 27, 2005
%
% Edit history
% April 28, 2005 - added R^2 calculation, method from Chapra and Canale
%       "Numerical Methods for Engineers" 4th ed
% January 30, 2006 - MOD2 - forces B coefficient to 1

% initialize matricies
curve_A = zeros(3);
curve_B = zeros(3,1);
curve_coef = zeros(3,1);

curve_t_points = curve_time;
curve_r_points = curve_radius;
curve_num_points=size(curve_t_points,1);

% speed of sound at NTP --> 288.16K 101.325 kPa
a_0 = 340.29;

for curve_i=1:1:curve_num_points
    a_0_t = a_0 * curve_t_points(curve_i);
    ln_a_0_t = log(1+a_0_t);
    sq_ln_a_0_t = sqrt(ln_a_0_t);

    curve_A(1,1) = curve_A(1,1) + 1;
    curve_A(1,2) = curve_A(1,2) + ln_a_0_t;
    curve_A(1,3) = curve_A(1,3) + sq_ln_a_0_t;
    curve_A(2,1) = curve_A(2,1) + ln_a_0_t;
    curve_A(2,2) = curve_A(2,2) + ln_a_0_t*ln_a_0_t;
    curve_A(2,3) = curve_A(2,3) + ln_a_0_t*sq_ln_a_0_t;
    curve_A(3,1) = curve_A(3,1) + sq_ln_a_0_t;
    curve_A(3,2) = curve_A(3,2) + ln_a_0_t*sq_ln_a_0_t;
    curve_A(3,3) = curve_A(3,3) + ln_a_0_t;

    curve_B(1) = curve_B(1) + curve_r_points(curve_i) - a_0_t;
    curve_B(2) = curve_B(2) + (curve_r_points(curve_i) - a_0_t)*ln_a_0_t;
    curve_B(3) = curve_B(3) + (curve_r_points(curve_i) - a_0_t)*sq_ln_a_0_t;

end %for
```

```
curve_coef = curve_A^-1*curve_B;

% calculation of r^2 for curve fit
curve_sum_resid=0;
curve_mean_y=0;
curve_mean_y_count=0;
% calculate S_r
for curve_i=1:1:curve_num_points
    % sum of the square of the residuals
    curve_sum_resid = curve_sum_resid + (curve_r_points(↘
       curve_i) - (curve_coef(1) + a_0*curve_t_points(curve_i)↘
        + curve_coef(2)*log(1+a_0*curve_t_points(curve_i)) + ↘
       curve_coef(3)*sqrt(log(1+a_0*curve_t_points(curve_i))))↘
       )^2;
    curve_mean_y = curve_mean_y + curve_r_points(curve_i);
    curve_mean_y_count = curve_mean_y_count + 1;
end %for

curve_mean_y= curve_mean_y / curve_mean_y_count;
curve_sum_around_mean=0;

% calculate S_t
for curve_i=1:1:curve_num_points
    curve_sum_around_mean = curve_sum_around_mean + ...
        (curve_r_points(curve_i) - curve_mean_y)^2;
end %for

% optional printing
% curve_sum_around_mean
% curve_sum_resid

% print r^2
curve_r_squared = (curve_sum_around_mean-curve_sum_resid)/↘
   curve_sum_around_mean
curve_r_squared_mod2 = curve_r_squared;
curve_coef_mod2 = [curve_coef(1);1;curve_coef(2);curve_coef(3)↘
   ];
```

B.4 Edge Detection Module

```
% edge_detect_seq
%
```

```
% This file can be called to detect the outer edge of a shock.
% The image to be manipulated should be called "pic_adj"
% Written to work with MJH_SHOCK_DETECT_MOD6
%
% Michael J. Hargather
% Penn State Gas Dynamics Lab
% Written May 25, 2005
%
% July 25, 2005 - added sequence to move picture to the right ↘
    by 1 pixel

% lines used in the image manipulation
se = strel('line',3,90);                % vertical line
sed = strel('diamond',1);               % diamond array

% edge detect
pic_edge = edge(pic_adj,'prewitt',[],'vertical');

% dilations and erosions and bridging pixel gaps
pic_mod = bwmorph(pic_edge,'bridge');
pic_mod = imdilate(pic_mod,se);
pic_mod = imdilate(pic_mod,sed);
pic_mod = imdilate(pic_mod,sed);
pic_mod = bwmorph(pic_mod, 'bridge');
pic_mod = imerode(pic_mod, sed);
pic_mod = imerode(pic_mod, sed);
pic_adj = bwmorph(pic_mod, 'bridge');

% sequence to move entire picture to the right by 1 pixel
for z=pic_length:-1:2
    pic_adj(:,z) = pic_adj(:,z-1);
end
```

REFERENCES

[1] G. F. Kinney and K. J. Graham. *Explosive shocks in air*. Springer-Verlag, 1985.

[2] W. E. Baker. *Explosions in air*. University of Texas Press, 1973.

[3] B. Hopkinson. British Ordnance Minutes, 13563, 1915.

[4] J. M. Dewey. Expanding spherical shocks (blast waves). In G. Ben-Dor, O. Igra, and E. Elperin, editors, *Handbook of Shock Waves, Vol. 2*, pages 441–481. Academic Press, 2001.

[5] R. G. Sachs. Dependence of blast on ambient pressure and temperature. Technical Report BRL-466, Army Ballistic Research Lab, Aberdeen Proving Ground, 1944.

[6] J. M. Dewey. Air velocity in blast waves from TNT explosions. *Royal Society – Proceedings Series A*, 279(1378):366–385, 1964.

[7] H. Kleine, J. M. Dewey, K. Ohashi, T. Mizukaki, and K. Takayama. Studies of the TNT equivalence of silver azide charges. *Shock Waves*, 13(2):123–138, 2003.

[8] J. M. Dewey. The properties of a blast wave obtained from an analysis of the particle trajectories. *Proceedings of the Royal Society of London Series A - Mathematical and Physical Sciences*, 324(1558):275–299, 1971.

[9] J. M. Dewey. Explosive flows: Shock tubes and blast waves. In *Handbook of Flow Visualization*, book chapter 29, pages 481–497. Hemisphere Publishing Corp., 1st edition, 1989.

[10] J. D. Anderson. *Modern compressible flow: with historical perspective*. McGraw-Hill, 2003.

[11] M. Held. Blast waves in free air. *Propellants Explosives Pyrotechnics*, 8(1):1–7, 1983.

[12] T. Krauthammer and A. Altenberg. Negative phase blast effects on glass panels. *International Journal of Impact Engineering*, 24(1):1–17, 2000.

[13] T. L. Davis. *The chemistry of powder and explosives*. Wiley, 1943.

[14] P. W. Cooper. Comments on TNT equivalence. In *20th International Pyrotechnics Seminar*, pages 215–226, 1994.

[15] G. I. Taylor. The formation of a blast wave by a very intense explosion .1. Theoretical discussion. *Proceedings of the Royal Society of London Series A-Mathematical and Physical Sciences*, 201(1065):159–174, 1950.

[16] H. L. Brode. Blast wave from a spherical charge. *Physics of Fluids*, 2(2):217–229, 1959.

[17] S. A. Formby and R. K. Wharton. Blast characteristics and TNT equivalence values for some commercial explosives detonated at ground level. *Journal of Hazardous Materials*, 50(2-3):183–198, 1996.

[18] E. D. Esparza. Blast measurements and equivalency for spherical charges at small scaled distances. *International Journal of Impact Engineering*, 4(1):23–40, 1986.

[19] R. K. Wharton, S. A. Formby, and R. Merrifield. Airblast TNT equivalence for a range of commercial blasting explosives. *Journal of Hazardous Materials*, 79(1):31–39, 2000.

[20] J. M. Dewey. The TNT equivalence of an optimum propane-oxygen mixture. *Journal of Physics D: Applied Physics*, 38(23):4245–4251, 2005.

[21] M. Held. TNT-equivalent. *Propellants Explosives Pyrotechnics*, 8(5):158–167, 1983.

[22] R. Houlston, J. E. Slater, N. Pegg, and C. G. DesRochers. On analysis of structural response of ship panels subjected to air blast loading. *Computers and Structures*, 21(1-2):273–289, 1985.

[23] A. C. Jacinto, R. D. Ambrosini, and R. F. Danesi. Experimental and computational analysis of plates under air blast loading. *International Journal of Impact Engineering*, 25(10):927–947, 2001.

[24] G. S. Settles. *Schlieren and shadowgraph techniques: Visualizing phenomena in transparent media*. Springer-Verlag, 2001.

[25] G. N. Nurick and J. B. Martin. Deformation of thin plates subjected to impulsive loading - A review .2. Experimental studies. *International Journal of Impact Engineering*, 8(2):171–186, 1989.

[26] G. N. Nurick, M. E. Gelman, and N. S. Marshall. Tearing of blast loaded plates with clamped boundary conditions. *International Journal of Impact Engineering*, 18(7-8):803–827, 1996.

[27] R. G. Teelingsmith and G. N. Nurick. The deformation and tearing of thin circular plates subjected to impulsive loads. *International Journal of Impact Engineering*, 11(1):77–91, 1991.

[28] S. R. Bodner and P. S. Symonds. Experiments on viscoplastic response of circular plates to impulsive loading. *Journal of the Mechanics and Physics of Solids*, 27(2):91–113, 1979.

[29] T. Wierzbicki and G. N. Nurick. Large deformation of thin plates under localised impulsive loading. *International Journal of Impact Engineering*, 18(7-8):899–918, 1996.

[30] G. S. Langdon, S. C. K. Yuen, and G. N. Nurick. Experimental and numerical studies on the response of quadrangular stiffened plates. Part II: Localised blast loading. *International Journal of Impact Engineering*, 31(1):85–111, 2005.

[31] N. Jacob, G. N. Nurick, and G. S. Langdon. The effect of stand-off distance on the failure of fully clamped circular mild steel plates subjected to blast loads. *Engineering Structures*, 29(10):2723–2736, 2007.

[32] M. Stoffel, R. Schmidt, and D. Weichert. Shock wave-loaded plates. *International Journal of Solids and Structures*, 38(42-43):7659–7680, 2001.

[33] M. Stoffel. Experimental validation of simulated plate deformations caused by shock waves. *Zamm-Zeitschrift fur Angewandte Mathematik und Mechanik*, 85(9):643–659, 2005.

[34] H. S. Turkmen. Structural response of laminated composite shells subjected to blast loading: Comparison of experimental and theoretical methods. *Journal of Sound and Vibration*, 249(4):663–678, 2002.

[35] H. M. Wen and N. Jones. Experimental investigation of the scaling laws for metal plates struck by large masses. *International Journal of Impact Engineering*, 13(3):485–505, 1993.

[36] H. M. Wen and N. Jones. Experimental investigation into the dynamic plastic response and perforation of a clamped circular plate struck transversely by a mass. *Proceedings of the Institution of Mechanical Engineers, Part C: Journal of Mechanical Engineering Science*, 208(2):113–137, 1994.

[37] G. J. McShane, D. D. Radford, V. S. Deshpande, and N. A. Fleck. The response of clamped sandwich plates with lattice cores subjected to shock loading. *European Journal of Mechanics, A/Solids*, 25(2):215–229, 2006.

[38] D. D. Radford, G. J. McShane, V. S. Deshpande, and N. A. Fleck. The response of clamped sandwich plates with metallic foam cores to simulated blast loading. *International Journal of Solids and Structures*, 43(7-8):2243–2259, 2006.

[39] G. N. Nurick and J. B. Martin. The measurement of the response of clamped circular plates to impulsive loading. *Institute of Physics Conference Series*, 70(70):495–502, 1984.

[40] S. G. Grantham and J. E. Field. Speckle correlation methods applied to ballistics and explosives. volume 4933 of *Proceedings of SPIE - The International Society for Optical Engineering*, pages 27–32, 2003.

[41] T. Siebert, T. Becker, K. Spiltthof, I. Neumann, and R. Krupka. High-speed digital image correlation: Error estimations and applications. *Optical Engineering*, 46(5), 2007.

[42] G. N. Nurick and J. B. Martin. Deformation of thin plates subjected to impulsive loading - A review .1. Theoretical considerations. *International Journal of Impact Engineering*, 8(2):159–170, 1989.

[43] H. S. Turkmen and Z. Mecitoglu. Nonlinear structural response of laminated composite plates subjected to blast loading. *AIAA Journal*, 37(12):1639–1647, 1999.

[44] S. C. K. Yuen and G. N. Nurick. Experimental and numerical studies on the response of quadrangular stiffened plates. Part I: Subjected to uniform blast load. *International Journal of Impact Engineering*, 31(1):55–83, 2005.

[45] J. McArthur, C. Salisbury, D. Cronin, M. Worswick, and K. Williams. High strain rate characterization of shock absorbing materials for landmine protection concepts. *Shock and Vibration*, 10(3):179–186, 2003.

[46] K. Balasubramanian and P. R. Rao. On extremity trends in advances of materials. *Ferroelectrics*, 306:235–249, 2004.

[47] C. H. Huang. Inverse evaluation of material constants for piezoceramics by out-of-plane vibration. *AIAA Journal*, 44(7):1411–1418, 2006.

[48] P. W. Cooper. *Explosives engineering*. Wiley-VCH, Inc, 1996.

[49] G. J. McKay. Forensic characteristics of organic peroxide explosives (TATP, DADP and HMTD). *Kayaku Gakkaishi/Journal of the Japan Explosives Society*, 63(6 SPEC):323–329, 2002.

[50] T. Urbanski. *Chemistry and technology of explosives*, volume 4. Pergamon Press, 1984.

[51] M. E. Staymates. Personal Communication, 2007.

[52] R. Varosh. Electric detonators: EBW and EFI. *Propellants Explosives Pyrotechnics*, 21(3):150–154, 1996.

[53] S. V. Lebedev. Explosion of a metal by an electric current. *Soviet Physics JETP-USSR*, 5(2):243–252, 1957.

[54] A. C. T. van Duin, Y. Zeiri, F. Dubnikova, R. Kosloff, and W. A. Goddard. Atomistic-scale simulations of the initial chemical events in the thermal initiation of triacetonetriperoxide. *Journal of the American Chemical Society*, 127(31):11053–11062, 2005.

[55] J. C. Oxley, J. L. Smith, and H. Chen. Decomposition of a multi-peroxidic compound: Triacetone triperoxide (TATP). *Propellants Explosives Pyrotechnics*, 27(4):209–216, 2002.

[56] F. Dubnikova, R. Kosloff, J. Almog, Y. Zeiri, R. Boese, H. Itzhaky, A. Alt, and E. Keinan. Decomposition of triacetone triperoxide is an entropic explosion. *Journal of the American Chemical Society*, 127(4):1146–1159, 2005.

[57] K. K. Kuo. *Principles of Combustion*. Wiley, 2005.

[58] I. Cho. Personal Communication, 2005.

[59] D. Hernandez. Personal Communication, 2007.

[60] H. E. Edgerton. Shockwave photography of large subjects in daylight. *Review of Scientific Instruments*, 29(2):171–172, 1958.

[61] G. S. Settles, T. P. Grumstrup, J. D. Miller, M. J. Hargather, L. J. Dodson, and J. A. Gatto. Full-scale high-speed "Edgerton" retroreflective shadowgraphy of explosions and gunshots. volume PSFVIP-5-251 of *Proceedings of PSFVIP-5, 5th Pacific Symposium on Flow Visualisation and Image Processing, 27-29th September 2005, Australia*, 2005.

[62] M. Raffel, C. E. Willert, and J. Kompenhans. *Particle Image Velocimetry*. Springer, 3rd edition, 1998.

[63] S. Rahman, E. Timofeev, and H. Kleine. Pressure measurements in laboratory-scale blast wave flow fields. *Review of Scientific Instruments*, 78(12), 2007.

[64] J. D. Anderson. *Hypersonic and high temperature gas dynamics*. McGraw-Hill, 1989.

[65] V. H. Balden and G. N. Nurick. Numerical simulation of the post-failure motion of steel plates subjected to blast loading. *International Journal of Impact Engineering*, 32(1-4):14–34, 2005.

[66] B. Luccioni, D. Ambrosini, and R. Danesi. Blast load assessment using hydrocodes. *Engineering Structures*, 28(12):1736–1744, 2006.

[67] Century Dynamics Inc. *AUTODYN User Manual*, 4.3 edition, 2005.

[68] P. A. Urtiew and B. Hayes. Parametric study of the dynamic JWL-EOS for detonation products. *Combustion Explosion and Shock Waves*, 27(4):505–514, 1991.

[69] D. Wilson. Personal Communication, 2007.

[70] Correlated Solutions Inc. *Vic-3D User Manual*, 2006.

[71] J. Strong. *Concepts of Classical Optics*. Dover, 2004.

[72] R. B. Kemp, M. E. Brown, and P. K. Gallagher. *Handbook of thermal analysis and calorimetry, volume 2: Applications to inorganic and miscellaneous materials*. Elsevier, 2003.

VITA

Michael J. Hargather

Michael John Hargather was born on December 21^{st}, 1982, in Fairport, New York, to John and Kate Hargather. Michael graduated from Fairport High School in 2001 as the salutatorian. His academic career continued at Penn State Erie, the Behrend College, where he graduated in 2004 with honors in mechanical engineering and a minor in physics. While at Behrend, Michael was an active member in social, professional, and academic activities. He founded the Behrend Sailing Club, served as the President of the American Society of Mechanical Engineers Behrend chapter, and was a Programming Assistant for the Schreyer Honors College. Michael's teaching career began as a physics lab instructor and tutor in 2002, and continued until his graduation from Behrend. For his honors thesis research, Michael wrote a molecular dynamics simulation program to investigate the motion of magnetic nano-particles suspended in a fluid. His senior design research project was the experimental development of a natural gas flow sensor.

Michael entered graduate school at The Pennsylvania State University in the summer of 2004. He joined the Penn State Gas Dynamics Lab and performed his thesis research with Dr. Gary S. Settles as his adviser. While in the Gas Dynamics Lab, Michael learned a wide variety of experimental techniques, including schlieren, shadowgraph, and particle image velocimetry. His work has been presented at the American Physical Society Division of Fluid Dynamics Conferences, the Aviation Security Technology Symposium, the International Symposium on Shock Waves, and the International Symposium on Flow Visualization. He has published in the International Journal of Shock Waves and is a reviewer for the International Journal of Impact Engineering. Michael was also the Chair of the Penn State College of Engineering Research Symposium 2008. Michael was awarded a Graduate Teaching Fellowship and taught an undergraduate level introductory fluid-thermal science course for two semesters.

Michael plans to continue experimental research on a wide variety of topics while serving as a post-doctoral research associate in the Penn State Gas Dynamics Lab. Ultimately, he hopes to become a faculty member and to operate a successful research laboratory while educating students.